



DEGREE PROJECT, IN ELECTRIC POWER ENGINEERING , SECOND LEVEL
STOCKHOLM, SWEDEN 2015

Design and Analysis of a Fractional-Slot Concentrated-Wound PM-Assisted Reluctance Motor

LUIGI MARINO

KTH ROYAL INSTITUTE OF TECHNOLOGY
ELECTRICAL ENGINEERING

”L’importante non è stabilire se uno ha paura o meno, è saper convivere con la propria paura e non farsi condizionare dalla stessa. Ecco, il coraggio è questo, altrimenti non è più coraggio, è incoscienza.””

”It is not relevant to establish whether one has fear or not, but being able to live with it without any influence. This is courage, otherwise it is unconsciousness.””

Giovanni Falcone

Abstract

The aim of this master thesis is to design and analyse a FSCW PMaSynRM (Permanent Magnet assisted Synchronous Reluctance Motor) for industrial applications. The design process includes analytical calculations (initial design and PM amount minimization) and finite element method (FEM) based design optimization. An overcompensated design is proved to be advantageous for a 10-pole reluctance motor. A comparative analysis with other rotor topologies was made, where motor performance, temperature effects and production costs are taken into account. Detailed curves which describe efficiency, power factor and current with respect to ambient temperature are studied for the proposed motor designs at different working points. The demagnetization risk is also taken into account and the safe working temperature ranges have been defined for all the considered motors.

The results show that the initial motor design with 10 poles/12 slots PMaSynRM with NdFeB magnets has poor performance in terms of efficiency and power factor, with huge amount of PM inserted. This is mainly due to the lack of reluctance torque for this relatively higher number of poles solution. Moreover, it has been found in literature and confirmed in this investigation that this negative effect for the 10-pole motor is amplified due to the presence of the concentrated winding. Indeed, it is shown by simulations that the motor performance is improved by employing 8 poles/12 slots PMaSynRM configuration with a relatively lower NdFeB magnet amount, thanks to the improved rotor anisotropy. The 10 poles/12 slots interior permanent magnet (IPM) and surface mounted permanent magnet (SMPM) topologies present higher performance due to the effective utilization of PM, mainly or completely producing the torque. Hence, IPM and SMPM do not suffer the lack of anisotropy.

Keywords: concentrated windings, demagnetization, distributed windings, ferrite, finite element method, loss distribution, natural and over compensation, overlaod, permanent magnet assisted synchronous reluctance motors, permanent magnets, rare earth magnets (NdFeB), reluctance torque, temperature effects, torque ripple.

Sammanfattning

Syftet med detta examensarbete är att utforma och analysera en FSCW PMaSynRM (Permanent Magnet assisted Synchronous Reluctance Motor) för industriella applikationer. Designprocessen omfattar analytiska beräkningar (ursprungliga konstruktion och PM belopp minimering) och finita elementmetoden (FEM) baserad design optimering. En överkompenserad design visat sig vara fördelaktigt för en 10-polig reluktansmotor. En jämförande analys med andra rotor topologier gjordes, där motor prestanda, temperatureffekter och produktionskostnader beaktas. Detaljerade kurvor som beskriver effektivitet, effektfaktor och ström med avseende på omgivningstemperatur studeras för de föreslagna motorn för vid olika arbetspunkter. Den avmagnetisering risken också beaktas och säkerhetstemperaturområden har definierats för alla ansåg motorerna.

Resultaten visar att den initiala motordesign med 10-polig/12 spår PMaSynRM med NdFeB magneter har dåliga effektivitet och effektfaktor, med enorma mängder PM insatt. Detta är främst på grund av bristen på reluktansvridmomentet för denna relativt högre poltal lösning. Dessutom har man funnit i litteraturen och bekräftat i denna undersökning att denna negativa effekt för 10-polig motorn förstärks på grund av närvaron av den koncentrerade lindningen. Faktum är att det framgår av simuleringar att motorprestanda förbättras med en 8-polig/12 spår PMaSynRM konfiguration med en relativt lägre NdFeB magnet belopp, tack vare den förbättrade rotor anisotropi. Den 10-polig/12 spår interiör permanentmagnet (IPM) och ytmonterade permanent magnet (SMPM) topologier presentera högre prestanda tack vare ett effektivt utnyttjande av PM och deras produktion vridmoment, huvudsakligen eller helt anförtrotts PM effekten.

Nyckelord: avmagnetisering, ferrit, finita elementmetoden, fördelade lindningar, förlust distribution, koncentrerade lindningar, momentrippel, naturligt och överkompensation, permanentmagnet assisterad synkron reluktansmotorer, permanentmagneter, reluktansvridmomentet, sällsynta jordmagneter (NdFeB), temperatureffekter, överbelastning.

Acknowledgements

This master thesis has been carried out at ABB LV Motors, Västerås (Sweden) within a Double Degree Programme between Politecnico di Torino (Italy) and KTH Stockholm (Sweden).

I would like to express my best appreciation to my industrial and academic supervisors Dr. Freddy Gyllenstein (ABB LV Motors), Lic.tech. Rathna Chitroju (ABB LV Motors), Lic.tech. Kashif Khan (ABB LV Motors), Ass.Prof. Gianmario Pellegrino (Politecnico di Torino) and Ass.Prof. Juliette Soulard (KTH Stockholm) for the valuable assistance and all the inspiring discussions.

Thanks also to all the wonderful people I met during my academic career in Catania, Torino, Stockholm and Västerås. They really made these years a colourful experience, which made me the person I am today.

Finally, I want to thank my parents for the inestimable education and support they always gave me and my brother which has always been an example to follow, even if younger.



Luigi Marino
Västerås, Sweden
February 2015

Contents

Acknowledgements	iv
Contents	v
List of Figures	viii
List of Tables	xi
1 Introduction	1
1.1 Background	1
1.2 Aims	1
1.3 Thesis outline	2
1.4 Note on the FEM simulation tool and method	2
2 Theory based on Literature Review	4
2.1 Fractional Slot Concentrated Windings	4
2.1.1 FSCW definition and dq Model Validation	4
2.1.2 Advantages and Drawbacks of Concentrated Windings	5
2.1.3 Possible Winding Configurations	5
2.1.4 Pole/Slot Combination	7
2.1.5 Layout design with the "Star of Slots" method	10
2.2 Magnetic Materials	12
2.3 Permanent Magnet assisted Synchronous Reluctance Motor (PMaSynRM)	15
2.3.1 Definition	15
2.3.2 Basic Structure of PMaSynRM	17
2.3.3 dq Model, Torque Production and Power Factor	17
2.3.4 Losses and Efficiency	21
2.4 Rotor Saliency Design	23
2.4.1 Single-Barrier Rotor Structure	23
2.4.2 Multi-Barrier Rotor Structure	24
2.4.3 Insulation Distribution in the Rotor Structure	28
2.4.4 Torque Ripple Minimization	29
2.4.5 Radial and Tangential Ribs	30
2.5 Permanent Magnets Optimal Insertion for Natural Compensation	31
2.6 Flux-Weakening Operation	35
2.7 Iron Magnetization Characteristic	37

2.8 Conclusions	40
3 Initial Motor Design	41
3.1 Double layer concentrated Winding Design	41
3.2 Analytical dimensioning of the motor	44
3.2.1 Dimensionign of rotor and stator parameters	44
3.3 SynRM 1 Design	47
3.4 Comparison with distributed winding motor	49
3.5 Conclusions	51
4 SynRM Design Optimization and Refinement	52
4.1 Optimization of stator winding number of turns per slot	52
4.2 Electric and magnetic load optimization	53
4.3 Average reluctance torque optimization	55
4.4 Torque ripple optimization	56
4.5 Slot opening optimization	58
4.6 Conclusions	62
5 Permanent Magnets Insertion	63
5.1 Nature of the problem	63
5.2 Natural compensation	64
5.3 Over compensation	66
5.4 Minimum and maximum allowed compensation	68
5.4.1 Flux weakening capability limit	68
5.4.2 Risk of demagnetization limit	70
5.5 PMaSynRM design	71
5.6 Thermal aspects and model refinement	74
5.7 Motor Dimension Reduction	75
5.8 PMaSynRM with Ferrite	76
5.9 Conclusions	77
6 Alternative Motor Designs	78
6.1 V-shaped IPM topology	78
6.2 SMPM topology	78
6.3 8-pole PMaSynRM	80
6.3.1 NdFeB assisted motor	82
6.3.2 Ferrite assisted motor	82
6.4 Performance analysis and comparison method	84
6.5 Topology comparison	87
6.5.1 Rated point	88
6.5.2 Overspeed	90
6.5.3 Overload	92
6.6 Slot/pole combinations comparison	92
6.6.1 Rated point	93
6.6.2 Overspeed	94
6.6.3 Overload	94
6.7 PM materials comparison	97
6.7.1 Rated point	99

6.8 Influence of the load angle	101
6.9 General comparison	102
7 Conclusions and Future Work	106
7.1 Conclusions	106
7.2 Future Work	106
Bibliography	108

List of Figures

2.1 a)Distributed winding b)Overlapping concentrated winding c)Non-overlapping double-layer concentrated winding d)Non-overlapping single-layer concentrated winding [11]	6
2.2 Different pole/slot combinations fundamental winding factor for concentrated winding [1]	8
2.3 Different pole/slot combination lowest common multiples [1]	8
2.4 Different pole/slot combination great common divisors [1]	9
2.5 a)Rotor losses map with double-layer winding b)Rotor losses map with single-layer winding [5]	10
2.6 a) $Q = 9$ and $p = 8$ motor star of slots b) $Q = 12$ and $p = 8$ motor star of slots [4]	11
2.7 Hard magnetic material hysteresis loop	13
2.8 Demagnetization curve of a ferrite magnet at $-40^{\circ}C$ [12]	13
2.9 VACODYM 890 AP typical demagnetization curve [9]	14
2.10 a)IPM motor with tangential exitation b)IPM motor with radial exitation [6]	16
2.11 PMaSynRM motor[6]	16
2.12 Magnetic torque principle	18
2.13 Saliency torque principle and field distortion [2]	18
2.14 PMaSynRM vectorial diagram [7]	19
2.15 PMaSynRM d-q equivalent circuits [7]	20
2.16 One-barrier geometry with macroscopic parameters [23]	24
2.17 k-th segment and related pu magnetic potential [6]	25
2.18 k-th segment equivalent magnetic circuit [6]	26
2.19 k-th segment equivalent pu magnetic circuit [6]	27
2.20 Multi-barrier geometry with the imaginary point B [23]	30
2.21 Radial and tangential ribs	31
2.22 a)Linearised barrier geometry b)Equivalent magnetic circuit [28]	32
2.23 PM area dependence on the PM thickness (ribs are neglected) [28]	34
2.24 Ideal field weakening characteristics. a) Torque b) Power [13]	36
2.25 a) Current and b) flux trajectories for maximum torque control in PMaSynchRM [14]	37
2.26 Parameters plane with motor topologies and normalized power characteristics [15]	38
2.27 Permanent magnet machines design space [7]	38
2.28 Measure magnetic characteristic for a four poles PMaSynRM [6]	39
2.29 MTPA loci for a four poles PMaSynRM, with(red) and without (blue) cross saturation	40

3.1	Star of slots for a double-layer concentrated winding with $Q = 12$ and $p = 10$	42
3.2	First winding layer positioning	42
3.3	Winding layout for a double-layer concentrated winding with $Q = 12$ and $p = 10$	42
3.4	Theoretical MMF distribution along the air-gap and its space harmonic spectrum for the winding depicted in Fig.3.3	43
3.5	Stator slot diameter D_{sl}	46
3.6	Output torque versus the ratio of the slot inner and outer diameters [20]	46
3.7	SynRM 1 geometry	48
3.8	SynRM 1 flux density and flux lines at nominal load	49
3.9	SynRM 1 Air-gap flux density and MMF spectra in p.u. with reference to the fundamental harmonics	50
3.10	SynRM 1D geometry	50
3.11	SynRM 1D flux density and flux lines at nominal load	51
4.1	Efficiency and power factor variation with the effective number of conductors per slot in SynRM 1	53
4.2	Efficiency and power factor variation with the stator slot dimensions	54
4.3	Efficiency and power factor variation with the rotor insulation ratio in SynRM 3	56
4.4	Torque ripple dependence with the imaginary number of barriers	57
4.5	Optimized geometry for torque ripple	58
4.6	Efficiency and power factor variation with the stator slot opening in SynRM 5	59
4.7	SynRM 5 and SynRM 6 slot openings	59
4.8	SynRM 6 geometry	60
4.9	SynRM 6 flux distribution at nominal load	61
4.10	SynRM 6 Air-gap flux density and MMF spectra in p.u. with reference to the fundamental harmonics	61
5.1	NdFeB 493a [30]	64
5.2	q-axis fundamental stator MMF and the relative staircase distribution in the rotor	65
5.3	Optimal magnet thickness-width ratio dependence on the q-axis flux	68
5.4	PMaSynRM 1 motor geometry	72
5.5	PMaSynRM 1 flux lines and flux density distribution at nominal load	73
5.6	PMaSynRM 1 Air-gap flux density and MMF spectra in p.u. with reference to the fundamental harmonics	73
5.7	Employed ferrite magnetization curve [31].	76
6.1	V-shaped IPM motor geometry, flux density and flux lines at rated working point	79
6.2	V-shaped IPM motor loss distribution at rated working point and magnet temperature at 70 °C	79
6.3	SMPM motor geometry, flux density and flux lines at rated working point	80
6.4	SMPM motor loss distribution at rated working point and magnet temperature 70 °C	81

6.5	8-pole SynRM motor geometry, flux density and flux lines at rated working point	82
6.6	8 poles PMaSynRM motor geometry, flux density and flux lines at rated working point	83
6.7	8 poles PMaSynRM motor loss distribution at rated working point and magnet temperature 70 °C	83
6.8	8-pole PMaSynRM Ferrite motor geometry, flux density and flux lines at rated working point	84
6.9	8-pole PMaSynRM Ferrite motor loss distribution at rated working point and magnet temperature 70 °C	85
6.10	Simulated load/speed combinations and torque curve	86
6.11	NdFeB 493a and NMF-7F Ferrite minimum permanent magnets flux density dependence with the temperature	87
6.12	PMaSynRM 10-pole simulated at rated point and ambient temperature of 195 °C	88
6.13	Efficiency comparison at rated point for different topologies	88
6.14	Power factor comparison at rated point for different topologies	89
6.15	Current comparison at rated point for different topologies	89
6.16	Efficiency comparison at 3000 rpm for different topologies	90
6.17	Power factor comparison at 3000 rpm for different topologies	91
6.18	Current comparison at 3000 rpm for different topologies	91
6.19	Efficiency comparison at 1.5 pu load for different topologies	92
6.20	Power factor comparison at 1.5 pu load for different topologies	93
6.21	Current comparison at 1.5 pu load for different topologies	93
6.22	Efficiency comparison at rated point for different poles/slots combinations .	94
6.23	Power factor comparison at rated point for different poles/slots combinations .	95
6.24	Current comparison at rated point for different poles/slots combinations .	95
6.25	Efficiency comparison at 3000 rpm for different poles/slots combinations .	96
6.26	Power factor comparison at 3000 rpm for different poles/slots combinations .	96
6.27	Current comparison at 3000 rpm for different poles/slots combinations .	97
6.28	Efficiency comparison at 1.5 pu load for different poles/slots combinations .	97
6.29	Power factor comparison at 1.5 pu load for different poles/slots combinations .	98
6.30	Current comparison at 1.5 pu load for different poles/slots combinations .	98
6.31	Efficiency comparison at rated point for different PM materials	99
6.32	Power factor comparison at rated point for different PM materials	99
6.33	Current comparison at rated point for different PM materials	100
6.34	Overload capability analysis for the studied motor designs at ambient temperature of 25 °C	101
6.35	General overview of all the studied motor designs	103
6.36	Main flux orientation in the designed PMaSynRM	105

List of Tables

2.1	Main characteristics for different windings configurations (1: smaller/shorter 2: medium 3: larger/longer) [1]	7
3.1	Typical shear stress value for electrical machines [21]	45
3.2	SynRM 1 FEM simulation output parameters	48
3.3	SynRM 1D FEM simulation output parameters	49
4.1	SyRM 2 performance	53
4.2	SyRm 3 performance (time-stepping FEM)	55
4.3	SyRM 4 performance (time-stepping FEM)	57
4.4	SynRM 5 performance (time-stepping FEM)	58
4.5	SynRM 6 performance (time-stepping FEM)	60
5.1	Rotor flux barriers linearised geometric data	64
5.2	Permanent magnets optimal dimensions for natural compensation	66
5.3	Optimal magnet thickness and width values for natural compensation, demagnetization risk limit and flux-weakening capability limit	71
5.4	PMaSyRM 1 performance	72
5.5	Dimension reduction	75
5.6	PMaSyRM 2 performance	75
5.7	PMaSyRM with ferrite performance	76
6.1	V-shaped IPM geometrical and performance data at ambient temperature 25°C	80
6.2	SMPM geometrical data and performance data at ambient temperature 25°C	81
6.3	8-pole SynRM geometrical and performance data at ambient temperature 25°C	82
6.4	8 poles PMaSynRM geometrical data and performance data at ambient temperature 25°C	84
6.5	8-pole PMaSynRM Ferrite geometrical and performance data at ambient temperature 25°C	85
6.6	Torque ratio R_T for the considered motors	102
6.7	General motor designs comparison	103
6.8	Permanent magnets effectiveness and resistance to demagnetization at rated point	104

To my family

Chapter 1

Introduction

1.1 Background

Nowadays, energy efficiency is one of the main concern in industry. Environmental and economic reasons stand for the basis for this energy saving willingness. It is well known that electrical motors utilize the main part of the total energy consumption in the world. For this reason, strong efforts are made by the research centers, from the academic and industrial world, to find new solutions and improve the already known motor topologies.

The general industrial trend is to substitute the induction motors, largely installed in the past decades, with permanent magnet synchronous motors, typically characterized by higher efficiency and torque density. Moreover, Permanent Magnet (PM) machines allow to eliminate the need of a gearbox in many applications, thus the drive gains simplicity and reliability. It is important to point out that the industrial utilization of synchronous motors was made possible, thanks to the recent power electronics technology development, since this kind of motors needs to be frequency-controlled.

As of today, there is a lack of research work on fractional slot concentrated wound PM machines combined with anisotropic rotor structure. This project work is an attempt to contribute to the common knowledge on the mentioned rotor topology.

1.2 Aims

The main aim of this master thesis is to design and analyze a FSCW (Fractional Slot Concentrated Wound) PMaSynRM (Permanent Magnet assisted Synchronous Motor) motor for an industrial application and suitable for the following specifications:

- rated power up to 15 kW
- base speed of 1500 rpm
- maximum speed of 6000 rpm
- maximum electrical frequency of 500 Hz

The design and analysis procedures are carried out by means of both analytical and FEM-simulation tools. The final purpose is to have a clear understanding about the advantages and drawbacks of the motor under study, in comparison with the standard and other possible machine topologies.

1.3 Thesis outline

The thesis starts with an introduction on the basic theory where the more relevant contents found in the literature are presented (Chapter 2 *Theory and Literature review*). After that, the winding layout design and the initial motor dimensioning, based on analytical calculations, are treated (Chapter 3 *Initial Motor Design*) and the geometry optimization is performed as well as the parameters sensitivity analysis (Chapter 4 *SynRM Design Optimization and Refinement*). Once the SynRM motor has been optimized, a magnet insertion strategy is proposed and the motor geometry is re-optimized (Chapter 5 *Permanent Magnets Insertion*). Subsequently, in order to give a general overview of the problem, different alternative motor designs are proposed, the performance analysis of all the considered motors is performed and a structured comparison is presented (Chapter 6 *Alternative Designs*). Lastly, a general comparison, including cost aspects, is presented and final conclusions are stated (Chapter 7 *Conclusions and Future Work*).

1.4 Note on the FEM simulation tool and method

All the investigations in this work have been performed by means of a 2D FEM analysis, using the software FCSmek. In this program, it is possible to select two different simulation profiles, namely

- harmonic/magneto-static
- time stepping/transient

The latter is relatively more time consuming, but also provides results which are more reliable and gives the possibility to regulate the grade of precision by selecting the number of steps per period. The harmonic/magneto-static calculation does not consider all the harmonics involved in the parasitic loss computation and the rotor movement.

Adept, a ABB parametric interface tool, has been employed in order to facilitate the usage of the above mentioned tool. It gives the possibility to customize the simulation profile and choose several options to improve the simulation flexibility.

Moreover, it is possible to set up Adept to the option "nominal point". This option chooses the optimal current angle on the basis of the specified power and speed and on the performance the motor has for each current angle. This option is used in all the simulations in this work.

Chapter 2

Theory based on Literature Review

In this chapter, the literature review carried out in the preliminary part of the thesis work is presented and summarized. The intention is to give a general overview about many theoretical aspects involved in the project and a precise definition of the several technical solutions employed. The most relevant references are cited.

2.1 Fractional Slot Concentrated Windings

2.1.1 FSCW definition and dq Model Validation

Each winding layout, with Q slots, p poles and m phases, is characterized by the parameter:

$$q = Q/(mp) \quad (2.1)$$

The term "concentrated" has been traditionally referred to windings having $q = 1$. For this reason, in order to refer to non-overlapping winding with $q < 1$ and avoid any kind of misunderstanding, the term "concentrated" is not sufficient and should always be combined with "non-overlapping", "tooth" or "fractional slot". In other words, an overlapping winding can be either distributed or concentrated, while a non-overlapping winding can only be concentrated [1]. Non-overlapping windings with $q < 1$ will be referred to as Fractional Slot Concentrated Windings (FSCW) for the rest of this thesis report.

The dq theory, largely used to analyse permanent magnet motors, is based on two basic assumptions:

- sine-distributed winding
- linear magnetic behaviour

All the motors presented in this report are equipped with concentrated windings, hence both the two basic assumptions are violated. In any case, Soulard J. and Meier F. have shown in [36] that if the dq theory is applied to this type of motors, it is possible to estimate the steady state torque with a sufficient accuracy if the motor is not affected by saturation. Thus, hereafter, all the model considerations of the concentrated winding motor, are based on the dq theory.

2.1.2 Advantages and Drawbacks of Concentrated Windings

FSCW present several advantages and drawbacks compared to the distributed windings. First of all, FSCW require shorter end-winding connections. It means that a certain amount of copper is saved (as well as joule losses) and the machine total length is reduced for the same active length. Moreover, one of the key advantages of FSCW is the possibility to achieve higher slot fill factor. This may lead to an important impact on the machine power density. On the other hand, concentrated windings produce a non-sinusoidal flux distribution along the air-gap compared to distributed. As a result, larger iron losses are produced in machines with FSCW due to the harmonic flux distribution components. Having such a non-sinusoidal distribution can be, in some application, a desired feature. In fact, all these harmonic components increase the machine leakage inductance and, as a consequence, increase the flux weakening capability. Another important advantage, of the FSCW, is the possibility to design the motor with a large Least Common Multiple (LCM) between the number of poles and the number of slots, in order to obtain a low cogging torque. Lastly, FSCW are characterized by reduced manufacturing costs. A schematic comparison between distributed, overlapping concentrated and non-overlapping concentrated windings is depicted in Fig. 2.1 [11].

2.1.3 Possible Winding Configurations

It is possible to realize FSCW in two different constructive structures:

- Single-layer, with coils wound only on alternate teeth

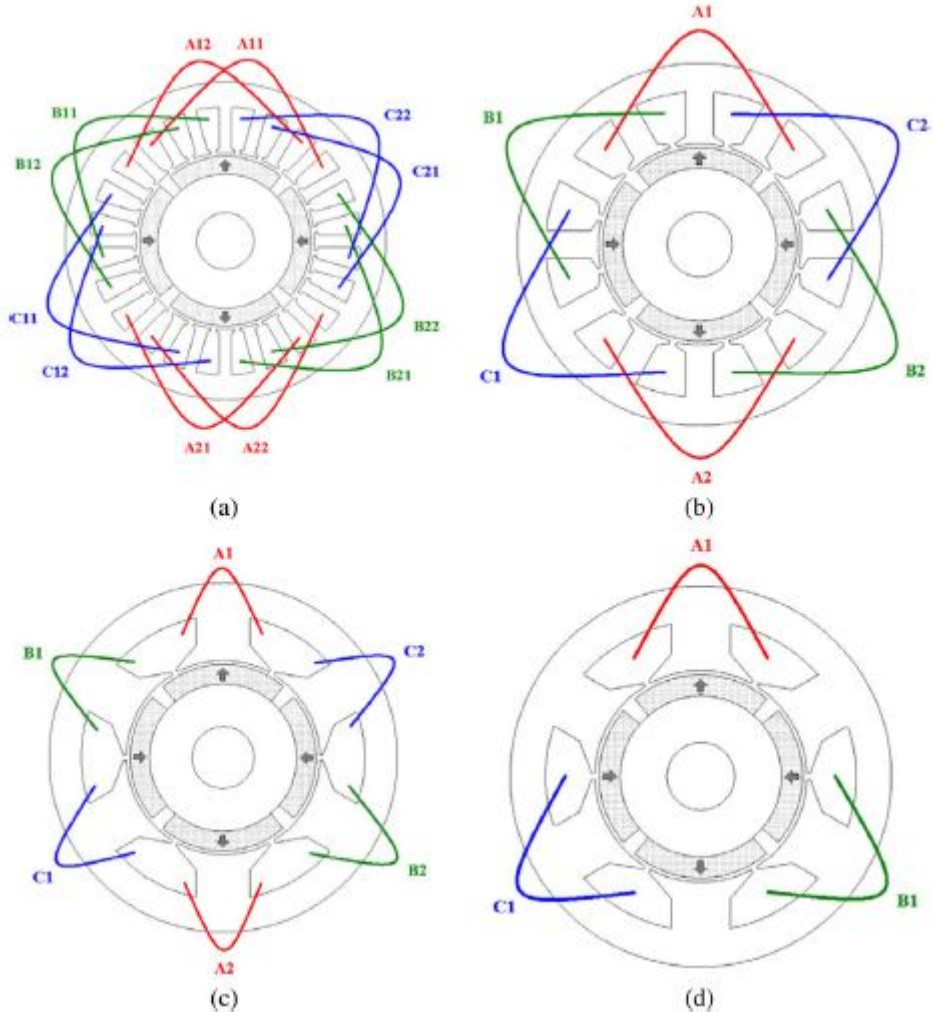


FIGURE 2.1: a)Distributed winding b)Overlapping concentrated winding c)Non-overlapping double-layer concentrated winding d)Non-overlapping single-layer concentrated winding [11]

- Double-layer, with coils wound on each tooth

The two kinds of concentrated winding configuration present different features, hence they are suitable for different applications. The main characteristics of single-layer concentrated winding, double-layer concentrated windings and distributed windings are summarized in Table 2.1. Moreover, the single-layer arrangement has a higher fault-tolerance due to the well isolated phases from a thermal, electrical and magnetic (higher self-inductance but lower mutual-inductance) point of view [1] since only conductors from same phases are placed in one slot.

TABLE 2.1: Main characteristics for different windings configurations (1: smaller/shorter 2: medium 3: larger/longer) [1]

Winding Configuration	Single-layer	Double-Layer	Distributed
Fundamental winding factor	1	2	3
End-windings lenght	2	1	3
Slot fill factor	3	2	1
Self-inductances	3	2	1
Mutual-inductances	1	2	3
MMF harmonic content	3	2	1
Eddy current losses	3	2	1
Overload torque capability	3	2	1

2.1.4 Pole/Slot Combination

When a concentrated winding has to be designed, the first choice to be made is the number of layers, according to the characteristics described above and depending on the application. Later on, the pole/slot combination has to be decided. The required nominal speed and frequency give an idea on the possible number of poles. However, this choice should be made on the basis of many other considerations. In fact, in literature it is possible to find the effect of pole/slot combination on several important parameters such as

- fundamental winding factor
- cogging and torque ripple
- vibrations
- rotor losses
- inductances

The fundamental winding factor is desired to be as high as possible in order to maximize the torque production with the same amount of current fed into the stator. It expresses the disposition effectiveness of the conductors, hence how efficiently they interact with the flux wave. The table shown in Fig. 2.2, extracted from [1], summarizes the different pole/slot combination fundamental winding factors for concentrated windings.

As mentioned above, an important characteristic is the torque ripple, when the pole/slot combination has to be chosen. The cogging torque is one of the torque ripple contributions and it can be reduced by choosing a proper pole/slot combination. However, a low cogging torque does not ensure a low torque ripple. The cogging torque is due to the

Q_s/p	4	6	8	10	12	14	16	18	20	22	24	26	28	30	32	34	36	38	40
6	0.866		0.866	0.5		0.5	0.866		0.866	0.5		0.5	0.866		0.866	0.5		0.5	0.866
9	0.617	0.866	0.945	0.945	0.866	0.617	0.328		0.328	0.617	0.866	0.945	0.945	0.866	0.617	0.328		0.328	0.617
12	$q=1$		0.866	0.933		0.933	0.866								0.866	0.933		0.933	0.866
15			0.621	0.866		0.951	0.951		0.866	0.621								0.621	0.866
18		$q=1$		0.647	0.866	0.902	0.945		0.945	0.902	0.866	0.647							
21						0.866	0.89		0.953	0.953		0.89	0.866						
24			$q=1$			0.76	0.866		0.933	0.95		0.95	0.933		0.866	0.76			
27							0.866	0.877	0.915	0.945	0.954	0.954	0.945	0.915	0.877	0.866			
30			$q=1$					0.866	0.874		0.936	0.951		0.951	0.936		0.874	0.866	
33									0.866		0.903	0.928		0.954	0.954		0.928	0.903	
36										0.866	0.867	0.902	0.933	0.945	0.953		0.953	0.945	
39											0.866	0.863		0.918	0.936		0.954	0.954	
42						$q=1$					0.866			0.89	0.913		0.945	0.953	
45												0.866	0.859	0.886			0.927	0.945	
48						$q=1$						0.866	0.857				0.905	0.933	
51													0.866				0.88	0.901	
54						$q=1$										0.866	0.854	0.877	
57																	0.866	0.852	
60							$q=1$											0.866	

$q=1/2, 1/4$	$q=3/8, 3/10$	$Q_s=21+6k, p=Q_s\pm 1, k = 0, 1, 2 \dots$
$q=3/7, 3/11$	$q=5/14, 5/16$	$Q_s=24+6k, p=Q_s\pm 2, k = 0, 1, 2 \dots$
$q=2/5, 2/7$	not appropriate	$k_{Wf} < 0.866$

FIGURE 2.2: Different pole/slot combinations fundamental winding factor for concentrated winding [1]

variation of the magnetic permeance seen by the permanent magnets due to the presence of the slots on the stator surface (localized anisotropy). It does not depend on the stator excitation. In [1], it is said that the larger the Least Common Multiple (LCM) between the number of slots and poles, the lower the resulting cogging torque. The table shown in Fig. 2.3, extracted from [1], summarizes the different pole/slot combination LCMs. Also, there are other means to reduce the torque ripple, as stator or rotor skewing and control-based techniques [8].

Q_s/p	4	6	8	10	12	14	16	18	20	22	24	26	28	30	32	34
6	12		24													
9		18	72	90	36											
12			24	60		84	48									
15				30		210	240		60							
18					36	126	144		180	198	72					
21						42	336		420	462		546	84			
24							48		120	264		312	168		96	
27								54	540	594	216	702	756	270	864	918
30									60	330		390	420		480	510
33										66		858	924		1056	1122
36											72	468	252	180	288	612

FIGURE 2.3: Different pole/slot combination lowest common multiples [1]

Until now, the influence of the pole/slot combination on the winding factor and hence on the torque (i.e. tangential forces) produced on the rotor, has been presented. Unfortunately, unbalanced radial forces are also created for some pole/slot combinations. This situation is to be avoided because of the eventual vibrations and noise production.

The so-called "unbalanced magnetic pull" is a consequence of the winding asymmetry, without considering the conductors orientation. In [1], it is said that if the great common divisor (GCD) between the number of slots and poles is unitary, the machine is subjected to unbalanced magnetic pull. Thus, these pole/slot combinations are to be avoided. The table shown in Fig. 2.4, extracted from [1], summarize the different pole/slot combination GCDs.

Qs/p	4	6	8	10	12	14	16	18	20	22	24	26	28	30	32	34
6	2		2													
9		3	1	1	3											
12			4	2	2	2	4									
15			5		1	1		5								
18				6	2	2		2	2	6						
21					7	1		1	1		1	7				
24						8	4	2		2	4		8			
27							9	1	1	3	1	1	3	1	1	
30								10	2	2	2	2		2	2	
33									11		1	1		1	1	
36										12	2	4	6	4	2	

FIGURE 2.4: Different pole/slot combination great common divisors [1]

The rotor iron losses are also influenced by the pole/slot combination, since it determines the space harmonic spectrum of the MMF (due to the discrete positioning of the stator conductors) [5]. These harmonics, moving asynchronously with respect to the rotor, induce currents in the rotor conductive parts. The variation of rotor flux is due to the MMF harmonics and the slotting effect. A proper choice of the pole/slot combination can make a difference to greatly reduce the former. The number of the fundamental harmonic (the one synchronous with the rotor) coincides with the number of pole pairs. It is possible to state that sub-harmonics are responsible for the greater part of the rotor losses. This can be justified by saying that the sub-harmonic waves are wider than the fundamental and thus the corresponding flux passes deeply inside the rotor. Moreover, these sub-harmonics have a rotation speed higher than the synchronous (the rotation speed is inversely proportional to the harmonic order). All the above considerations are shown in Fig. 2.5, where the double-layer and single-layer machines behaviours are described. Starting from Fig. 2.5 a), it is possible to say that for double-layer windings the lower rotor losses are located along the thick line where (indicated by the arrows)

$$Q/p = m = 3 \quad (2.2)$$

with m , the number of phases. With this configuration there are no sub-harmonics. Elsewhere, the rotor losses are higher but they do not increase monotonically as the machine design moves from the above mentioned line. In fact, there are several local minima, marked with circles, along the lines characterized by

$$Q/p \simeq 2.5 \quad (2.3)$$

and

$$Q/p = 1.5 \quad (2.4)$$

Fig. 2.5 b) describes with the same manner the way the single-layer winding is affected by rotor losses. In this case, there are some non feasible combinations (refer to the rules and the conditions to transform a double-layer to a single-layer winding described in [4]).

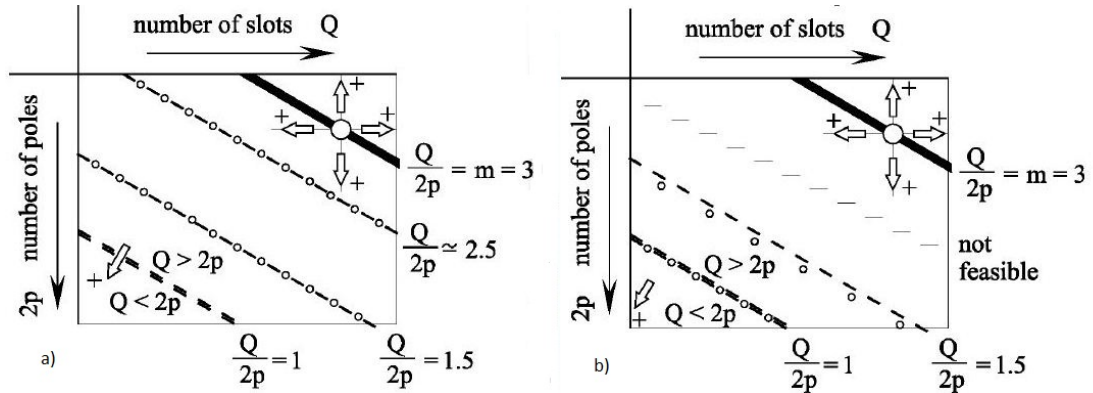


FIGURE 2.5: a)Rotor losses map with double-layer winding b)Rotor losses map with single-layer winding [5]

Moreover, if the rotor topology is already fixed, it may give further indications. For example, if the designer aims to realize a PMaSynchRM, a 2-pole machine has to be avoided as it is not possible to realize a proper anisotropic structure. This is because of the presence of the shaft which introduces a bad quality magnetic material in the natural flux path. The 4-pole machine is preferred for most applications [2].

2.1.5 Layout design with the "Star of Slots" method

Once the pole/slot combination has been fixed, it is possible to follow different methods in order to obtain the winding layout. A suitable one is the "Star of Slot Method" [4]. This method is intended to obtain:

- the maximum fundamental winding factor
- an equal EMF waveform for each phase, with

- an angular displacement of $2\pi/m$ electrical radians between the phases (where $/m$ is the number of phases)

”The star of slot is the phasor representation of the main EMF harmonic induced in the coil side of each slot” [4]. It is composed by $Q/GCD(Q, p/2)$ spokes, one for each slot, with an angle between two consecutive spokes of $\pi p/Q$. Two examples are given in Fig. 2.6, taken from [4].

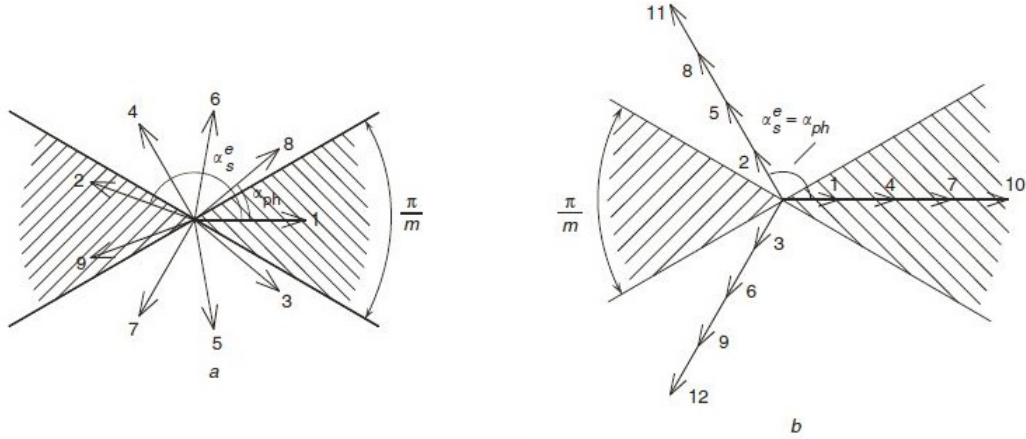


FIGURE 2.6: a) $Q = 9$ and $p = 8$ motor star of slots b) $Q = 12$ and $p = 8$ motor star of slots [4]

It is also important to check the feasibility of the winding. The condition for the winding feasibility is that the ratio $Q/(m GCD(Q, p/2))$ is an integer.

The phasor belonging to the same phase are determined by superimposing to the star of slots two opposite sectors, with a π/m span each. These two sectors are shown in Fig. 2.6, where $m = 3$. One of the two sectors gives positive and the other one negative polarity. In order to assign the rest of the phase, it is sufficient to rotate the two sectors with an angle of $2k\pi/m$ radians, where $k = 1, 2, \dots, (m - 1)$ and repeat the process. From the obtained star of slots, it is possible to determine the layout of a double-layer winding. If a single-layer winding is desired, all the even phasors must be removed from the star of slots. However, some constraints have to be respected in order to be able to operate the star of slots transformation which leads to a single-layer winding. There are geometrical and electrical constraints. The geometrical constraints are that the number of slots must be even and the slot pitch must be odd, the electrical constraint (only if the star of slots has an odd number of phasors per spoke) is that $Q/GCD(Q, p/2)$ must be even.

2.2 Magnetic Materials

The magnetic materials behaviour and performance are described by three different parameters:

- Flux Density or Magnetic Induction \mathbf{B} [T]
- Magnetic field \mathbf{H} [A/m]
- Magnetization \mathbf{M} [A/m]

These parameters are vectors that describe respectively the flux density at a point in space, the field created by a field source and the magnetic state of the material(result of the individual atomic magnetic moments). These vectors are related, in free space, by the following law:

$$\mathbf{B} = \mu_0 \mathbf{H} + \mu_0 \mathbf{M} = \mu_0 \mathbf{H} + \mathbf{J} \quad (2.5)$$

where \mathbf{J} [T] is called Polarization [6].

A common feature among all the magnetic materials is their non-linear behaviour. In fact, the magnetic permeability $\mu = \mu_0 \mu_R$ is not a constant value, but it actually depends on the level of magnetic induction in the considered material portion. The way μ varies is described by the typical magnetic hysteresis loop (with a large internal area for "hard magnetic materials", or permanent magnet, and a small internal area for "soft magnetic materials") as shown in Fig. 2.7. The curves are experimentally obtained by applying a sufficiently strong magnetic field to saturate the material in both directions.

Some relevant quantities from Fig. 2.7 are listed below:

- Remanence flux density B_r
- Coercitive magnetic field H_{ci}
- Saturation flux density B_{sat}
- Saturation magnetic field H_{sat}

The B-H curve also provides the energy product $(BH)_{max}$ i.e., the greatest BH product in the second quadrant. The B-H combination that gives $(BH)_{max}$ represents the best magnet working point in terms of energy density.

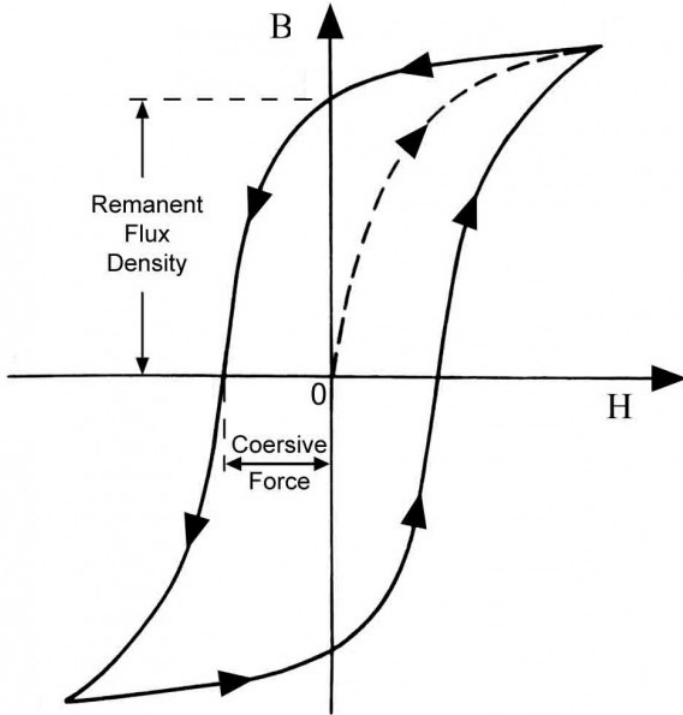
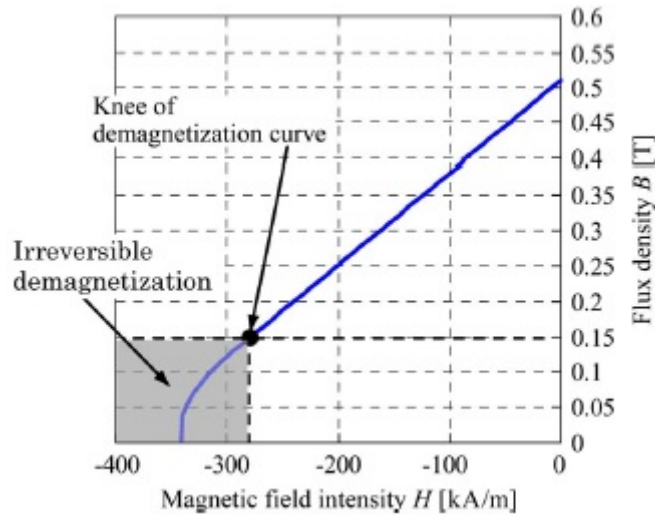


FIGURE 2.7: Hard magnetic material hysteresis loop

It is important to notice that when the magnet working point goes down from the positive saturated condition (first quadrant) and overcomes the knee (second quadrant) the magnet gets demagnetized, as shown in Fig.2.8 [12]. It means that, at this point, if the applied magnetic field is increased again, the magnet working point follows a lower trajectory ("recoil line"). This trajectory ends at the right-hand side of the hysteresis loop, hence the magnet remains demagnetized until it is saturated again in the positive direction.

FIGURE 2.8: Demagnetization curve of a ferrite magnet at $-40^{\circ}C$ [12]

For electrical machine applications, all the relevant information about the permanent magnet are summarized in the second quadrant. An industrial example of NdFeB is given in Fig. 2.9, taken from [9].

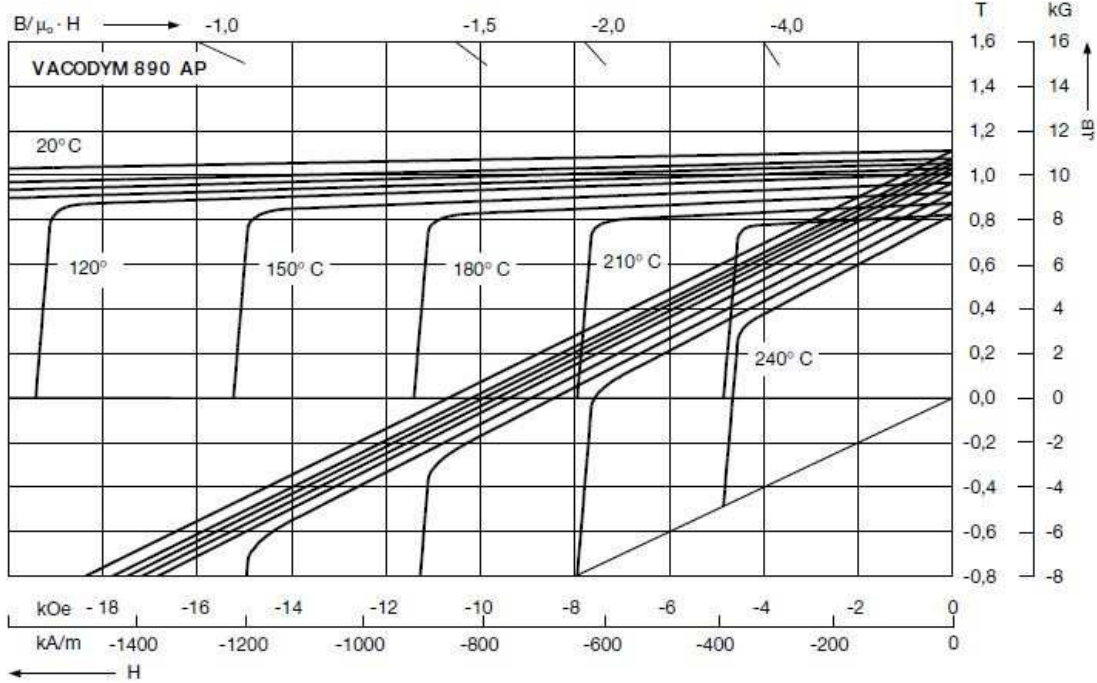


FIGURE 2.9: VACODYM 890 AP typical demagnetization curve [9]

Today, the most employed permanent magnets for electrical machines are:

- Ferrite
- Neodymium Iron Boron (NeFeB)
- Samarium Cobalt (SmCo)

With a material cost of approximately 6 [USD/Kg] [34], ferrite magnets are the cheapest but they also have the lowest $(BH)_{max}$. They show a decrement of B_r and a increment of H_{ci} as the temperature goes up, hence a negative thermal coefficient for B_r and positive for H_{ci} . Their maximum operating temperature is typically 200°C. NdFeB, on the other hand, is characterized by the highest remanence flux density and energy product, but it is currently the most expensive (83 [USD/Kg] [33]). For this material, both B_r and H_{ci} decrease as the temperature increases. A valid alternative to NdFeB is represented by SmCo, because of the exceptionally high H_{ci} and a relatively low temperature coefficient for B_r (still negative). Moreover, SmCo is resistant to corrosion but more difficult to be manufactured [6]. Furthermore, because of the temperature dependences mentioned above, ferrites demagnetize much easily at low temperatures and rare earth magnets at high temperatures.

The permanent magnet material selection is then made depending on the application. Many efforts have been made by the scientific community to extend the use of ferrite instead of the rare-earth magnets (the latter not only have a higher price, but the availability is also more unstable because of international market issues) [6].

2.3 Permanent Magnet assisted Synchronous Reluctance Motor (PMaSynRM)

2.3.1 Definition

A Permanent Magnet assisted Synchronous Reluctance Motor (PMaSynRM) is an electric motor that produces both reluctance torque (thanks to the rotor anisotropy) and electro-dynamic torque (thanks to the rotor excitation, in this case due to the permanent magnets). However, in the literature, this is not the only motor topology that corresponds to this definition. In fact, the Internal Permanent Magnet (IPM) motor also produces both the above mentioned torque components. However, it is possible to distinguish these two different motor topologies by considering their typical optimization procedures and their prevalent torque contribution. The PMaSynRM is simply a SynRM with a certain amount (usually quite limited) of permanent magnets providing a magnetic flux in the negative direction of the q-axis, see Fig.2.10 and 2.11. It means that this kind of topology is first of all optimized in order to obtain as much reluctance torque as possible. Then, by introducing the permanent magnets in the rotor structure, it is possible not only to have a secondary torque component but also to increase the power factor which is typically quite low in SynRM motors. On the contrary, the IPM motor is characterized by a prevalent torque component due to the permanent magnets and a secondary torque component due to the low anisotropy. In this case, the rotor saliency is not optimized as it was for the PMaSynRM, but it exists only because of the low magnetic permeance of the permanent magnets buried into the rotor structure [2]. In this thesis the d-axis is defined as the axis with the main flux (and maximum inductance) and not as the axis where the magnet flux is directed, as it is for the IPM motor.

The PMaSynRM are suitable for many applications for several reasons. Drives with PMaSynRM have typically higher efficiency and torque density than Induction Motors (IM), even if they always require to be inverter-fed. Compared to SynRM, they have higher torque density, but primarily higher power factor, hence overdimensioning of power electronics is avoided. On the other hand, the permanent magnets add costs to the motor. IPM and SMPM motors are characterized by higher torque density, but

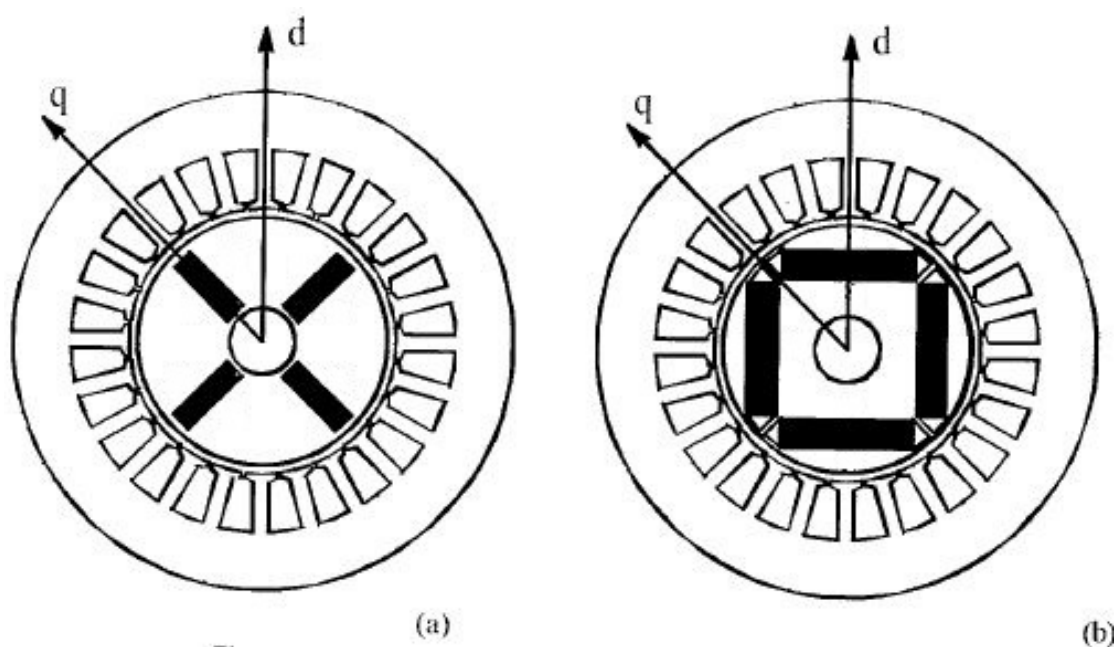


FIGURE 2.10: a)IPM motor with tangential excitation b)IPM motor with radial excitation[6]

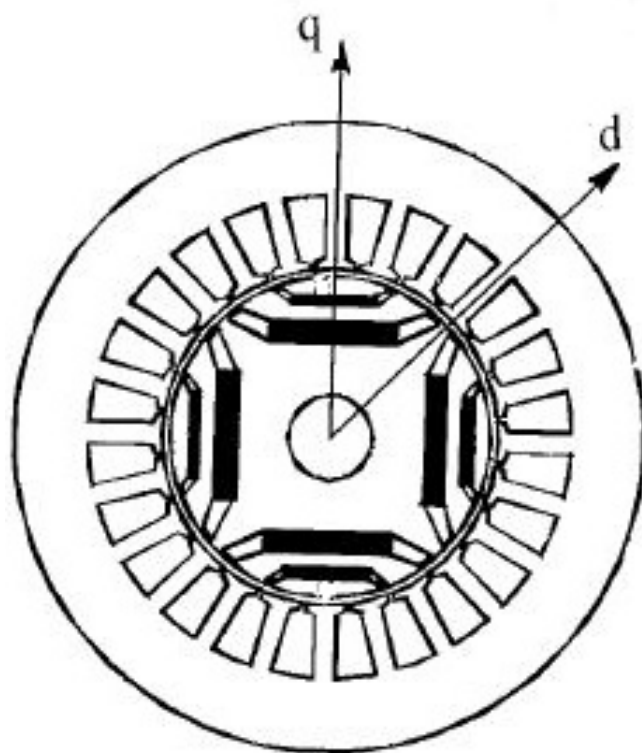


FIGURE 2.11: PMaSynRM motor[6]

their realization is more expensive due to the larger amount of permanent magnets in the rotor structure. Moreover, the larger the permanent magnets quantity, the worse is the flux-weakening capability. PMaSynRM are then very suitable especially for applications requiring flux-weakening operation. Not only because it is possible to obtain a wide constant power speed range, but also for the good overlaod capability in this kind of operation. Furthermore, the power factor which is typically high in the constant torque speed range, tends to become higher in flux-weakening operation [6]. Lastly, it is worth to point out that the rotor saliency gives the possibility to implement zero-speed sensorless control since a superimposed high-frequency excitation can allow to detect the anisotropic behaviour of the machine and lead to a position estimation [10].

2.3.2 Basic Structure of PMaSynRM

The stator structure of this kind of motor is exactly the same as in the IM, SMPM and IPM motors, what makes the difference is the rotor structure. The cross-sectional view is shaped in order to create air cavities called "flux barriers" (see Fig. 2.10 and 2.11). The intention is to realize a magnetic reluctance as high as possible for the q-direction and the contrary for the d-component of the flux. The permanent magnets are inserted in these free spaces. As mentioned in the previous paragraph, the magnet flux is directed in the negative direction of the q-axis in order to compensate the q-flux and maximize the anisotropy ratio.

2.3.3 dq Model, Torque Production and Power Factor

As stated earlier, the torque provided by a PMaSynRM is composed by two different contributions. Each of them is the result of a different torque production principle:

- magnetic torque
- reluctance torque

The magnetic torque principle is depicted in Fig. 2.12. If a magnet is immersed in a magnetic field, it experiences forces applied to his poles. These forces tend to attract opposite poles and work with opposite directions, producing a torque. The shape of the magnet is not relevant.

The reluctance torque has some similarities to the magnetic torque principle. A reluctance torque is produced wherever there is a magnetic field applied to a magnetically anisotropic object (the d-axis identifies the maximum while the q-axis identifies the

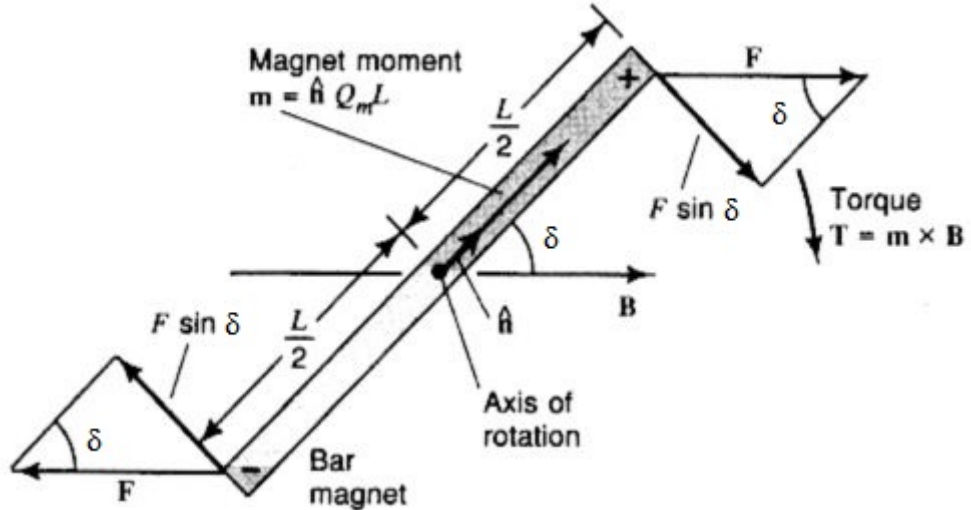


FIGURE 2.12: Magnetic torque principle

minimum permeance path). The torque is produced if there is a certain angle between the d-axis and the field lines. In other words, the imposed magnetic flux penetrates the object (a field distortion is introduced) and polarizes it. At this point the object behaves similarly to a permanent magnet.

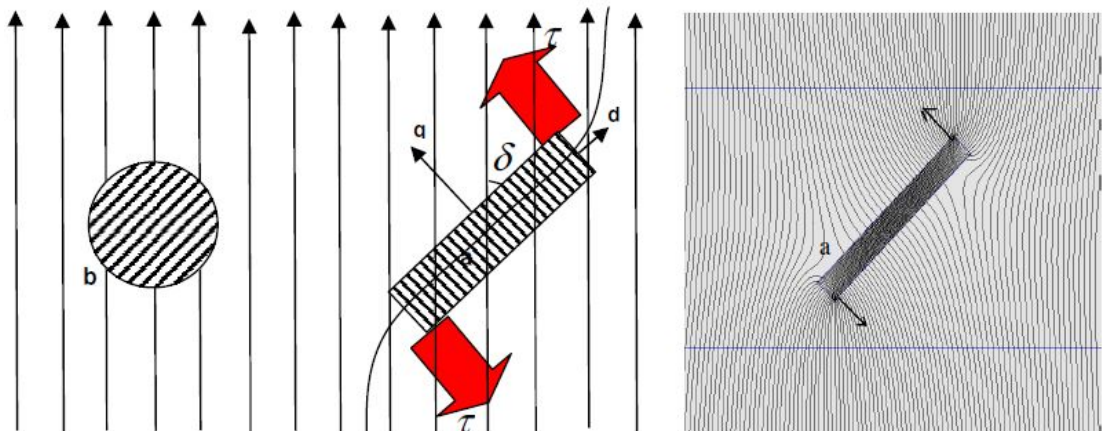


FIGURE 2.13: Saliency torque principle and field distortion [2]

In electrical machines, a rotating field that interacts with the rotor is produced by the stator windings. It is possible to state that the described system tends to reduce its potential energy (and field distortion) by means of the produced torque. If the stator current is controlled in such a way that the angle δ in Fig. 2.12 (where the vectors F represent the magnetic forces applied to the magnet poles) is maintained constant, a continuous torque production takes place [6]. δ is called "load angle", because it occurs when a mechanical load is connected to the object and it increases with the load until the maximum torque value is reached. However, the load angle for the maximum reluctance torque is 45° and for the maximum magnetic torque is 90° . It is important to say that

the reluctance torque varies sinusoidally with double the frequency with respect to the magnetic torque.

The PMaSynRM can be modelled using the following equations. The vectorial diagram and the d-q equivalent circuits are depicted in Fig. 2.14 and Fig. 2.15, respectively [7].

$$v = e + R_S i_{dq} \quad (2.6)$$

$$e = \frac{d\lambda_{dq}}{dt} + j\omega\lambda_{dq} \quad (2.7)$$

$$\lambda_{dq} = \lambda_{mdq} + \lambda_{rdq} \quad (2.8)$$

$$\lambda_{rdq} = L_{mdq} i_{dq} \quad (2.9)$$

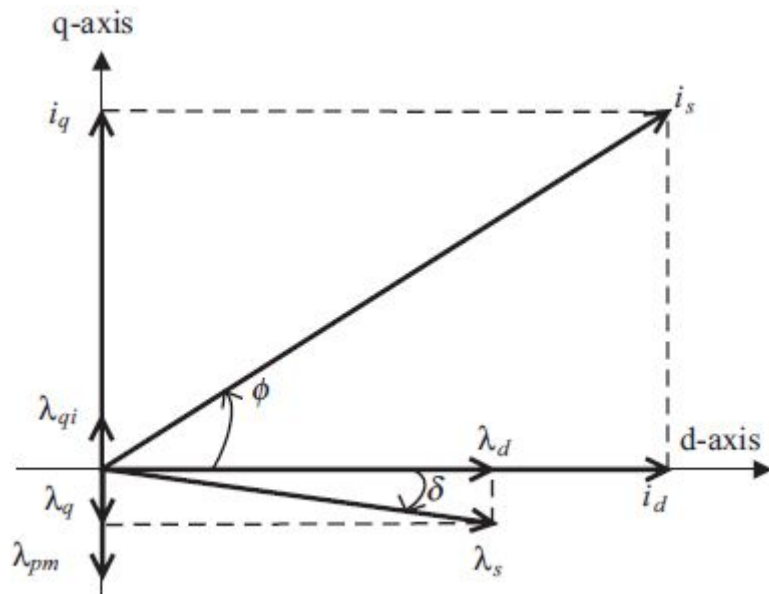


FIGURE 2.14: PMaSynRM vectorial diagram [7]

From the presented model, it is possible to extract the total torque and the internal power factor equation [2], expressed as function of d,q quantities:

$$T = \frac{3}{2}p((L_d - L_q)i_{dm}i_{qm} - \lambda_{PM}i_{dm}) \quad (2.10)$$

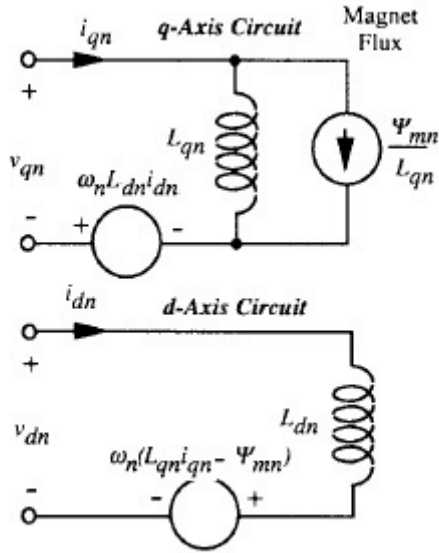


FIGURE 2.15: PMaSynRM d-q equivalent circuits [7]

$$IPF = \frac{\cos\theta((\xi - 1)\sin\theta - \frac{\lambda_{PM}}{L_q i_m})}{\sqrt{\xi^2 \cos^2\theta + (\sin\theta + \frac{\lambda_{PM}}{L_q i_m})^2}} \quad (2.11)$$

where, the saliency ratio is defined as

$$\xi = \frac{L_d}{L_q} \quad (2.12)$$

and θ is the current angle from the d-axis.

If the magnets flux fully compensates the undesired flux along the q-axis, the motor is called "naturally compensated". This condition is verified if

$$\lambda_{PM} = -L_q i_0 \quad (2.13)$$

where i_0 is the nominal current value. This is a particularly wanted design configuration because it allows to have an infinite constant power speed range (CPSR) operation always controlled with a MTPA strategy. Unfortunately, this condition can be perfectly achieved only in theory because of the magnet flux dependence on the temperature and the different possible operating conditions (the equation is defined for the nominal condition). However, a good grade of compensation, even if not perfect, gives the advantages discussed earlier.

It is possible to determine the value of λ_{PM0} , as described in [8], with the following expression:

$$\lambda_{PM0} = \frac{k_{w1}Qn_S}{6pC_S} DLB_{PM0} \quad (2.14)$$

where, k_{w1} is the fundamental winding factor, Q is the total stator slot number, n_S is the number of conductors per slot, D is the airgap diameter, L is the active length, C_S is the winding connection factor and B_{PM0} is the open circuit air-gap flux density. This equation is useful to estimate the PM flux with different material and amount of permanent magnets. The values of B_{PM0} can be calculated by means of FEM simulations [2].

2.3.4 Losses and Efficiency

The losses that occur in a PMaSynRM can be classified as:

- Copper losses P_{CU} , due to the Joule effect that the current produces in the stator windings (depending on the squared value of the current)
- Iron losses P_{FE} , composed mainly by hysteresis and eddy currents losses induced in the motor steel by time variation of the magnetic flux (depending on the flux density and frequency)
- PM losses P_{PM} , composed mainly by hysteresis and eddy currents losses induced in the PM material by time variation of the magnetic flux (depending on the flux density and frequency)
- Mechanical losses P_{mech} , due to mechanical phenomena as friction and viscosity (depending on the rotating speed)
- Stray losses P_{st} , include everything that is not accounted for in the traditional loss terms (i.e. extra losses that occur at load conditions compared to no-load in induction machines)

It is important to say that in variable speed drives (VSD) an extra amount of losses is present due to the time-harmonics introduced by the power electronic converter, controlled to drive the motor. In this thesis, this effect is neglected, since it goes beyond the purpose of this work, and only space-harmonics are taken into account.

It is of great interest to define a model for analytical calculation of iron losses. This is because the Finite Element Method (FEM) is often time too consuming for rapid

machine sizing and also it is useful for a better understanding of these phenomena. In the early attempts to model iron losses [16], a sinusoidal magnetic flux was assumed in the iron core of the motor. As stated in [17], this assumption may lead to a loss underestimation of 20 % and even larger for PM machines. The iron working point describes not simply an hysteresis loop, but a major hysteresis loop with many minor loops overlapped when the harmonic components of the magnetic flux occur. As a result, the loss is described by the summation of every hysteresis loop, the major and the minors. In [18], an improved model is proposed, accounting also for the harmonic components and the stator skewing. The general analytical expression of iron loss volume-density is:

$$P_{iron} = P_h + P_e + P_{exc} = k_{ch}k_h f B_m^\alpha + \frac{k_e}{2\pi^2} \left(\frac{dB}{dt} \right)_{rms}^2 + \frac{k_{exc}}{(2\pi^2)^{0.75}} \left(\frac{dB}{dt} \right)_{rms}^{3/2} \quad (2.15)$$

given in $[W/m^3]$. k_h , k_e and k_{exc} are material depending coefficients and can be empirically determined from the specific loss data of the specific lamination, usually provided by the manufacturer. Moreover, k_{ch} takes into accounts the effect of minor hysteresis loops. It is interesting to give state considerations about the iron losses also in flux-weakening operation. From 2.15, it is possible to say that, assuming the flux perfectly sinusoidal, the iron losses in flux weakening operation are smaller. It basically depends on the hysteresis loss term, where the maximum flux density (decreasing parameter in flux-weakening operation) has an higher exponent than the frequency (increasing parameter in flux-weakening operation). However, in real cases, when the flux density time variation is not sinusoidal, it is not possible to state this conclusion a priori. This fact is more evident in the following formula, taken from [19]

$$P_{iron} = \sum_{h=1}^N \pi(hf) B_h H_h \sin(\phi_h) \quad (2.16)$$

where f is the fundamental frequency, h the harmonic order, B_h and H_h the flux density and the magnetic field peak values of the h -th harmonic respectively, ϕ_h the angle between B_h and H_h . In equation 2.16, iron losses are calculated by applying Fourier analysis to flux density and magnetic field. In flux weakening condition, ideally, only the fundamental harmonic of the flux density (B_1) is reduced by the presence of the demagnetizing d-current, while f increases independently to the value of h . Hence, for $h > 1$, the product $B_h f$ tends to increase in flux weakening condition and to produce more losses.

At this point, the strategy to be adopted, in order to calculate the machine iron losses, is to analytically determine the flux density waveforms in all the machine regions from the air-gap flux waveform, as explained in [13] and then apply the model expressed in equation 2.15.

2.4 Rotor Saliency Design

The rotor saliency design of a PMaSynRM corresponds exactly to what is found in literature for SynRM, since the iron structure working principle is the same. From the previous paragraphs, it is straightforward that the rotor anisotropy is crucial for the motor performance. Thus, the rotor structure design mainly focuses on this aspect. In this part of the design and optimization process, the stator is supposed to be slot-less, hence no torque ripple is considered. The flux-barriers rotor structure is the state of the art of the technology in order to reach the highest saliency value. This configuration allows to reduce the q-axis inductance without excessively affecting the d-axis one [2]. This is because this geometry present an high air-gap from the q-axis and, at the same time, a large d-axis flux-path span.

After an analytical dimensioning, a FEM-based analysis is required to optimize the geometry and take into consideration the model simplifications. Afterwards, a fine tuning is still required. It mainly consists of

- reducing the number of barriers to a practical minimum
- rounding the sharp corners
- dimensioning and including the radial ribs

2.4.1 Single-Barrier Rotor Structure

The main macroscopic geometry parameter, for high saliency rotor structures, is the q-axis insulation ratio [2]

$$k_{wq} = \frac{W_{ins}}{W_{iron}} \quad (2.17)$$

where, W_{ins} is the sum of the widths of the flux barriers and W_{iron} is the sum of the widths of the iron paths in the rotor. If $k_{wq} = 0$, the rotor is solid and there is no saliency. In literature, other authors considered instead the total amount of insulation

in the q-axis [25]. In both cases, these parameters have important effects on the d- and q-axis inductances, hence on the average torque depending on $(L_d - L_q)$ and the power factor ($\xi = \frac{L_d}{L_q}$). It is the main variable affecting the rotor anisotropy. The flux barrier introduction in the rotor structure is intended to reduce the inductance L_q without affecting L_d . For this reason, it is of great interest to optimize this parameter in order to obtain the highest rotor saliency. A secondary optimization aspect, according to [2], is the radial position of the barriers in the rotor structure since it affects the average torque to a lesser degree. therefore, the radial position of each flux barrier can be chosen to improve the torque ripple since it allows to adjust the flux barriers ending points.

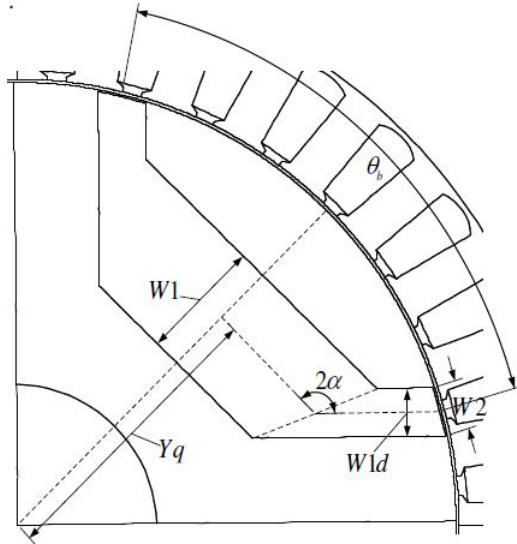


FIGURE 2.16: One-barrier geometry with macroscopic parameters [23]

In [2], the d-axis insulation ratio ($k_{wd} = \frac{W_{insD}}{W_{iron}}$) is said to be optimized in order to obtain the best performance (its optimum is smaller than k_{wq} if the machine has more than one pole pair). Moreover, it is suggested to perform the optimization procedures independently. Lastly, the angle α shown in figure 2.16 is found to be optimal if the edges of the barriers are parallel to the d-axis. This angle is around 135° for a 4 pole machine [24].

2.4.2 Multi-Barrier Rotor Structure

The theory presented in this paragraph is extensively treated in [6] and has been derived assuming for simplicity that

- the iron is ideal (no saturation and no magnetic potential drop, i.e. $\mu_{FE} \rightarrow \infty$)
- the stator slotting effect is neglected

- the winding and the MMF distribution are sinusoidal

In order to design the motor taking into consideration all of these aspects, FEM simulations are required.

If a d-axis MMF is applied, the rotor structure does not interfere if the magnetic drop is disregarded. Hence it is possible to calculate the d-axis magnetizing inductance as

$$L_{md} = c \frac{1}{p} \int_{-\pi}^{p\pi} \cos^2(\xi) d\xi = c \int_{-\pi}^{\pi} \cos^2(\xi) d\xi = c\pi \quad (2.18)$$

where, c is a constant depending on the geometry and the number of poles. When a q-axis MMF is applied, the rotor structure is polarized, even if the magnetic drop is disregarded as before. In Fig. 2.17, the k-th barrier magnetic potential r_k is shown when a unitary q-axis MMF is applied. r_k is lower than the average MMF on the angular interval relative to the k-th segment because of the air-gap presence.

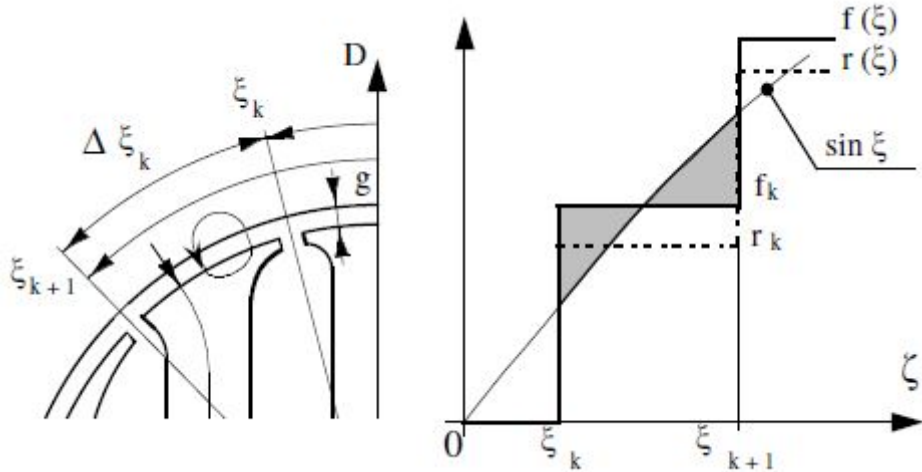


FIGURE 2.17: k-th segment and related pu magnetic potential [6]

As visible in Fig. 2.17, the q-axis flux is composed of two contributions, one circulating in the air-gap and one going through the rotor. As a consequence, the q-axis magnetizing inductance can be calculated as

$$L_{mq} = L_{cq} + L_{fq} \quad (2.19)$$

$$L_{cq} = c \int_{-\pi}^{\pi} \sin(\xi) [\sin(\xi) - f(\xi)] d\xi \quad (2.20)$$

$$L_{fq} = c \int_{-\pi}^{\pi} \sin(\xi) [f(\xi) - r(\xi)] d\xi \quad (2.21)$$

$$f_k = \frac{1}{\Delta\xi_k} \int_{\xi_k}^{\xi_{k+1}} \sin(\xi) d\xi = \frac{\cos(\xi_k) - \cos(\xi_{k+1})}{\xi_{k+1} - \xi_k} \quad (2.22)$$

It is now possible, by computing the integrations for each segment, to find the following relations

$$\frac{L_{cq}}{L_{md}} = 1 - \frac{4}{\pi} \sum_k f_k^2 \Delta\xi_k \quad (2.23)$$

$$\frac{L_{fq}}{L_{md}} = \frac{4}{\pi} \sum_k f_k (f_k - r_k) \Delta\xi_k \quad (2.24)$$

Concerning the q-axis flux, the barrier magnetic potential r_k needs to be calculated from f_k and the geometry of the machine. This calculation can be performed by means of the equivalent magnetic circuit shown in Fig. 2.18.

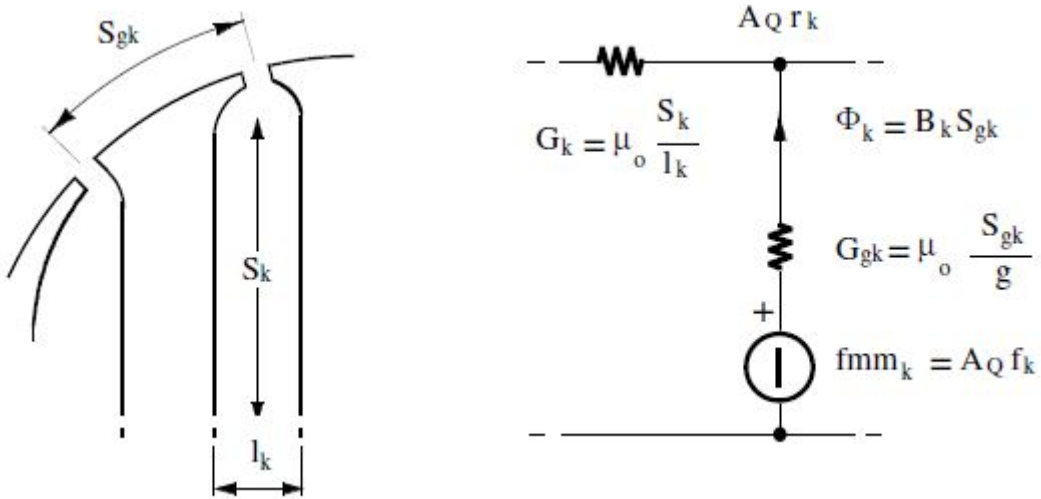


FIGURE 2.18: k-th segment equivalent magnetic circuit [6]

G_k represents the magnetic permeance of the k-th flux barrier and G_{gk} the magnetic permeance of the air-gap relative to the respective segment. Moreover, A_Q is the q-axis MMF peak and all the other symbols are self explanatory. Moreover, it is possible to obtain a pu equivalent circuit, as depicted in Fig. 2.19, in order to get rid of A_Q in the relation between r_k and f_k .

By applying the Kirchhoff's current law (KCL) at the node k in the pu equivalent circuit, it is possible to find the equation

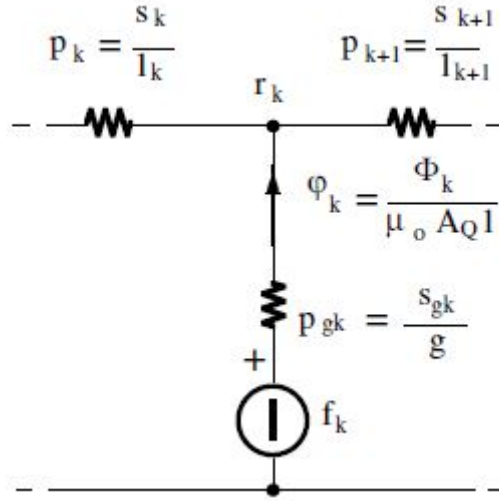


FIGURE 2.19: k-th segment equivalent pu magnetic circuit [6]

$$p_k(r_k - r_{k-1}) + p_{gk}r_k + p_{k+1}(r_k - r_{k+1}) = p_{gk}f_k \quad (2.25)$$

and by repeating this process for each flux barrier, in order to compute r_k for each flux barrier, it is possible to set the following set of equations

$$[P][r_k] = [p_{gk}f_k] \quad (2.26)$$

where, the matrix P depends on p_k and p_{gk} .

Equation 2.24 can be rearranged as

$$\frac{L_{fq}}{L_{md}} = \frac{4}{\pi} \frac{\delta}{p_r} \sum_k f_k \phi_k \quad (2.27)$$

where the air-gap δ and the flux ϕ_k are shown. Moreover, if $r_k \simeq f_k$ it is possible to write

$$\frac{L_{fq}}{L_{md}} \simeq \frac{4}{\pi} \frac{\delta}{p_r} \sum_k p_k \Delta f_k^2 \quad (2.28)$$

It is now possible to state that the circulating q-axis flux drops drastically when the number of layers is increased, as it could be expected by looking at the geometry. On the other hand, the q-axis flux is scarcely influenced by the number of layers, while it is mainly affected by the quantity of magnetic insulation i.e., the previously mentioned

insulation ratio. As a consequence, it is possible to conclude that $\frac{L_{mq}}{L_{md}}$ increases as p is increased i.e., the saliency ratio ξ decreases, and $\frac{L_{cq}}{L_{md}}$ decreases as the number of layers is increased. The number of poles choice is then constrained by anisotropy optimization and iron yoke design. In the literature it is said that if there are no iron yoke design constraints the best choice is often the 4 poles configuration. The leakage inductance (in the slot and in the ribs) dependence on the number of poles is also analysed in [6] by Vagati.

In the slotted stator analysis in [6], also the leakage flux contributions and slot harmonics are considered. It is found that the best strategy to reduce torque ripple is to jointly design the number of stator slots n_s and rotor barriers n_r in order to obtain

$$n_r = n_s \pm 4 \quad (2.29)$$

since $n_r = n_s$ or $n_r = n_s \pm 2$ would lead to a direct stator and rotor harmonics interaction, i.e. torque ripple production. If $n_r \gg n_s$ the rotor magnetic potential matches at least with $n_s \pm 1$ producing torque ripple. Once n_r is chosen, it is possible to perform the permeance design. Different strategies are suggested in [6].

2.4.3 Insulation Distribution in the Rotor Structure

Vagati et al. in [25] express the rule to obtain the best insulation distribution among the layers

$$\frac{W1_k}{W1_h} = \frac{\Delta f_k}{\Delta f_h} \sqrt{\frac{S_k}{S_h}} \quad (2.30)$$

where, k and h are the barrier numbers. Δf_k represents the difference in the average pu q-axis MMF over the k -th barrier and S_k is the barrier length. It is possible to re-adapt eq. 2.30 for barrier permeances

$$\frac{p_h}{p_k} = \frac{\Delta f_k}{\Delta f_h} \sqrt{\frac{S_h}{S_k}} \quad (2.31)$$

since

$$p_k = \frac{S_k}{W1_k} \quad (2.32)$$

In order to realize an homogeneous anisotropic structure, it is possible to design the flux barriers in such a way they have the same permeance p_k (it is not the only possible approach [2]). This assumption, combined with eq. 2.30, gives

$$\frac{W1_k}{W1_h} = \frac{\Delta f_k^2}{\Delta f_h^2} \quad (2.33)$$

Moreover, in order to ensure the same flux density in all the segments, and then maximize the d-axis flux, the flux paths thickness has to follow the following rule

$$\frac{S_k}{S_h} = \frac{fd_k}{fd_h} \quad (2.34)$$

Equations 2.33 and 2.34 summarize the theory developed in [6] to distribute the magnetic insulation in the rotor structure in an optimal way. One more assumption, combined with a suitable d-axis insulation ratio (usually lower than in the q-axis), is needed to completely define the barriers shape and dimensions (refer to barrier shape in Fig. 2.16)

$$\left(\frac{Wk_d}{Wh_d}\right)_{d-axis} = \left(\frac{W1_k}{W1_h}\right)_{q-axis} \quad (2.35)$$

2.4.4 Torque Ripple Minimization

The torque ripple is definitely an important aspect to take care of for SynRM and PMaSynRM motor design. The torque ripple is due by the rotor-stator interaction, hence a joint design has to be performed. As shown in [2], [6], [27], the torque ripple optimization basically depends more on the number of flux barriers in the rotor structure than how they are positioned. In [2], it has been shown that the maximization of the average torque (related to the insulation ratio) and the minimization of the torque ripple are independently possible for SynRM motors. Moreover, the torque ripple and iron losses optimization are not possible to be done at the same time. Thus, a compromise between these two important aspects has to be found.

As explained in [2], it is possible to maintain a constant rotor slot pitch and move, at the same time, all the barriers towards the shaft or the air-gap by moving the imaginary point B shown in Fig.2.20. Its position is identified from the closest rotor slot to the q-axis by moving with the same rotor slot pitch towards the q-axis itself. Angle β describes the angle span between B and the q-axis.

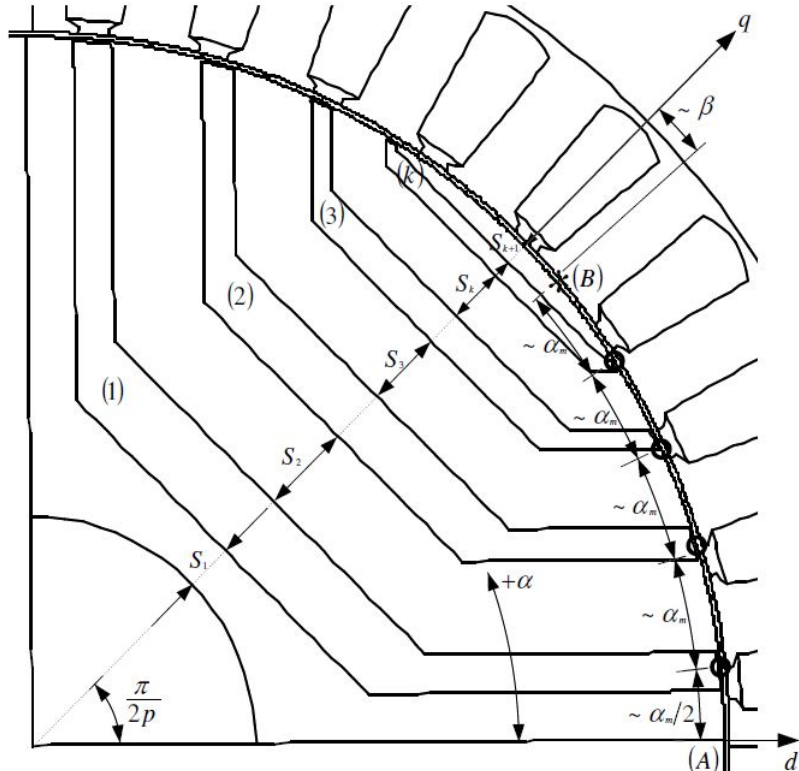


FIGURE 2.20: Multi-barrier geometry with the imaginary point B [23]

The angle β is a design parameter, since it decides the flux barrier position and it can be considered the only parameter to be optimized. If the rotor slot pitch (α_m) is imposed to be constant, it is possible to relate it to β as in the follow equation

$$\alpha_m = \frac{\frac{\pi}{2p} - \beta}{k + \frac{1}{2}} \quad (2.36)$$

where, k is the number of barriers.

2.4.5 Radial and Tangential Ribs

The salient rotor structure needs to be mechanically stable for all the possible speeds reachable by the motor. Thus, in order to sustain the centrifugal forces due to the rotation, radial ribs (usually in the q-axis direction) and tangential ribs (close to the air-gap) are used.

The ribs lower the anisotropic behaviour, and consequently the motor performance, because of their related leakage fluxes (the rib position does not affect the magnetic behaviour [6]). In normal operation condition, the ribs are saturated (it is assumed that they saturate at a constant flux density B_{sat}) and, thus, magnetically isolate the

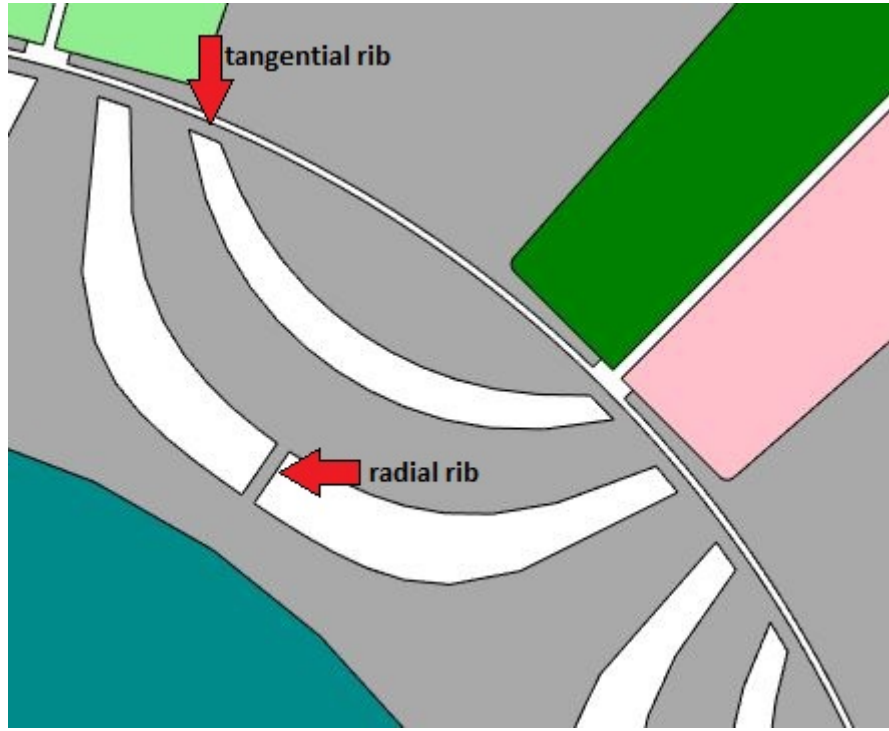


FIGURE 2.21: Radial and tangential ribs

different rotor iron layers. Because of the saturation hypothesis, they can be modelled as flux source in anti-parallel with the PM-flux source [6]. The flux source related to the rib is characterized by

$$\phi_{rib} = B_{sat} t_{rib} L \quad (2.37)$$

where t_{rib} is the rib width. It is important to notice the mentioned rib model does not introduce any non-linearity. The minimal required rib width can be retrieved by mechanical FEM analysis and it basically depends on the speed of the motor, the rotor structure and thermal influence. However, the desired theoretical width cannot be always applied since it may be too low because of production limits.

2.5 Permanent Magnets Optimal Insertion for Natural Compensation

The permanent magnet quantity minimization is of large interest in the PmaSynRM design, because, in many cases, it leads to a significant cost saving. The risk of demagnetization must be taken into consideration, since reducing, for example, the magnet thickness leads to a magnet working point characterized by a lower flux density.

As mentioned before, the design procedure of a PMaSynRM generally starts with the design of the rotor iron structure i.e., the SynRM motor. If a wide CPSR is required by the application, the permanent magnets are designed so that the PM flux linkage λ_{PM} obeys to the following equation

$$I_{RATED} \geq \frac{\lambda_{PM}}{L_q} = I_{CHAR} \quad (2.38)$$

where, I_{CHAR} is the motor characteristic current.

In [28] an analytical formulation of the problem is provided with reference to a single flux barrier. It applies for each of the rotor flux barriers, that are decoupled to each other. It is explicitly stated that the barriers decoupling does not introduce any approximation in the model.

A linearised geometry and its respective equivalent magnetic circuit are displayed in Fig.2.22 [28].

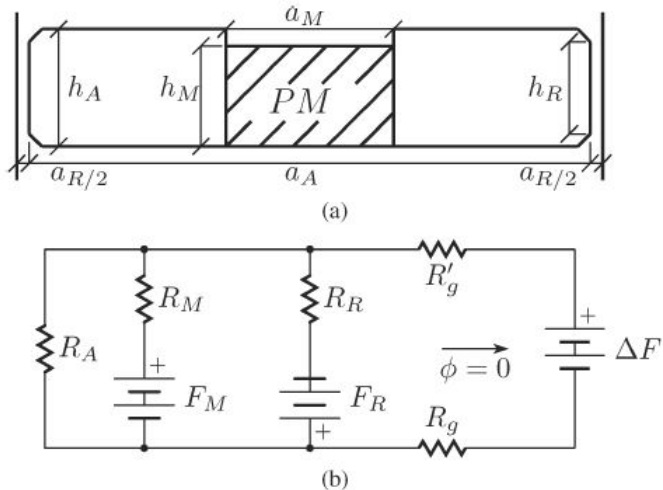


FIGURE 2.22: a)Linearised barrier geometry b)Equivalent magnetic circuit [28]

The equivalent magnetic circuit components

$$R_M = \frac{h_M}{\mu_M \mu_0 a_M l} \quad (2.39)$$

$$R_A = \frac{h_A}{\mu_0 (a_A - a_M) l} \quad (2.40)$$

$$R_R = \frac{h_R}{\mu_R \mu_0 a_R l} \quad (2.41)$$

are, respectively, the PM reluctance, the air path reluctance (on both the sides of the PM) and the ribs reluctance. R_g and R'_g represent the two air-gap sections needed to close the flux lines towards the stator, but they are disregarded in the following calculations. Moreover,

$$F_M = \frac{B_r}{\mu_0} h_M \quad (2.42)$$

and

$$F_R = \frac{B_{sat}}{\mu_0 \mu_R} h_R \quad (2.43)$$

are, respectively, the PM MMF and the MMF relative to the rib model (B_{sat} and μ_R are taken from the saturated region of the considered iron magnetizing curve). ΔF represents the stator MMF related to each layer and it is obtained by averaging the q-axis fundamental stator MMF over the corresponding flux barrier span. The q-axis fundamental stator MMF is given by

$$F_q = \frac{3}{\pi} \frac{N}{p} K_w I_q \quad (2.44)$$

In [28], it is said that the design technique in which the barrier space left free from the magnet thickness is replaced with iron is the most effective since it allows, at the same time, to dimension the magnet thickness to block the q-axis flux and provide the maximum path width for the d-axis flux. A specific property of the design technique proposed by Vagati *et al.* in [28] is to obtain a null flux also in each rotor barrier, as shown in Fig.2.22. In order to obtain such a condition, the PM MMF has to be designed as

$$F_M = R_M \left[\left(\frac{1}{R_A} + \frac{1}{R_M} + \frac{1}{R_R} \right) \Delta F + \frac{F_R}{R_R} \right] \quad (2.45)$$

as can be deduced by the circuit in Fig.2.22. After rearranging the relations given for the time being, it is possible to express the magnet area as

$$S_M = \frac{K_1 \cdot K_3 \cdot y^2}{K_2 \cdot y - 1} \quad (2.46)$$

where,

$$y = \frac{h_M}{h_A} \quad (2.47)$$

$$K_1 = h_A a_A \quad (2.48)$$

$$K_2 = \frac{h_A B_r}{\mu_0 \Delta F} + 1 \quad (2.49)$$

$$K_3 = \mu_R \frac{a_R}{a_A} \frac{h_A}{h_R} \left(1 + \frac{F_R}{\Delta F} \right) + 1 \quad (2.50)$$

Eq. 2.46 defines a family of machines with the same characteristic current but with small rotor geometry deviations. They have also almost coincident torque and power factor values. In [28] a 4-layer example was analysed and the PM area variation with the PM thickness for each layer is shown in Fig.2.23.

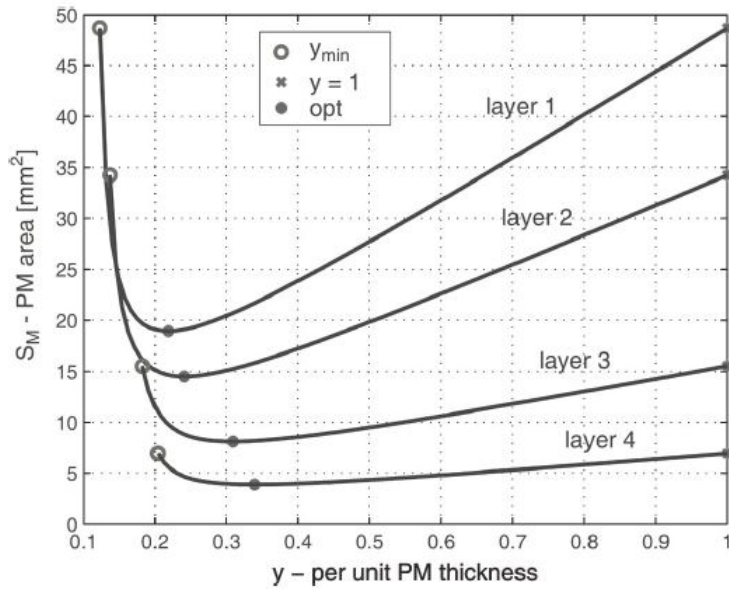


FIGURE 2.23: PM area dependence on the PM thickness (ribs are neglected) [28]

As visible from the graph, for each barrier, there is a value of y that minimizes the PM area. It is always between $y = 1$ and y_{min} , which corresponds to the maximum width of the PM. The PM area minimum is found by imposing its partial derivative respect to y to zero

$$\frac{\partial S_M}{\partial y} = 0 \quad (2.51)$$

The retrieved optimal PM thickness and the relative optimal PM area are

$$y_{opt} = \frac{2}{K_2} \quad (2.52)$$

$$S_{Mopt} = 4 \frac{K_1 K_3}{K_2^2} \quad (2.53)$$

It is also interesting to determine a minimum PM thickness in order to avoid demagnetization due to a working point with a too low flux density. Imposing B_{wc} as the minimum allowed flux density in the PM, with ΔF_{OL} defined as ΔF but due to the overload current, the minimum PM thickness is given by

$$y_{demag} = \frac{\mu_0 \Delta F_{OL}}{B_{wc} h_A} \quad (2.54)$$

which is, as expected, higher for overload currents. As a consequence, the optimal magnet thickness is not always feasible because of the risk of demagnetization.

2.6 Flux-Weakening Operation

When an electric drive is operated, it is convenient to use the rated current and the rated flux, in order to generate the rated torque, at low speed. The induced voltage is proportional to the flux and the speed. Hence, when the maximum available voltage for the drive is reached (also called rated voltage), it is said that the machine operates at rated speed (or base speed). For the available voltage, in order to increase the speed further, it is necessary to decrease the flux. The purpose is to maintain the induced voltage at the rated value, even if the speed exceeds the base value. As a result, in the region where the power is kept constant, the torque is inversely proportional to the speed, as shown in Fig. 2.24 [13].

For example, in SMPM motors, since the excitation flux is fixed, the only way to regulate it, is to feed the stator winding with a demagnetizing current in order to create a field that opposes and compensates the flux from the magnets. This current is a negative d-current, since the magnet flux is pointed in the positive direction of the d-axis. The PMaSynRM current and flux trajectories for maximum torque control are depicted in Fig. 2.25, taken from [14]. The operation points below the rated speed are marked with MTPA (Maximum Torque per Ampere). Since the main flux of the machine is not in the same axis of the permanent magnets, the first defluxing phase consists in reducing

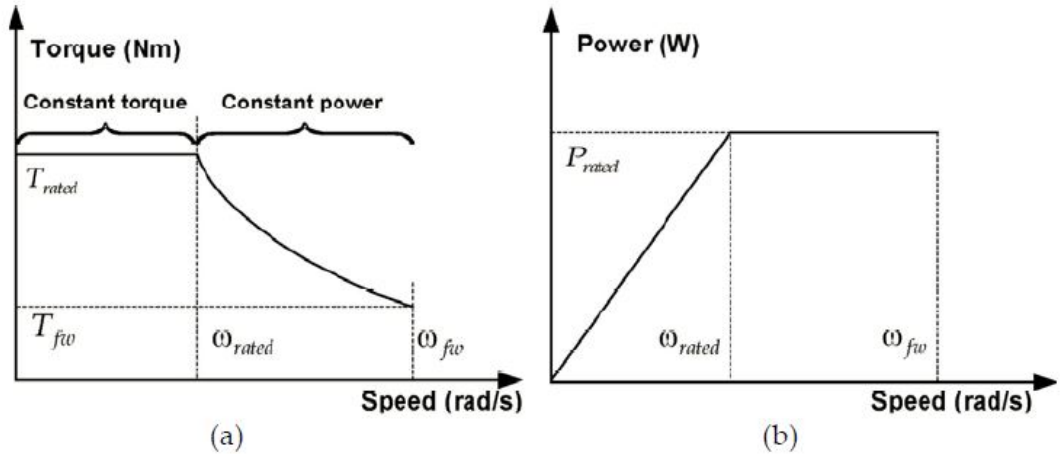


FIGURE 2.24: Ideal field weakening characteristics. a) Torque b) Power [13]

the d-current (from point A to B, along the maximum current circle) until the motor reaches the MTPV (Maximum Torque per Voltage) region. Moreover, if the motor is perfectly compensated, the MTPV operation is theoretically reached at infinite speed. This argument is fully described in [14].

Neglecting the resistive voltage drop, the PMaSynRM voltage limit V_{RAT} is defined as

$$V_{RAT}^2 \geq \omega^2 |(L_d I_d)^2 + (L_q I_q + \lambda_{PM})^2| \quad (2.55)$$

It is possible to define the CPSR (Constant Power Speed Range) as

$$CPSR = \omega_{CPSR} / \omega_b \quad (2.56)$$

where, ω_{CPSR} is the maximum speed the drive can reach with the rated power. For the PMaSynRM the torque decrease, in CPSR, is partially compensated by the power factor increase. Hence, the torque decreases less than inversely proportional.

In general, the two design parameters that influence the flux weakening performance of a synchronous motor are the saliency ratio

$$\xi = \frac{L_d}{L_q} \quad (2.57)$$

and the normalized magnet flux linkage

$$\psi_{mn} = \frac{\psi_m \omega_b}{V_b} \quad (2.58)$$

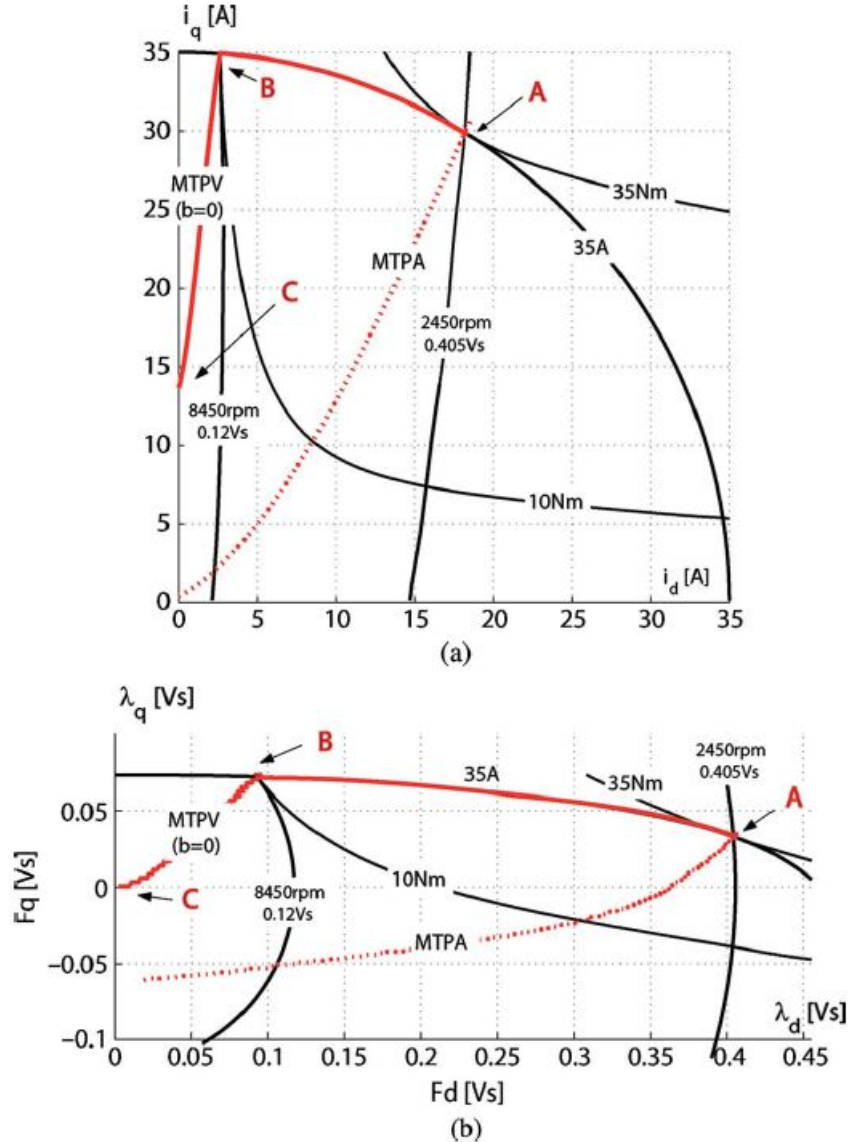


FIGURE 2.25: a) Current and b) flux trajectories for maximum torque control in PMaSynchRM [14]

All the possible ξ/ψ_{mn} combinations performance are summarized in Fig. 2.26, taken from [15], where an opposite dq convention is used with respect to this thesis.

For a given saliency ration, the CPSR improves with an increasing amount of magnet flux until a certain point, but it worsens beyond that. In Fig. 2.26, it is possible to notice an optimal flux weakening design curve as evidenced in Fig. 2.27, taken from [7].

2.7 Iron Magnetization Characteristic

Iron non-idealities are to be taken into account for refining the motor design and they can be simulated by means of FEM analysis. In reality, not only the iron has a finite

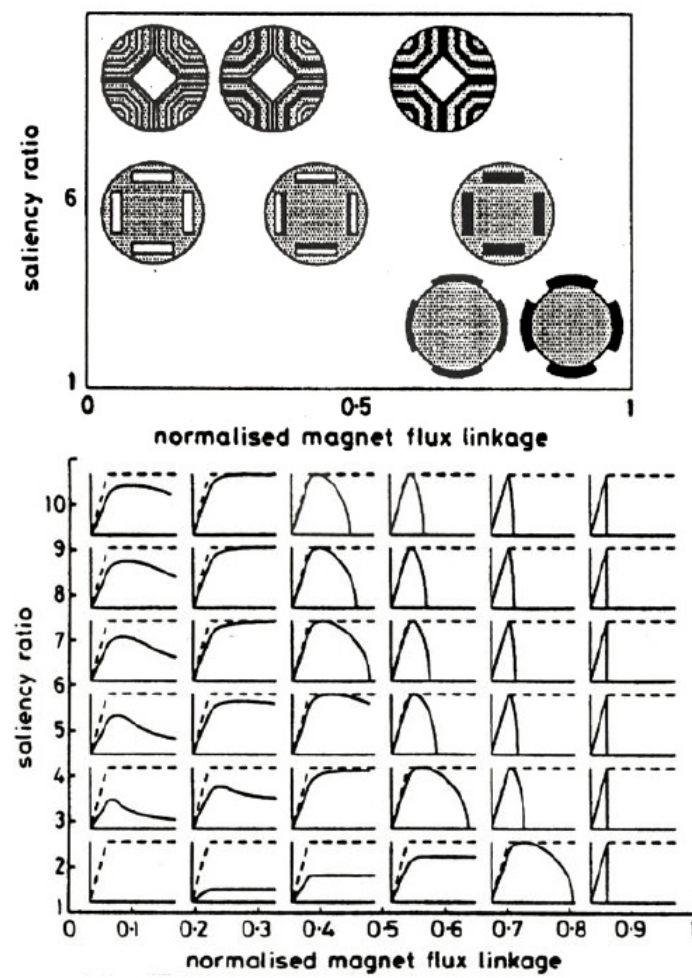


FIGURE 2.26: Parameters plane with motor topologies and normalized power characteristics [15]

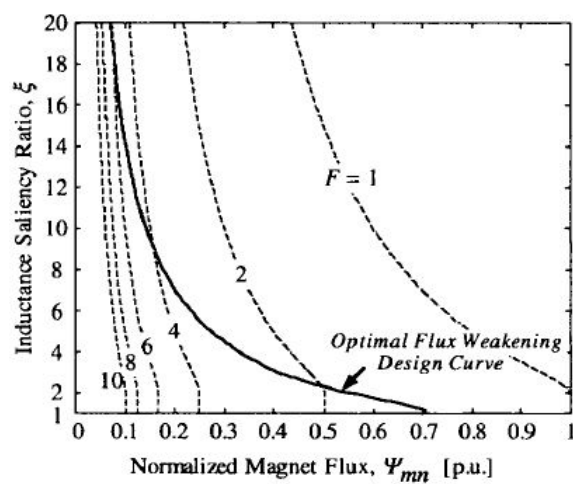


FIGURE 2.27: Permanent magnet machines design space [7]

magnetic permeability, but also it is not constant. In other words, the iron has a non-linear behaviour. In synchronous machines, it is possible to distinguish two magnetic behaviours: one in the d-axis and other in the q-axis. In the most complete model, both of the fluxes (hence also the inductances) in these two axis, are influenced by both the currents I_d and I_q . The influence of a current to a flux on a different axis is a phenomenon called *Cross Saturation*. It is then possible to write

$$\lambda_d = \lambda_d(I_d, I_q) \quad (2.59)$$

$$\lambda_q = \lambda_q(I_d, I_q) \quad (2.60)$$

A measured magnetic characteristic for a four poles PMaSynRM is shown in Fig. 2.28 [6]

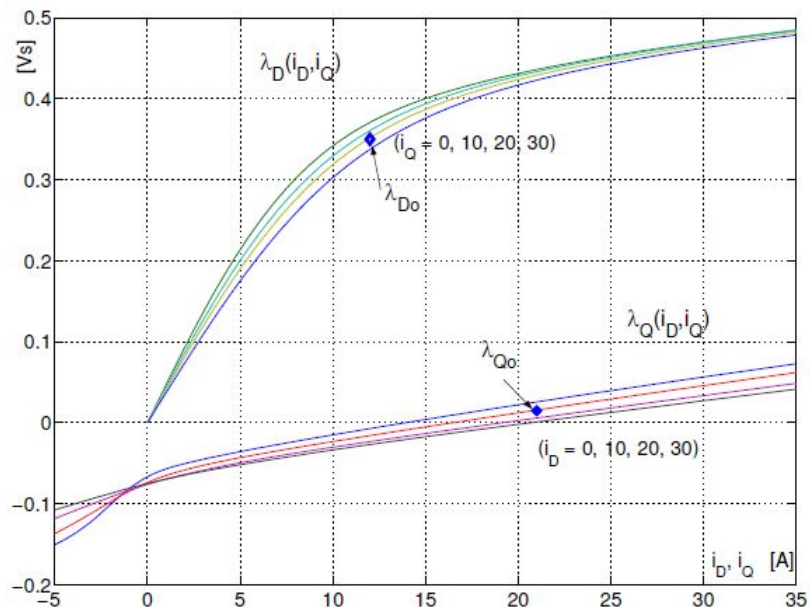


FIGURE 2.28: Measure magnetic characteristic for a four poles PMaSynRM [6]

The main cross saturation negative effect consists in lowering the magnetizing flux i.e., in the d-axis, for the same d-axis current. As a consequence, the per-ampere torque capability and, more greatly, the power factor decrease (the latter is anyway improved in the case of a PM assisted motor). The MTPA locus in the (I_d, I_q) plane is also distorted because of the cross saturation. An example for a four poles PMaSynRM is depicted in Fig.2.29 [6], where a major need of d-axis current is evident when the cross saturation occurs.

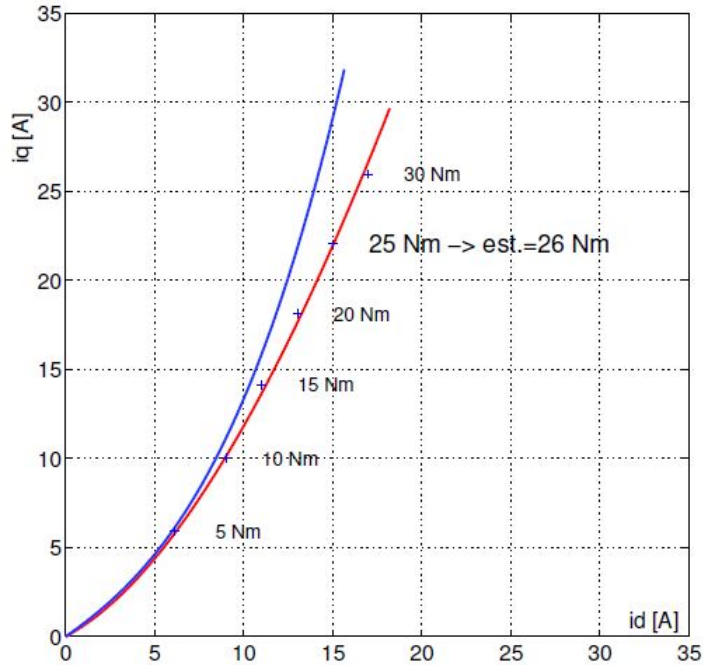


FIGURE 2.29: MTPA loci for a four poles PMaSynRM, with(red) and without (blue) cross saturation

2.8 Conclusions

This chapter presents the wide variety of aspects to be taken into consideration when a PMaSynRM motor with CW has to be designed or analysed. It also gives the idea of the topic complexity and the effort a designer has to make in order to properly match all the possible technical solutions at different levels: winding, iron structure, PMs, etc.

In chapter 3 the initial design procedure for such a motor is shown. More precisely, the winding layout is fixed and an analytical initial dimensioning is carried on.

Chapter 3

Initial Motor Design

The initial design procedures and choices, based on analytical considerations, are presented in this chapter. The winding layout and the geometry of the motor are defined and a first motor design, named "SynRM 1", is simulated. The permanent magnet insertion is treated in the coming chapters.

3.1 Double layer concentrated Winding Design

At this stage, it was decided to design a double-layer winding and a pole/slot combination was fixed to 10/12 (i.e., 10 poles and 12 slots).

This combination has been widely tested and presents the following features [1]:

- high fundamental winding factor ($k_{wf} = 0.933$)
- acceptable cogging torque, $LCM(Q, p) = 60$ (Least Common Multiple)
- unbalanced magnetic pull is not present, $GCD(Q, p) = 2$ (Great Common Divisor)

This winding is characterized by a number of slot per pole per phase q given by Eq.3.1

$$q = Q/(mp) = 2/5 \quad (3.1)$$

where, Q is the number of stator slots, m the number of phases and p the number of poles. The winding layout is hereafter designed by mean of the 'Star of Slots' method, described in the previous chapter. The feasibility check gives a positive result since

$$Q/(m \text{GCD}(Q, p/2)) = 4 \quad (3.2)$$

is an integer value.

In this case, the star of slot is composed by $Q/\text{GCD}(Q, p/2) = 12$ spokes, shifted in counter-clockwise direction by an angle of $\pi p/Q = (5/6)\pi$. The resulting star of slots is depicted in Fig.3.1 .

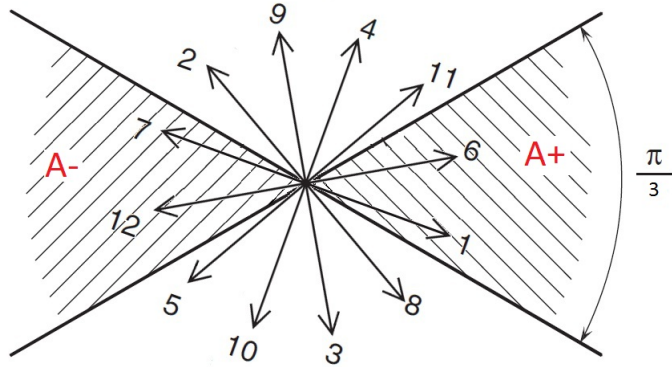


FIGURE 3.1: Star of slots for a double-layer concentrated winding with $Q = 12$ and $p = 10$

The phase and the polarity are assigned to each spoke, which corresponds to a slot, as described in the previous chapter. It is now possible to fill the slot as depicted in Fig.3.2.

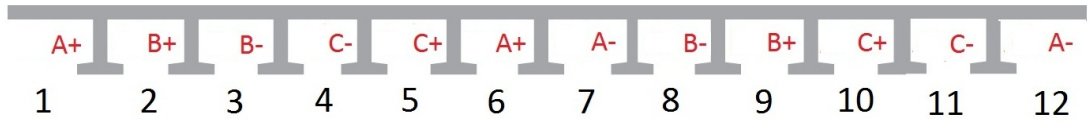


FIGURE 3.2: First winding layer positioning

It is now straightforward to complete the winding layout as shown in Fig.3.3 .

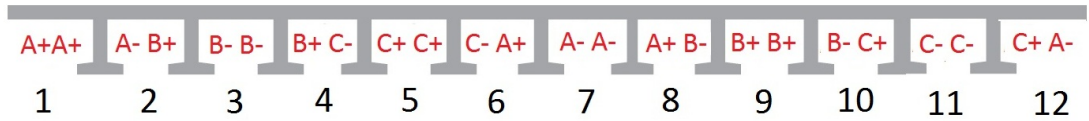


FIGURE 3.3: Winding layout for a double-layer concentrated winding with $Q = 12$ and $p = 10$

The above mentioned winding layout produces a MMF wave along the air-gap characterized by the space-harmonics spectrum shown in Fig.3.4.

For a 10-pole machine, the MMF working space-harmonic, i.e. the one that interacts with the rotor field in order to produce the mean value of torque, is the 5th. All the other space-harmonics provide undesirable effects, as described in the previous chapter.

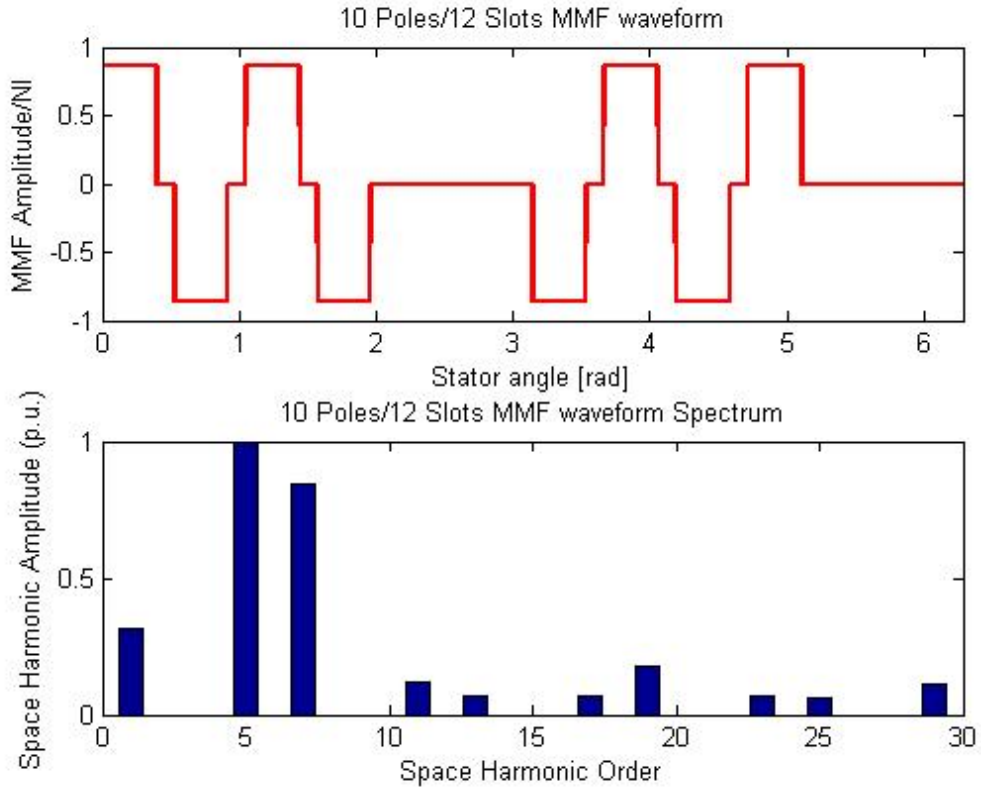


FIGURE 3.4: MMF distribution along the air-gap and its space harmonic spectrum for the winding depicted in Fig.3.3

For this reason, it is a design goal to minimize their effect. A particular attention has to be paid for the 1st order harmonic as it produces a two-pole MMF along the air-gap and its presence is particularly undesired. It causes saturation, rotates asynchronously with respect to the rotor and penetrates very deeply into the rotor iron. As mentioned in [26], it is possible to improve the harmonic spectrum, and even cancel out the 1st harmonic shown in Fig.3.4, by using a non-conventional winding solution i.e. 4-layer concentrated winding (this solution allows to have different number of conductors in the same coil [26]). It is important to mention that the so-called *Slot harmonics* are characterized by the harmonic orders given by

$$h_s = kQ \pm p \quad (3.3)$$

$$k = 1, 2, 3, \dots \quad (3.4)$$

where, Q is the number of slots and p is the number of pole pairs. However, even with a 4-layer concentrated winding, it is not possible to reduce this class of harmonics. The main

harmonic is reduced because they present the same winding factor. As a consequence, slot harmonics produce a torque ripple that can be reduced only by optimizing the rotor geometry.

3.2 Analytical dimensioning of the motor

The physical size of electrical machines is mainly established on the basis of torque capability requirements. The secondary factors influencing the machine sizing are the motor speed rating (mechanical stress has to be controlled), the maximum number of poles (which influences the iron losses) and the minimum rotor critical speed [20]. The desired rating parameters of the machine to be designed in this work are:

- Output power $P = 15 \text{ kW}$
- Base speed $\omega_b = 1500 \text{ rpm}$

thus, the nominal torque to be achieved has to be

$$T = P/\omega_b \approx 95.5 \text{ Nm} \quad (3.5)$$

3.2.1 Dimensioning of rotor and stator parameters

The theory described in this paragraph is extensively treated by Soong in [20]. For electrical machines in general, the Shear Stress [kPa], which expresses the force applied on the conductors, is defined by

$$\sigma = BA \quad (3.6)$$

where B is the *Magnetic Loading* (or flux density) and A is the *Electric Loading* (or linear current density). These two parameters respectively represent the level of the iron and copper exploitation of the machine. The magnetic loading is typically limited by the saturation limit of the iron, while the electric loading is basically limited by the maximum possible current density, directly linked to the thermal capability. Moreover, the shear stress and the torque for a radial flux machine are related by the following equation

$$T = 2V_r\sigma \quad (3.7)$$

$$V_r = (\pi/4)D^2L \quad (3.8)$$

where, V_r is the rotor volume, D the rotor diameter and L the rotor length [20].

Experience-based values of D/L are typically between 0.5 and 2 and the typical values for σ are shown in Table 3.1.

TABLE 3.1: Typical shear stress value for electrical machines [21]

Application	Shear Stress [kPa]
Industrial motors < 1kW	0.7 to 2
Industrial motors > 1kW	4 to 15
High performance industrial servos	10 to 20
Aerospace machines	20 to 35
Very large liquid-cooled machines	70 to 100

It is important to say that, if the stator dimensions are varied in proportion with the rotor dimensions, a larger rotor diameter leads to deeper slots, hence to a higher possible electric loading. Thus, the output torque proportionality to the outer stator diameter (D_s) is approximately given by [22]

$$T \propto D_s^{2.5}L \quad (3.9)$$

The following values have been considered as the starting parameters for the initial design:

- Shear stress, $\sigma = 10$ kPa
- Rotor dimensions, ratio $D/L = 0.8$
- Air-gap length, $\delta = 0.5$ mm
- Air-gap flux density, $B = 0.8$ T
- Maximum stator yoke flux density, $B_y = 1.4$ T

From equations 3.7 and 3.8, it is now possible to extract the rotor dimensions:

$$D = 0.1694m \quad (3.10)$$

$$L = D/0.8 = 0.2118m \quad (3.11)$$

The next step consists of dimensioning the stator slot height. In [20], it is stated that the torque optimum is reached when the ratio between the rotor diameter and the stator slot diameter is around 0.7 (slightly different values are obtained if the slots or the teeth are designed with parallel sides). Hence, it is straightforward to calculate the optimal stator slot diameter and the slot height

$$D_{sl} = (D + \delta)/0.7 = 0.2428m \quad (3.12)$$

$$h_{sl} = \frac{D_{sl} - (D + \delta)}{2} = 0.0364m \quad (3.13)$$

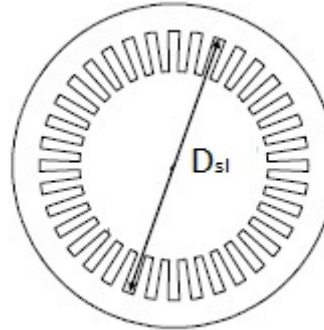


FIGURE 3.5: Stator slot diameter D_{sl}

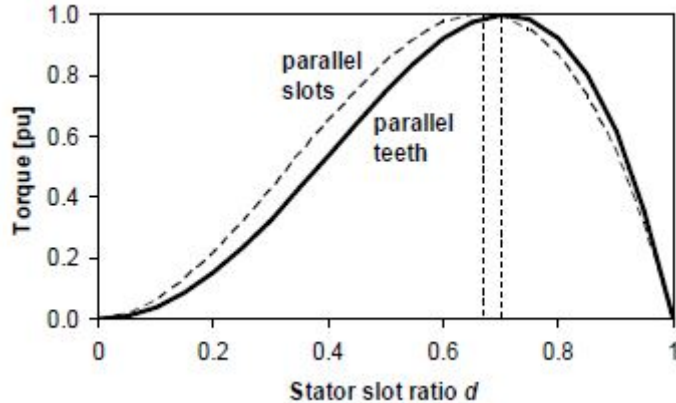


FIGURE 3.6: Output torque versus the ratio of the slot inner and outer diameters [20]

The stator yoke thickness (which is as large as the iron path in the rotor) can be calculated as described in [20]

$$t_{ys} = \frac{B}{B_y} \frac{\pi D}{4p} = 0.0152m \quad (3.14)$$

Finally, it is possible to compute the outer stator diameter as

$$D_{out} = D + 2(\delta + h_{sl} + t_{ys}) = 0.2737m \quad (3.15)$$

The value of t_{ys} represents the flux path thickness both in the stator and in the rotor. Once the q-axis insulation ratio (k_{wq}) is defined, it is possible to calculate the rotor yoke thickness(t_{yr}) and the rotor core inner diameter (D_I). As a starting value, a q-axis insulation ratio of 0.7 and a two flux-barrier geometry are selected. Note that the torque and torque ripple sensitivity for these design parameters should be carefully studied, as explained in [2]. Thus

$$k_{wq} = 0.7 \quad (3.16)$$

$$t_{yr} = (1 + k_{wq})t_{ys} = 0.0259m \quad (3.17)$$

$$D_I = D - 2t_{yr} = 0.1177m \quad (3.18)$$

At this stage, it has been decided to equally divide the stator in space available for slots (copper) and teeth (iron). The average slot and tooth width is then calculated as

$$(w_{sl})_{average} = (w_{tooth})_{average} = \frac{\pi(D + \delta)}{2Q} = 0.0222m \quad (3.19)$$

This design decision is the object of optimization later on, in order to find the optimal compromise between copper and iron losses. In other words, the way the stator space is divided in copper and iron influences the possible current and magnetic loadings of the motor.

3.3 SynRM 1 Design

The geometry of SynRM 1 is shown in Fig. 3.7, where the different winding phases are indicated with different colors. This motor design has been simulated by means of FEA at its nominal working point. The obtained flux density distribution and flux lines are shown in Fig. 3.8 and all the relevant output parameters from the simulation are summarized in Table 3.2.

Several output parameters from the FEM simulation are not the same as estimated from the analytical calculations (e.g. air-gap and stator yoke flux densities). This is due

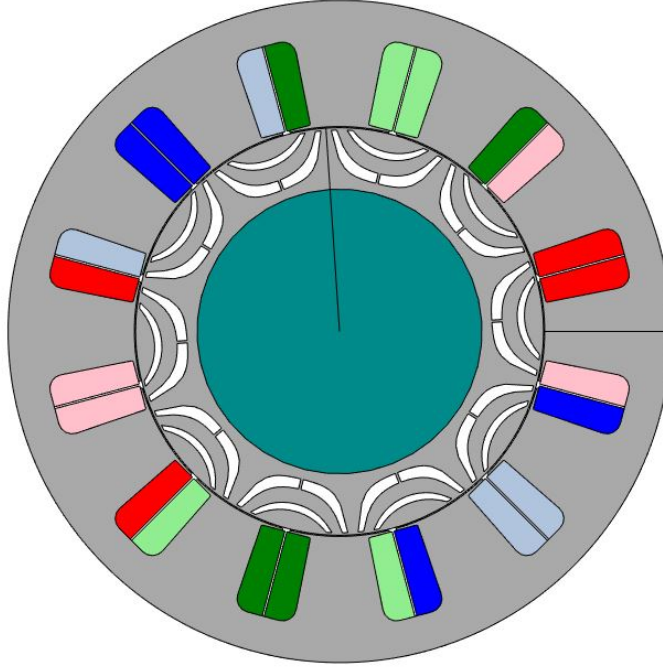


FIGURE 3.7: SynRM 1 geometry

TABLE 3.2: SynRM 1 FEM simulation output parameters

Output Power [kW]	14.966	Input Power [kW]	17.584
Stator Voltage [V]	380	Stator connection	Star
Stator Current [I]	89.21	Frequency [Hz]	125
Power Factor	0.3	Efficiency [%]	85.3
Av. Torque [Nm]	95.47	Peak-to-peak Torque Ripple [%]	19.9
Speed [rpm]	1500	Iron Stator Losses [W]	1237
Iron Rotor Losses [W]	688	Copper Stator Losses [W]	575
Resistive Rotor Losses [W]	47	Friction Losses [W]	41
Total Losses [W]	2547	Stator Current Density [A/mm^2]	4.09
Air-gap flux Density [T]	0.7	Max St. Yoke Flux Density [T]	1.7
Max St. Tooth Flux Density [T]	1.67	Amb. Temperature [°C]	25
Iron Weight [Kg]	49,97	Copper Weight [Kg]	14.05
Total Weight [Kg]	64.02		

to the fact that in the analytical computation the iron non-idealities (finite magnetic permeability and saturation) and slotting effect are not taken into consideration.

It is interesting to observe the air-gap flux density spectrum computed in the simulation in Fig.3.9. The differences in the spectra depicted in Fig.3.4 and 3.9 are due to the magnetic permeance variation along the air-gap. As a result, a 3rd order harmonic created in the air-gap flux density is visible in the FEM simulations in Fig. 3.9.

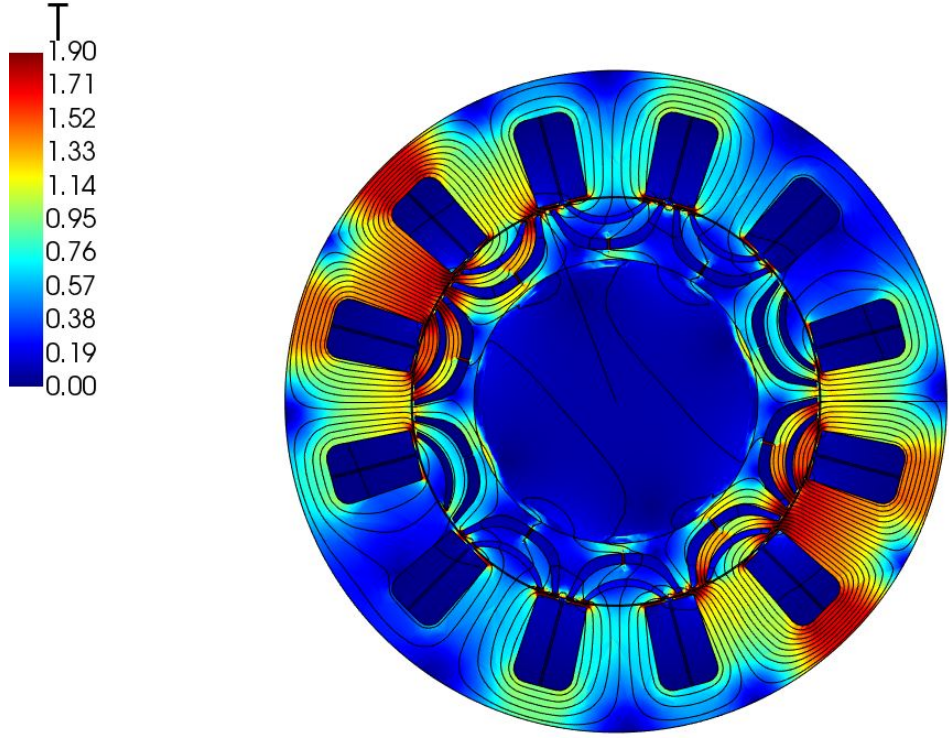


FIGURE 3.8: SynRM 1 flux density and flux lines at nominal load

3.4 Comparison with distributed winding motor

It is now interesting to compare SynRM 1 to the corresponding distributed winding motor. This corresponding motor is obtained by changing only the stator with a distributed winding (it is decided to choose $q = 2$) and then shape the stator geometry in order to have approximately the same current and stator flux density (including an outer diameter reduction of 13.7 mm). The obtained design is named "SynRM 1D" and it is presented as SynRM 1D, in Fig. 3.10, 3.11 and Table 3.3.

TABLE 3.3: SynRM 1D FEM simulation output parameters

Output Power [kW]	14.982	Input Power [kW]	17.530
Stator Voltage [V]	380	Stator connection	Star
Stator Current [I]	85.55	Frequency [Hz]	125
Power Factor	0.31	Efficiency [%]	85.5
Av. Torque [Nm]	95.38	Peak-to-peak Torque Ripple [%]	15.2
Speed [rpm]	1500	Iron Stator Losses [W]	1323
Iron Rotor Losses [W]	375	Copper Stator Losses [W]	809
Resistive Rotor Losses [W]	0.01	Friction Losses [W]	41
Total Losses [W]	2506	Stator Current Density [A/mm^2]	6.41
Air-gap flux Density [T]	1.16	Max St. Yoke Flux Density [T]	1.61
Max St. Tooth Flux Density [T]	1.61	Amb. Temperature [°C]	25
Iron Weight [Kg]	44.9	Copper Weight [Kg]	8.18
Total Weight [Kg]	53.08		

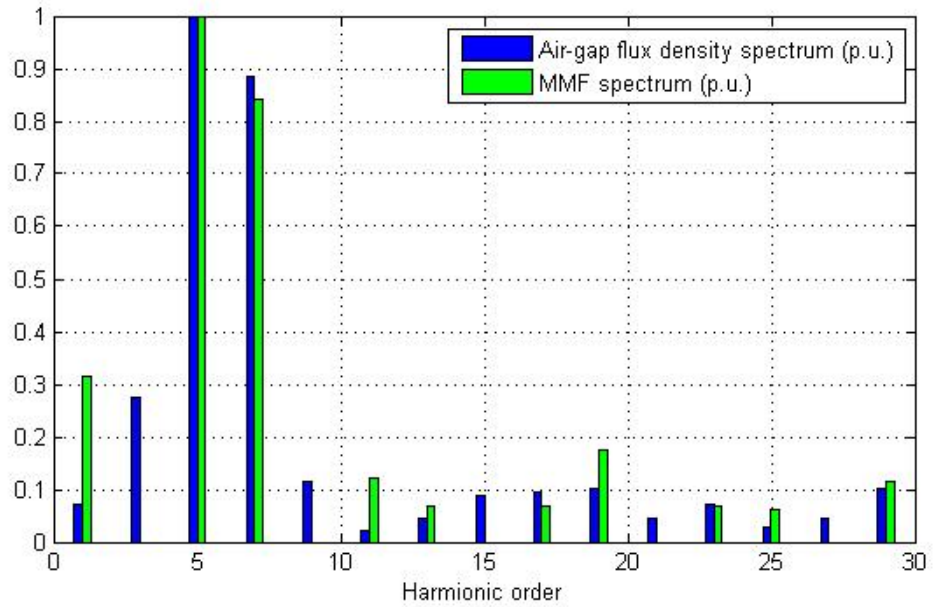


FIGURE 3.9: SynRM 1 Air-gap flux density and MMF spectra in p.u. with reference to the fundamental harmonics

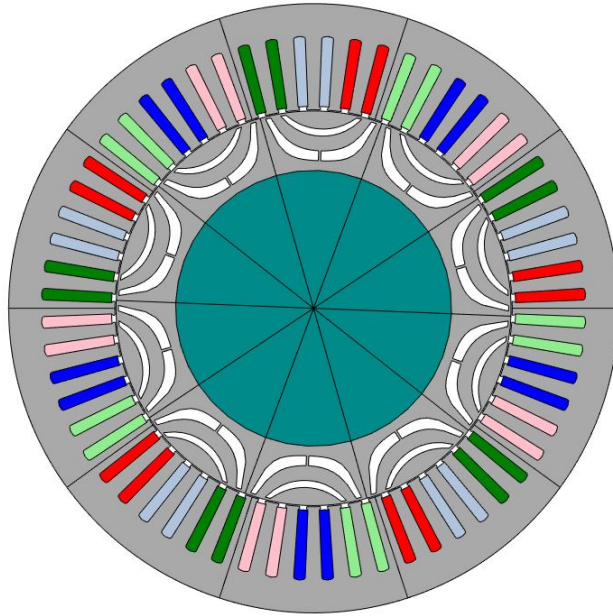


FIGURE 3.10: SynRM 1D geometry

In these motor designs, iron and copper losses differ mainly due to slightly different electric and magnetic loading. An exception is the rotor iron losses which are much higher in the concentrated winding motor, because they are greatly influenced by the air-gap flux density space harmonics (created by asynchronous rotating field components).

It is possible to observe that the efficiency, power factor and torque ripple are comparable for the two machines under consideration. The distributed winding motor presents

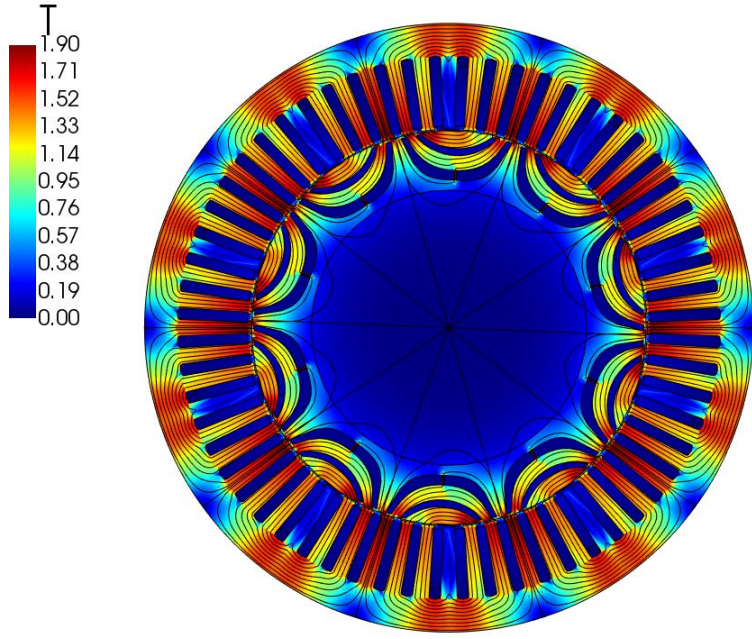


FIGURE 3.11: SynRM 1D flux density and flux lines at nominal load

slightly better values, but it is in comparison between two initial designs, hence it is not possible to say at this point which motor performs better. Moreover, it is not possible to conclude yet what happens if the rated power or speed of the motor is changed. This result expresses the significance of investigating the concentrated winding solution for this type of motor.

3.5 Conclusions

In this part of the thesis, after the winding layout design and an initial dimensioning, the obtained first motor design (SynRM 1) has been compared to a DW design (SynRM 1D) and the choice to pursue for a CW has been motivated.

In the next chapter, the initial design is refined and optimized by means of FEM sensitivity analysis of several key design parameters.

Chapter 4

SynRM Design Optimization and Refinement

In this chapter the motor geometry named SynRM 1 is used as initial design in an optimization procedure in order to maximize the motor performance. This chapter is focused on the iron structure optimization, while the permanent magnet optimization is considered in the coming chapter.

4.1 Optimization of stator winding number of turns per slot

In SynRM 1, the number of effective conductors per slot was fixed to 21. The number of conductors might differ because they can be grouped in parallel. This value has been varied from 15 to 30 with the purpose of maximizing efficiency and power factor.

The optimal number of effective conductors per slot is 24 both for the efficiency and power factor, as shown in Fig.4.1. The efficiency and power factor values in Fig.4.1 are slightly overestimated because the simulations have been run with the magneto-static method. However, they still give important information about the optimized parameter trends. When the motor was simulated in time-stepping mode it was found that, if the number of turns is set to 24, the motor is not able to reach the desired power and, hence, the number of turns has been set to 23. The motor with the optimized number of turns is named SynRM 2 (it has exactly the same geometry of SynRM 1). A time stepping simulation is then run for SynRM 2 and the retrieved efficiency and power factor are 85.76 % and 0.325 respectively.

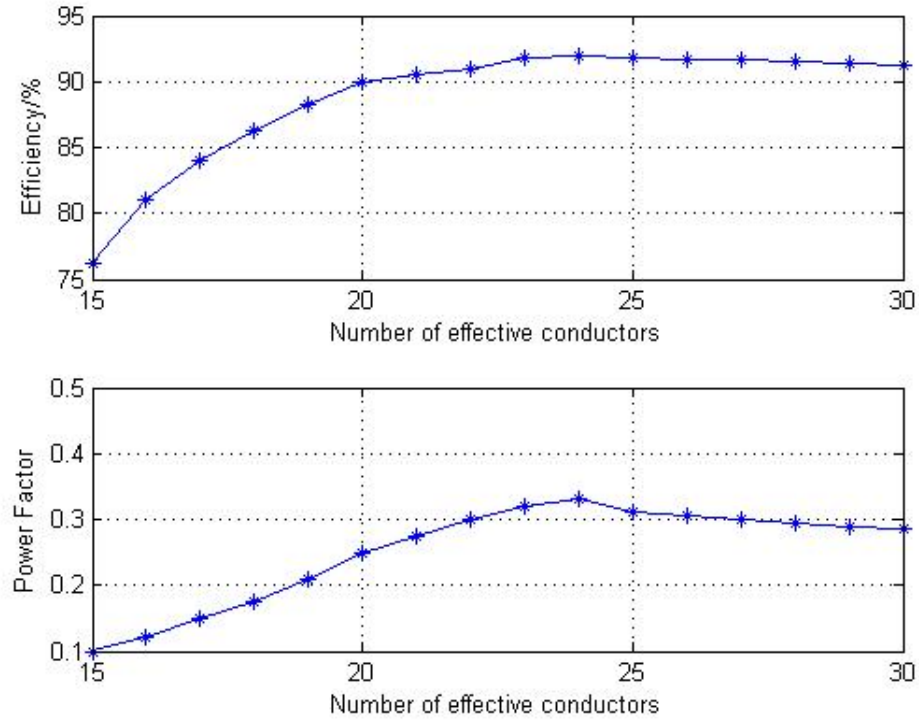


FIGURE 4.1: Efficiency and power factor variation with the effective number of conductors per slot in SynRM 1

4.2 Electric and magnetic load optimization

In the early design, it was decided to equally divide the stator available space for slots and tooth. This choice resulted in the electric and magnetic loading data shown in Table 4.1 for SynRM 2.

TABLE 4.1: SyRM 2 performance

Stator Current Density [A/mm^2]	4.19
Air-gap flux Density [T]	0.649
Max St. Yoke Flux Density [T]	1.601
Max St. Tooth Flux Density [T]	1.629
Power Factor	0.325
Efficiency [%]	85.76

The stator iron is extremely exploited, even over the saturation knee, while the stator current density could be increased without any thermal problems. This consideration leads to a smaller slot area, in order to let the flux flow in a wider cross-section area, e.g. obtaining a lower flux density. However, the convenience of reducing the slot area is also influenced on the percentage of the joule losses with respect to the total losses.

An optimization process is performed in order to find the best combination between the following parameters

- the slot height h_{sl} (36.46 mm in SynRM 2)
- the slot average width w_{sl} (23 mm in SynRM 2), average value between the width closer to the air-gap and the width closer to the yoke.

The parametric study results are presented in Fig.4.2.

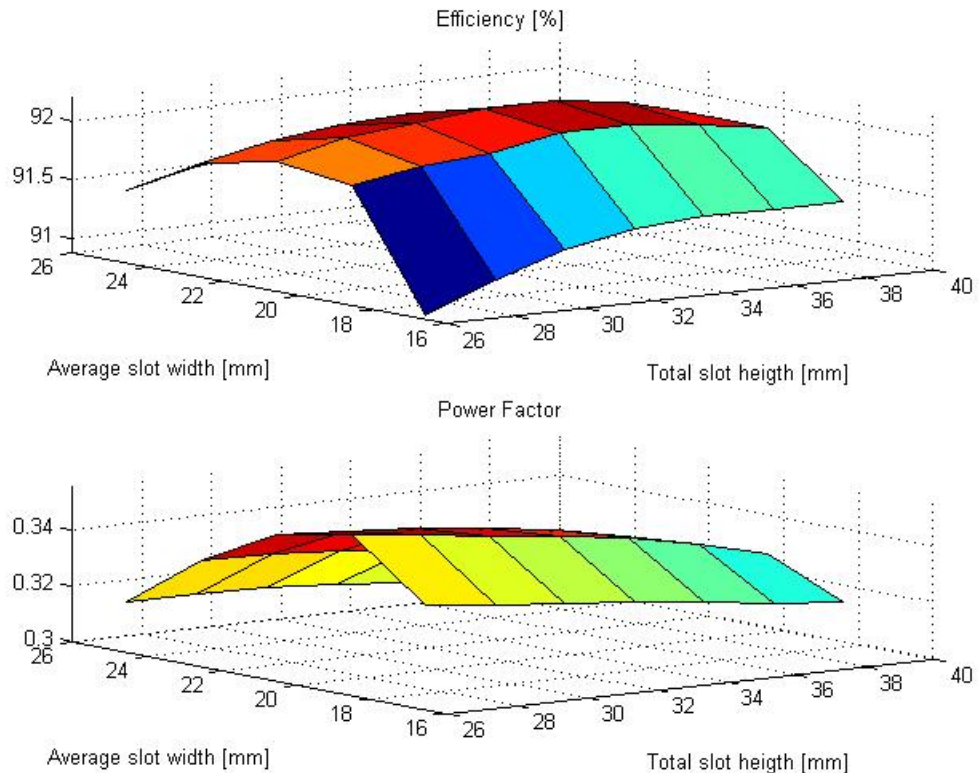


FIGURE 4.2: Efficiency and power factor variation with the stator slot dimensions

In the studied parameter variation, maximum efficiency is targetted in choosing the parameters. However, since the simulations have been performed in magneto-static mode, the results should be considered with care. It is then possible to conclude that the each parameter combination with $30.46 < h_{sl} < 34.46$ are suitable design parameters. The chosen combination is $(h_{sl}, w_{sl}) = (34.46\text{mm}, 23\text{mm})$, with 92.01 % of efficiency and 0.33 power factor. The optimized set of parameters (h_{sl}, w_{sl}) characterizes SynRM 3 design to differentiate it from SynRM 2. It is important to notice that the number of turns optimization balances the electric and the magnetic load as well. In fact, the efficiency surface graph around the SynRM 2 slot width and height is very flat. A good strategy, thus, could be to optimize the number of turns (with a stator geometry in which

slots and tooth have the same width) and then optimize the slot dimension in order to get to a more refined design, since the number of turns is a discrete parameter. As it was in the previous paragraph, the optimization has been performed in magneto-static mode in order to make it less time consuming. Hence, SynRM 3 has been simulated in time-stepping mode and the obtained results are summarized in Table 4.2.

TABLE 4.2: SyRm 3 performance (time-stepping FEM)

Stator Current Density [A/mm^2]	4.44
Air-gap flux Density [T]	0.644
Max St. Yoke Flux Density [T]	1.549
Max St. Tooth Flux Density [T]	1.641
Power Factor	0.3304
Efficiency [%]	85.76

The optimization process led to a slot area shrinkage and an appreciable power factor improvement.

As it can be seen in the vector diagram in Fig. 2.14, the permanent magnet insertion modifies the total flux amplitude. This fact leads to a slightly different magnetic loading of the motor. As a consequence, in theory, this optimization should be performed again after the permanent magnet insertion.

4.3 Average reluctance torque optimization

The considered rotor structure is geometrically complex, hence it is of great importance to recognize the most important parameters to optimize (while the stator is kept the same). As extensively described in [2], it is convenient to introduce a generalized geometry, as shown in Fig. 2.20. In this way, it is possible to perform the optimization process only for a few macroscopic parameters instead of for all the microscopic geometric parameters. The main macroscopic parameter influencing the average torque of the motor is the insulation ratio k_{wq} [2]. Thus, SynRM 3 has been simulated for insulation ratios from 0.7 (the initial value) to 1 (for lower values than 0.7 the motor was not able to deliver the desired torque). The optimization is oriented towards the highest efficiency and power factor. Higher average reluctance torque capability results in a higher efficiency since the motor has to be less exploited in terms of electric and magnetic loading. Lower current or flux values result in lower losses, hence, for a fixed delivered power, the efficiency is higher. This time, because of the lower number of possible combinations to be simulated, the simulations have been performed directly in time-stepping mode. The results are displayed in Fig. 4.3.

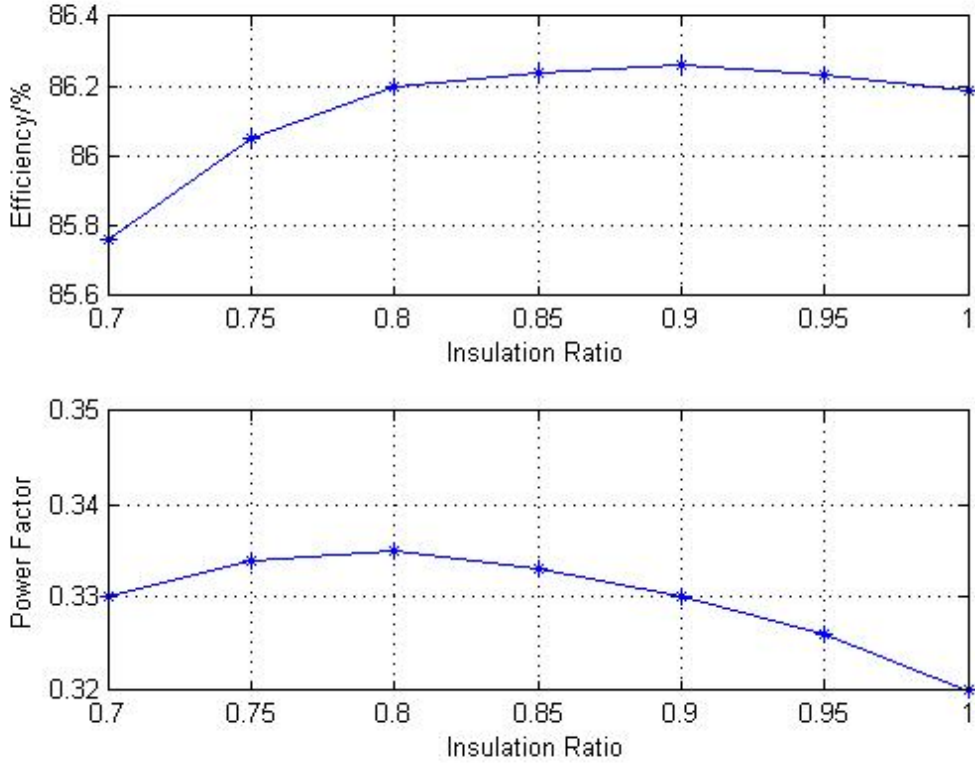


FIGURE 4.3: Efficiency and power factor variation with the rotor insulation ratio in SynRM 3

A local maximum has been found for both efficiency and power factor, but at different insulation ratio values:

- Efficiency maximum, $\eta_{max} = \eta|_{0.9} = 86.26\%$
- Power factor maximum, $\cos(\phi)_{max} = \cos(\phi)|_{0.8} = 0.3350$

It has been decided to characterize SynRM 4 by choosing the insulation ratio that maximizes the efficiency, hence $k_{wq} = 0.9$. The main SynRm 4 simulation results are summarized in Table 4.3.

4.4 Torque ripple optimization

The next step in the design process is the torque ripple optimization. In [2] it is suggested that the main parameters influencing the torque ripple are the number of flux barriers and their position. The purpose of this work is to design a PMaSynRM. Contributing to the torque ripple, but not considered here, the permanent magnet insertion creates

TABLE 4.3: SyRM 4 performance (time-stepping FEM)

Stator Current Density [A/mm^2]	4.43
Air-gap flux Density [T]	0.673
Max St. Yoke Flux Density [T]	1.585
Max St. Tooth Flux Density [T]	1.617
Peak-to-peak Torque Ripple [%]	23.56
Power Factor	0.3299
Efficiency [%]	86.26
k_{wg} [-]	0.9

a cogging torque. However, it is possible to drastically reduce the cogging torque by skewing the motor.

The rotor barriers position is related to the angle β as explained in paragraph 2.4.4, hence this optimization step has been performed by varying the above mentioned angle and the number of barriers. The results from the simulations are displayed in Fig. 4.4, where the parameter Q is directly proportional to the angle β mentioned in chapter 2.

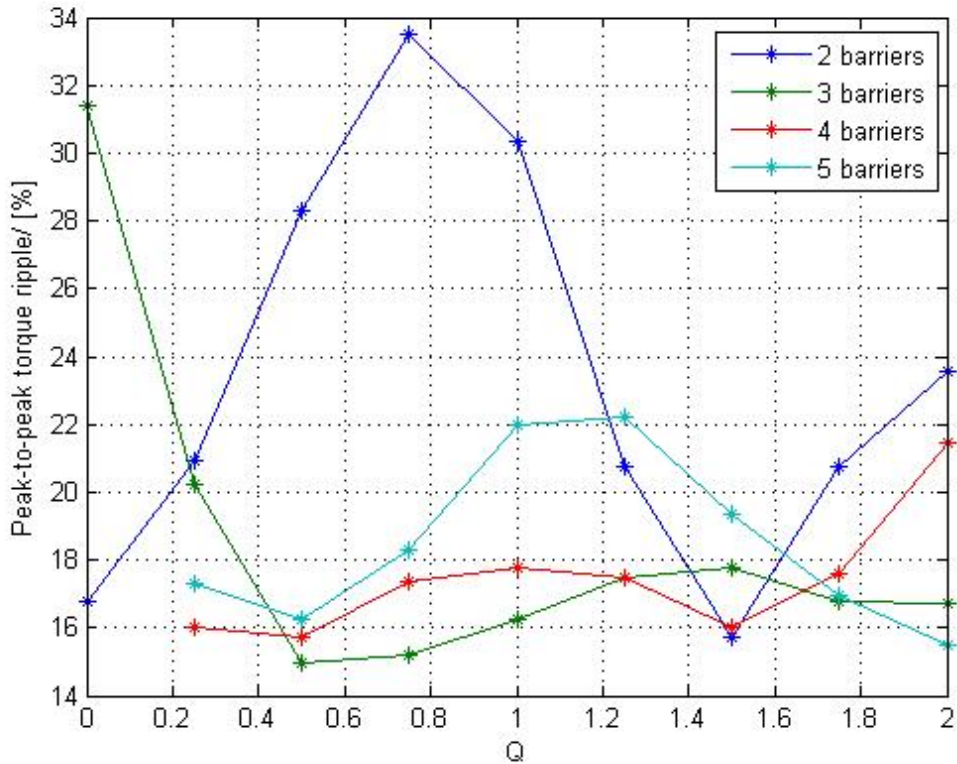


FIGURE 4.4: Torque ripple dependence with the imaginary number of barriers

If B stands for the number of flux barriers, it has been found that the best (B, Q) combinations are $(3, 0.5)$, $(3, 0.75)$ and $(2, 1.5)$. At this point, the combination $(2, 1.5)$ is chosen. It is easier to manufacture lower number of barriers and efficiency and power

factor are slightly higher, even though the obtained torque ripple is slightly larger. SynRM 5 is then defined with the new (B, Q) combination. SynRM 5 relevant simulation results are summarized in Table 4.4 and its geometry is shown in Fig. 4.5.

TABLE 4.4: SynRM 5 performance (time-stepping FEM)

Peak-to-peak Torque Ripple [%]	15.7
Power Factor	0.3256
Efficiency [%]	85.23

The result of this optimization is a torque ripple reduction of 7.86 %, but at the expense of 1.03 % units of efficiency. They both could represent important variations and, depending on the motor application, it could be chosen to remain with the original (B, Q) combination.

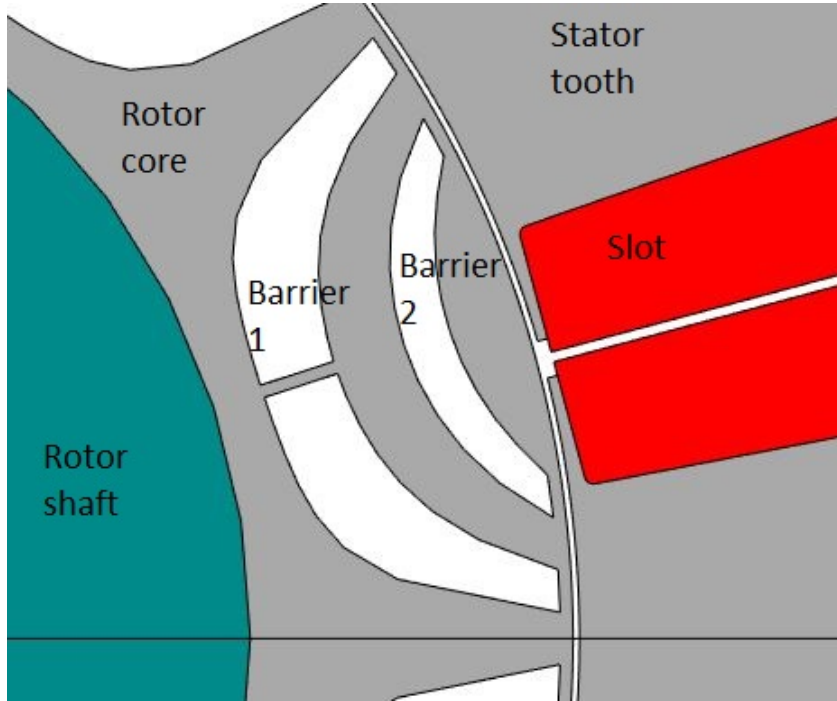


FIGURE 4.5: Optimized geometry for torque ripple

4.5 Slot opening optimization

The slot opening width mainly influences the slot flux leakage and the cogging torque, which could be optimized later when the magnet insertion is done. The cogging torque could be reduced to zero if a closed slot opening was used. Manufacturing challenges (like using magnetic slot wedges) diminish the interest of such a solution. At this stage, an optimization has been performed in order to maximize efficiency and power factor.

SynRm 5 is characterized by a slot opening of 3 mm. The result for slot opening from 1 mm to 19 mm are displayed in Fig.4.6.

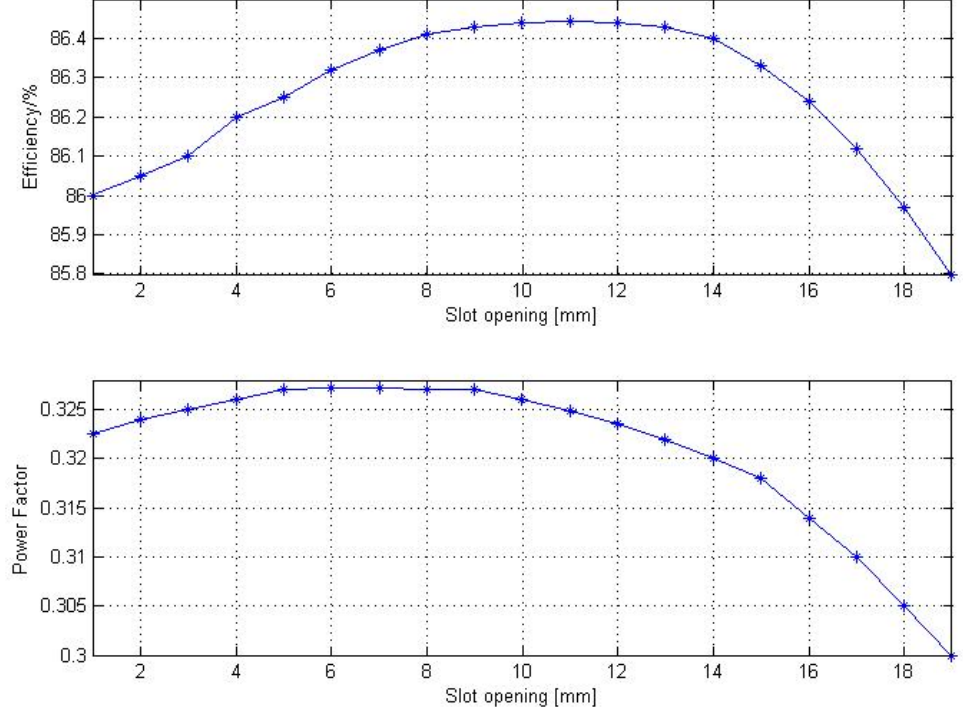


FIGURE 4.6: Efficiency and power factor variation with the stator slot opening in SynRM 5

The chosen slot opening width is 9 mm, which represents a good compromise between efficiency and power factor. SynRM 6 is now defined with a slot opening of 9 mm.

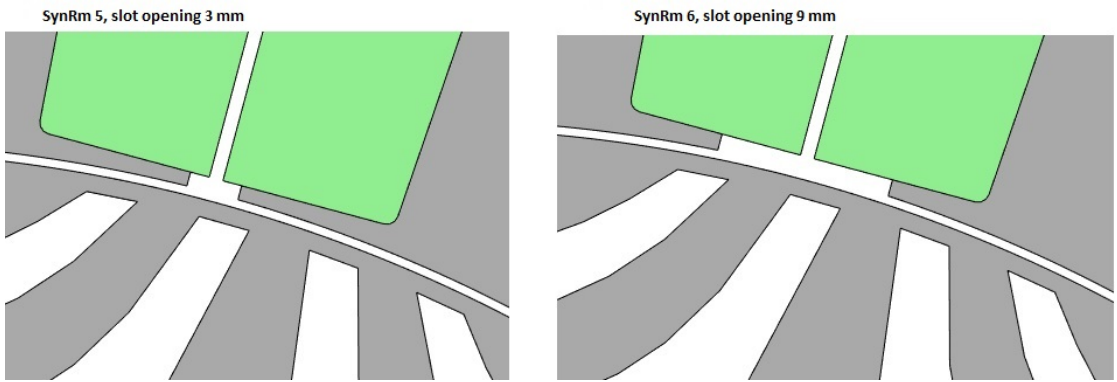


FIGURE 4.7: SynRM 5 and SynRM 6 slot openings

The main SynRM 6 simulation results are summarized in Table4.5.

TABLE 4.5: SynRM 6 performance (time-stepping FEM)

Stator Current Density [A/mm^2]	4.47
Air-gap flux Density [T]	0.711
Max St. Yoke Flux Density [T]	1.611
Max St. Tooth Flux Density [T]	1.612
Power Factor	0.3261
Efficiency [%]	86.46

It is important to say that the slot opening width affects the torque ripple, hence the torque ripple optimization should be performed again. However, it is reasonable to re-optimize the number of barriers and their position after the permanent magnet insertion, in order to take into account also the cogging torque component.

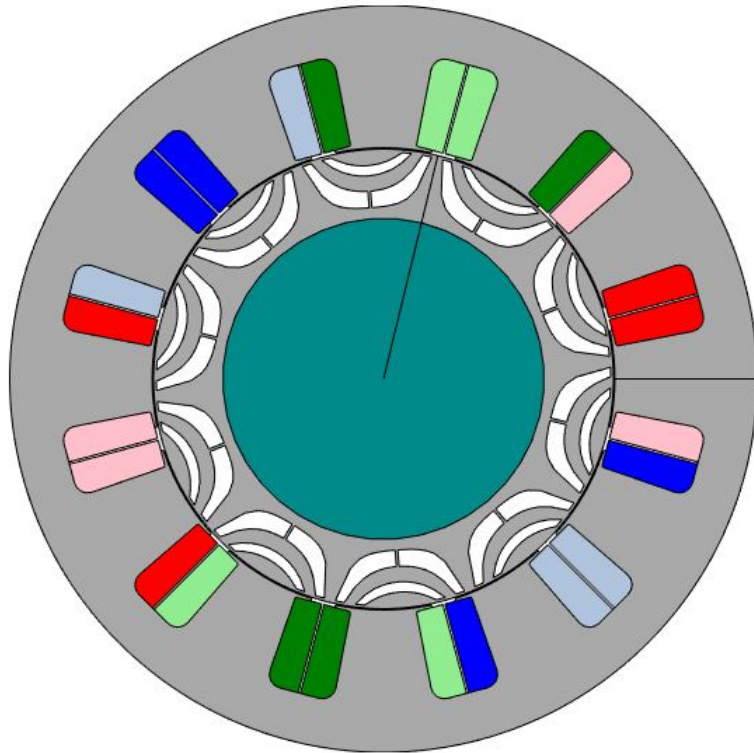


FIGURE 4.8: SynRM 6 geometry

In Fig.4.10, the air-gap flux density first harmonic is very low. Differently, for the MMF distribution, the same harmonic is much larger, as depicted in Fig. 3.4. This is because the presence of flux barriers and the large inner rotor diameter make the sub-harmonics interact with a low magnetic permeance path. Since the sub-harmonics are the most undesired components, in this case it is not worth trying to improve the MMF distribution (using for example multi-layer winding [26] or stator flux barriers [29]).

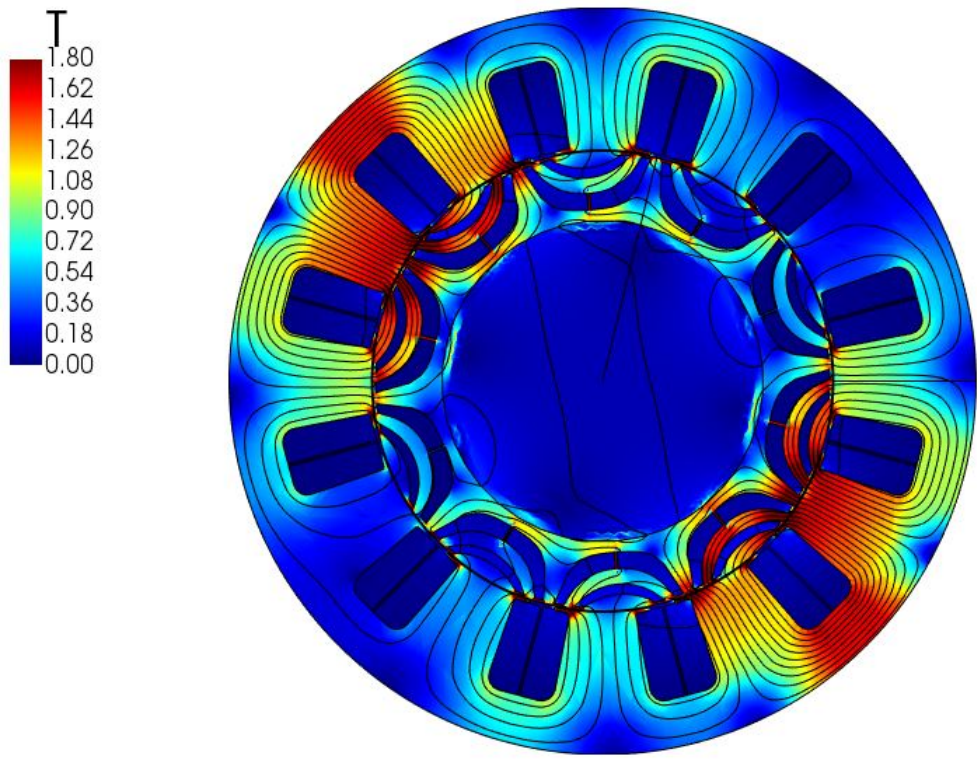


FIGURE 4.9: SynRM 6 flux distribution at nominal load

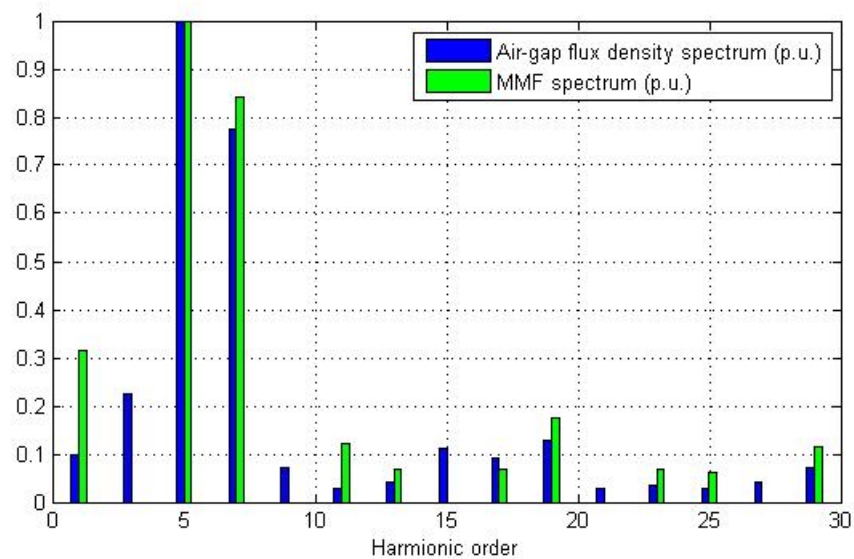


FIGURE 4.10: SynRM 6 Air-gap flux density and MMF spectra in p.u. with reference to the fundamental harmonics

4.6 Conclusions

In this chapter the initial design from Chapter 3 has been optimized and the method has been presented. In particular, the efficiency has been increased from 85.3 % (SynRM 1) to 86.5 % (SynRM 6).

In the next chapter, the problem of the PMs insertion is treated and an optimization process for the resulting PM-assisted motor is carried on.

Chapter 5

Permanent Magnets Insertion

At this point of the motor design procedure, the permanent magnets are inserted in the motor. The optimal amount of magnets is analytically derived and the resulting motor is presented and simulated.

5.1 Nature of the problem

The goal of the permanent magnets is to enhance the power factor and provide PM torque. As shown in chapter 2, it is possible to optimize the amount of permanent magnets employed once the desired value of λ_{PM} is chosen. In literature, a motor is said to be naturally compensated if the relation expressed in Eq.2.38 applies with the equality. This kind of compensation is often desired for low number of poles motors, where the reluctance torque is usually relatively high due to the possibility to reach high anisotropy levels. The higher the number of poles, the lower is the anisotropy effectiveness. Hence, for high number of poles motors, it is useful to compensate the lack of reluctance torque with a larger amount of PMs, with respect to the natural compensation. In this way, it is possible to improve even further the torque and power factor at rated conditions (as visible in the vectorial diagram depicted in Fig.2.14), at the expenses of the flux weakening capability and permanent magnets costs. On the other hand, in order to obtain high efficiency at high speed operation (flux weakening), it is important to keep λ_{PM} under certain values, otherwise the motor would need a demagnetizing positive q-axis current (see equation 2.55). This q-axis current would lower the efficiency because it is not used to produce any torque. In other words a trade-off between the efficiency of the motor at the nominal point and at the maximum speed operation has to be done.

At this stage NdFeB is chosen as permanent magnet material since the final design is expected to be an overcompensated motor. The rare earth permanent magnet material employed is NdFeB 493a and its characteristics are depicted in Fig.5.1, taken from [30]. Initially, the permanent magnets are designed in order to achieve a natural compensation (with the minimum amount of permanent magnet [28]) and later the amount of magnets is gradually increased. The permanent magnet increment is performed by maintaining the optimal geometry.

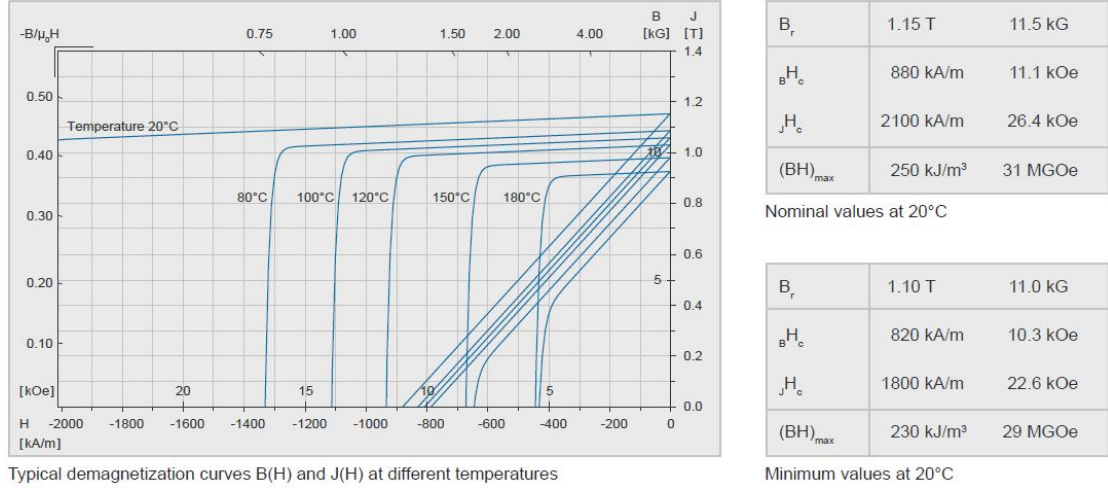


FIGURE 5.1: NdFeB 493a [30]

5.2 Natural compensation

In order to calculate the desired amount of permanent magnets, the geometrical barrier data are summarized in Table 5.1, with reference to Fig.2.22. Flux barriers 1 and 2 are close to the shaft and to the air-gap respectively.

TABLE 5.1: Rotor flux barriers linearised geometric data

	Flux barrier 1	Flux barrier 2
Linearised length a_A [m]	0.0555	0.0323
Average thickness h_A [m]	0.00424	0.0036
Total magnetic rib thickness [m]	0.003	0.002

The magnetic rib length is assumed equal to the average flux barrier thickness. The ribs magnetic model is determined, as described in [28], by considering the M700-50A iron's B-H curve, hence

- $B_R = 2.468T$

- $\mu_R = 13.92$

The only input data to be defined are the q-axis fundamental stator MMF and the relative staircase distribution in the rotor, depicted in Fig5.2.

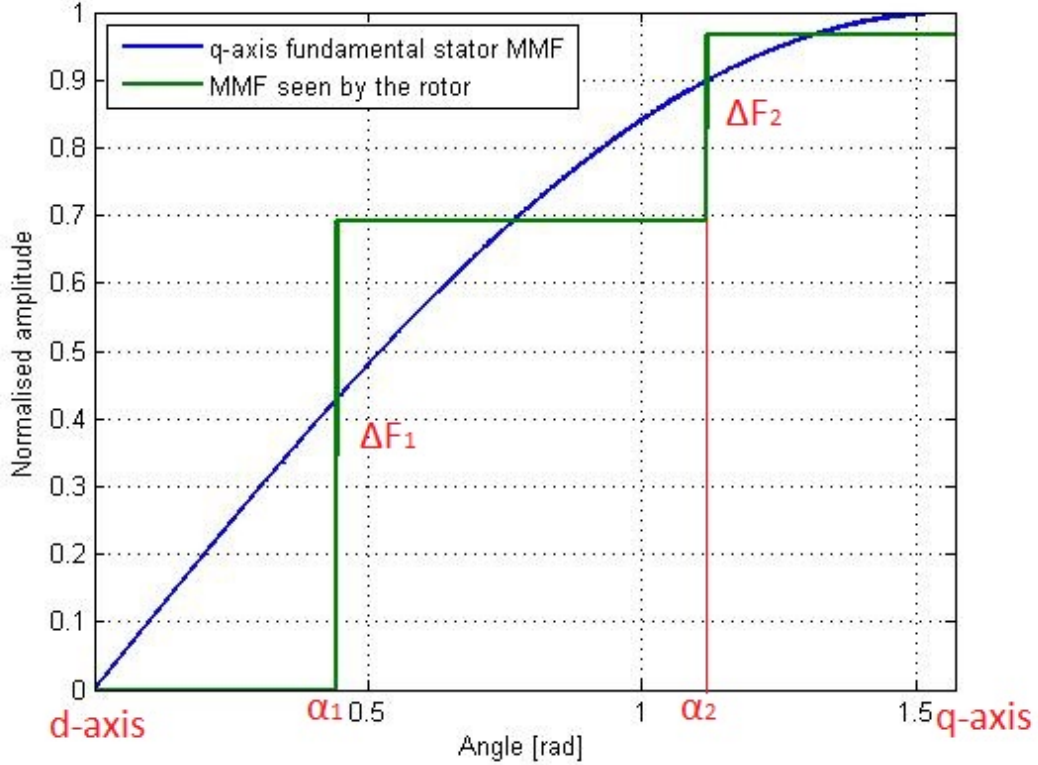


FIGURE 5.2: q-axis fundamental stator MMF and the relative staircase distribution in the rotor

α_1 and α_2 are the angles between the d-axis and the flux barrier end, for barrier 1 and barrier 2, respectively. In SynRM 6, they are

- $\alpha_1 = 0.444 \text{ el. rad} = 24.44 \text{ el.}^\circ$
- $\alpha_2 = 1.11875 \text{ el. rad} = 64.1 \text{ el.}^\circ$

The q-axis fundamental stator MMF peak is given by

$$F_p = \frac{3}{\pi} \frac{N}{p} k_w I_Q = 1436 At \quad (5.1)$$

$$N = n_s(2pq) = 92 \quad (5.2)$$

where N is the number of turns per phase, p is the number of pole pairs, k_w is the winding factor and $I_Q = 87.65A$ is the q-axis current peak at nominal condition. Since the MMF

staircase represents the average, in a certain angle span, of the q-axis fundamental stator MMF, it is possible to calculate ΔF_1 and ΔF_2 (see Fig. 5.2) by simple integrations

- $\Delta F_1 = \frac{1}{\alpha_2 - \alpha_1} \int_{\alpha_1}^{\alpha_2} \hat{F} \sin(\alpha) d\alpha = 993At$
- $\Delta F_2 = \frac{1}{\frac{\pi}{2} - \alpha_2} \int_{\alpha_2}^{\frac{\pi}{2}} \hat{F} \sin(\alpha) d\alpha - \Delta F_1 = 396At$

It is now possible to apply equations 2.48, 2.49, 2.50 and insert them into 2.52 and 2.53. The resulting permanent magnets optimal geometry is given in Table 5.2.

TABLE 5.2: Permanent magnets optimal dimensions for natural compensation

	PM in barrier 1	PM in barrier 2
Optimal magnet thickness [mm]	1.61	0.716
Optimal magnet width [mm]	47	19
Optimal cross-sectional magnet surface [mm^2]	75.67	13.604

5.3 Over compensation

In literature, a motor is said to be overcompensated if the amount of PMs exceeds the definition of natural compensation (given at paragraph 5.1). For the above mentioned reasons, it is of interest to overcompensate the motor. The design problem is mainly to understand how much the motor should be overcompensated. In order to chose the best solution, several overcompensation levels are simulated. It is of interest to maintain the optimal magnet dimensions (i.e., minimum cross-sectional area) even when the natural compensation is exceeded. In order to do this, it is necessary to find the ratio between the optimal thickness and width of the permanent magnets for the general case.

The equation 2.45, when the compensation is not natural (i.e., $\phi \neq 0$ in Fig. 2.22), becomes

$$F_M = R_M \left\{ \left(\frac{1}{R_A} + \frac{1}{R_M} + \frac{1}{R_R} \right) \Delta F + \frac{F_R}{R_R} + \phi \left[1 + 2R_g \left(\frac{1}{R_A} + \frac{1}{R_M} + \frac{1}{R_R} \right) \right] \right\} \quad (5.3)$$

where,

$$2R_g = \frac{\delta}{\mu_0 \frac{\xi_k \xi_{k+1}}{\xi_k + \xi_{k+1}} Dl} \quad (5.4)$$

is the total air-gap reluctance relative to a flux barrier. ξ_k and ξ_{k+1} are respectively the angles covering the superior and inferior endings of the two flux paths adjacent to the k -th barrier, as depicted in Fig. 2.17.

At this point, it is possible to derive

$$a_M = \frac{\frac{h_A}{l} \{ \phi [1 + 2R_g(\frac{\mu_0 a_A l}{h_A} + \frac{1}{R_R})] + \frac{F_R}{R_R} + \Delta F(\frac{1}{R_R} + \frac{\mu_0 a_A l}{h_A}) \} h_M}{[\mu_r B_r h_A + \phi 2R_g \mu_0 + \Delta F \mu_0] h_M - (\phi 2R_g + \Delta F) \mu_0 \mu_r h_A} \quad (5.5)$$

Then the PM cross-sectional area expression becomes

$$S_M = a_M h_M = \frac{\frac{h_A}{l} \{ \phi [1 + 2R_g(\frac{\mu_0 a_A l}{h_A} + \frac{1}{R_R})] + \frac{F_R}{R_R} + \Delta F(\frac{1}{R_R} + \frac{\mu_0 a_A l}{h_A}) \} h_M^2}{[\mu_r B_r h_A + \phi 2R_g \mu_0 + \Delta F \mu_0] h_M - (\phi 2R_g + \Delta F) \mu_0 \mu_r h_A} \quad (5.6)$$

The minimum permanent magnet cross-sectional area (i.e. the minimum volume, since the magnets length is fixed as the active length of the motor) is found by imposing its partial derivative equal to zero

$$\frac{\partial S_M}{\partial h_M} = 0 \quad (5.7)$$

As a result, the optimal magnet thickness and width are given by

$$h_{Mopt} = \frac{2(\phi 2R_g + \Delta F) \mu_0 \mu_r h_A}{\mu_r B_r h_A + (\phi 2R_g + \Delta F) \mu_0} \quad (5.8)$$

$$a_{Mopt} = \frac{\frac{2h_A}{l} \{ \phi [1 + 2R_g(\frac{\mu_0 a_A l}{h_A} + \frac{1}{R_R})] + \frac{F_R}{R_R} + \Delta F(\frac{1}{R_R} + \frac{\mu_0 a_A l}{h_A}) \}}{\mu_r B_r h_A + (\phi 2R_g + \Delta F) \mu_0} \quad (5.9)$$

and

$$\frac{h_{Mopt}}{a_{Mopt}} = \frac{(\phi 2R_g + \Delta F) \mu_0 \mu_r l}{\phi [1 + 2R_g(\frac{\mu_0 a_A l}{h_A} + \frac{1}{R_R})] + \frac{F_R}{R_R} + \Delta F(\frac{1}{R_R} + \frac{\mu_0 a_A l}{h_A})} \quad (5.10)$$

It is now possible to increase one of the two magnet dimensions and, at the same time, vary the other one with eq. 5.10 in order to have always the optimal amount of magnets. In this way, all the desired compensation level of the motor can be simulated and the optimal permanent magnet dimensions combination is maintained. The optimal magnet thickness and width ratio dependence on the q-axis flux is depicted in Fig.5.3.

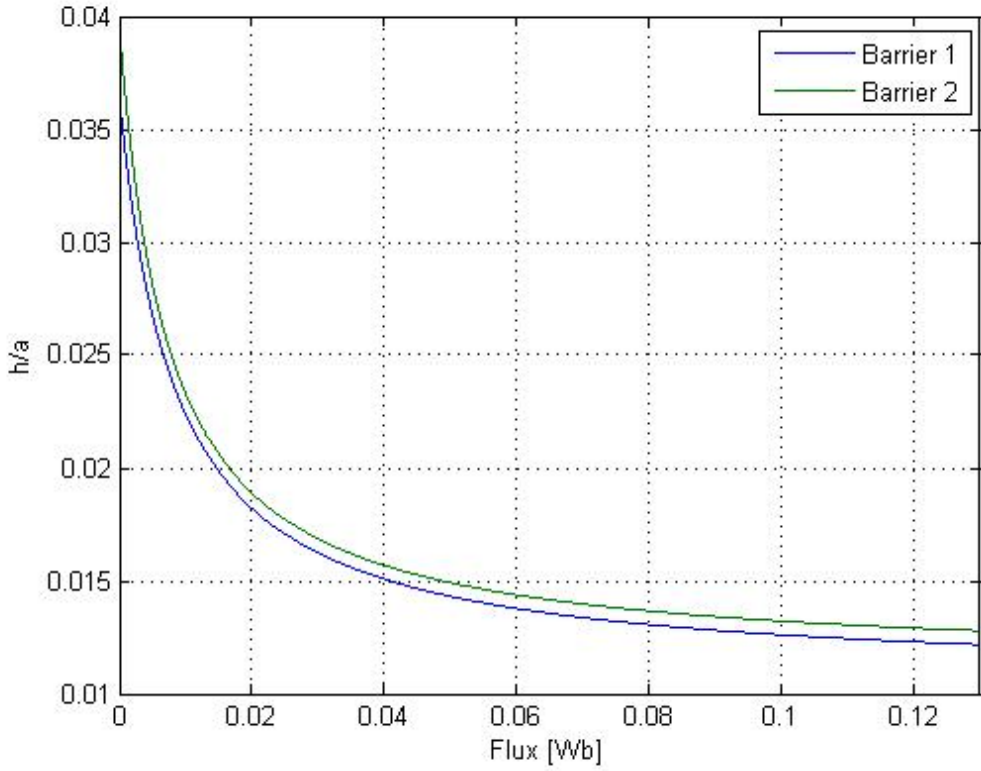


FIGURE 5.3: Optimal magnet thickness and width ratio dependence on the q-axis flux

The higher the flux, the higher is the MMF drop inside the magnet. Moreover, since $R_M \propto \frac{h_M}{a_M}$, the higher the flux, the lower is $\frac{h_{M\text{opt}}}{a_{M\text{opt}}}$.

5.4 Minimum and maximum allowed compensation

Not all the compensation levels can be reached because of the constraints due to

- the flux weakening capability, which sets a superior limit to the amount of permanent magnet that can be used, and
- the risk of demagnetization, which sets an inferior limit to the amount of permanent magnet that can be used.

5.4.1 Flux weakening capability limit

Based on the theory given in chapter 2, it is possible to state that the motor has its minimum flux linkage when it is operated at maximum speed. The required maximum

speed for the application is $\omega_{max} = 6000 rpm = 628.32 \frac{rad}{s}$ and the phase voltage is $V_{ph} = 220V$. Hence, the minimum flux of the motor has to be

$$\phi_{min} = \frac{\lambda_{min}}{N} = \frac{\frac{V_{ph}}{\omega_{max}}}{N} = 3.810^{-3} Wb \quad (5.11)$$

where, λ_{min} is the minimum linked flux to the phase winding and N is the number of turns per phase. In order to reach the maximum speed, the permanent magnet flux has to fulfill the following relation

$$\phi_{min} \geq \phi_{PM} - L_q I_{q0} \quad (5.12)$$

hence

$$\phi_{PM} \leq \phi_{min} + L_q I_{q0} = 0.1496 Wb \quad (5.13)$$

since, in SynRM 6, $L_q = 1.9367 mH$ and $I_{q0} = 75.3A$ (q-axis current retrieved from FEM simulations). It is wanted to maintain the same PM balance among the barriers found for the natural compensation. Thus, the ratio between the flux provided by the PMs in the barriers must be kept constant and from equation 5.3 (where ΔF is set to zero) it is possible to retrieve

$$\frac{\phi_{barr1}}{\phi_{barr2}} = \frac{\phi_{barr1-NAT}}{\phi_{barr2-NAT}} = 2.259 \quad (5.14)$$

It is now possible to write

$$\phi_{PM} = \phi_{barr1} + \phi_{barr2} = \phi_{barr1} \left(1 + \frac{\phi_{barr2-NAT}}{\phi_{barr1-NAT}}\right) < \phi_{min} + L_q I_0 = 0.1496 Wb \quad (5.15)$$

which yields

$$\phi_{barr1} < \frac{\phi_{min} + L_q I_0}{1 + \frac{\phi_{barr2-NAT}}{\phi_{barr1-NAT}}} \quad (5.16)$$

and, in an analogous way

$$\phi_{barr2} < \frac{\phi_{min} + L_q I_0}{1 + \frac{\phi_{barr1-NAT}}{\phi_{barr2-NAT}}} \quad (5.17)$$

If equation 5.8 is reversed and ΔF is set to zero, the following equation is found for the flux provided by a magnet

$$\phi_{barr} = \frac{\mu_r B_r h_A h_{Mopt}}{\mu_0 (2\mu_r h_A - h_{Mopt}) 2R_g} \quad (5.18)$$

After rearranging the equations 5.16, 5.17 and 5.18, it is possible to express the optimal magnet thickness upper limit as

$$(h_{Mopt1})_{limit} = \frac{2\mu_r h_{A1}}{1 + \frac{\mu_r B_r h_{A1}}{\mu_0 2R_{g1}} \frac{1 + \frac{\phi_{barr2-NAT}}{\phi_{barr1-NAT}}}{\phi_{min} + L_q I_0}} = 4.78mm \quad (5.19)$$

$$(h_{Mopt2})_{limit} = \frac{2\mu_r h_{A2}}{1 + \frac{\mu_r B_r h_{A1}}{\mu_0 2R_{g2}} \frac{1 + \frac{\phi_{barr1-NAT}}{\phi_{barr2-NAT}}}{\phi_{min} + L_q I_0}} = 2.83mm \quad (5.20)$$

5.4.2 Risk of demagnetization limit

The minimum magnet thickness which ensures the PMs are not demagnetized has to be retrieved by taking into account the maximum current (here considered to be 150% of the nominal value). Equation 2.54 in chapter 2 is used to find the normalized values

$$y_{1demag} = \frac{\mu_0 \Delta F_1}{B_{wc} h_{1A}} = 0.882 \quad (5.21)$$

$$y_{2demag} = \frac{\mu_0 \Delta F_2}{B_{wc} h_{2A}} = 0.414 \quad (5.22)$$

hence

$$(h_{M1})_{min} = y_{1demag} h_{1A} = 3.735mm \quad (5.23)$$

$$(h_{M2})_{min} = y_{2demag} h_{2A} = 1.4895mm \quad (5.24)$$

if the minimum flux density is set to $B_{wc} = 0.5$ T. Since, $(h_{M1})_{min}$ and $(h_{M2})_{min}$ are not designed with respect to eq. 5.14, hence $(h_{M1})_{min}$ is fixed and $(h_{M2})_{min}$ is calculated as a consequence by inserting equation 5.18 into 5.14

$$(h_{M2})_{min} = 2.02mm \quad (5.25)$$

5.5 PMaSynRM design

The retrieved optimal magnet thickness and width limits are summarized in Table 5.3.

TABLE 5.3: Optimal magnet thickness and width values for natural compensation, demagnetization risk limit and flux-weakening capability limit

	h_{Mopt1} [mm]	h_{Mopt2} [mm]	a_{Mopt1} [mm]	a_{Mopt2} [mm]
Natural comp.	1.61	0.716	47	19
Demagn. risk limit (min)	3.735	2.02	275.5	142.4
Flux-weak. cap. limit (max)	4.78	2.83	390.4	218.5

The optimal magnet width, in the range comprising the demagnetization risk limit and the flux-weakening capability limit, exceeds the barrier width, given in Table 5.1. Thus, the magnet amount cannot be optimized for this motor. However, this result suggests that the magnets need to occupy all the possible barriers length. Moreover, in [28] it is said that the design technique in which the barrier space left free from the magnet thickness is replaced with iron is more effective. It provides the maximum path width for the d-axis flux. So the flux barrier space should be filled with permanent magnet material and then, in order to regulate the amount of magnet, optimize the insulation ratio, as it has been defined previously for SynRM motors. In this case, eq. 5.14 is not any more assured.

The permanent magnet tips have been cut off. This solution gives two main benefits: primarily it reduces PM losses (conductive materials close to the air-gap experience more eddy currents) and secondarily reduces the risk of demagnetization (PMs close to the air-gap are exposed to stronger demagnetizing fields). As a result, the efficiency increases but the power factor decreases.

After optimization of the number of turns which led to a value of 35, the insulation ratio of the motor filled with permanent magnet has been varied from 0.2 to 1.5. The magnet insertion allows to drastically reduce the nominal current (since the motor is magnetized also by the permanent magnets) and hence, the current density is also greatly lowered. As a consequence, the electric and magnetic loadings have to be optimized

again by re-adapting the number of turns. For the insulation ratio, a good choice is $k_w = 0.8$ since it gives both high efficiency and power factor. The optimal efficiency is reached with a slot opening of 9 mm and a number of barriers and position identified by $(QP2, QPI) = (2, 1.5)$. It is now possible to characterize the motor PMaSynRM with the selected parameters and summarize the simulation results in Table 5.4.

TABLE 5.4: PMaSyRM 1 performance

Stator current density [A/mm^2]	1.99
Air-gap flux density [T]	0.768
Max st. yoke flux density [T]	0.706
Max st. tooth flux density [T]	0.920
Power factor	0.99
Efficiency [%]	94.43

From table 5.4, it is evident that the motor is not well exploited since the electrical and magnetic loadings are far lower than what they usually are for this kind of motors. It means that this motor can easily support a higher rated power or be downsized (as it is done later on in this chapter).

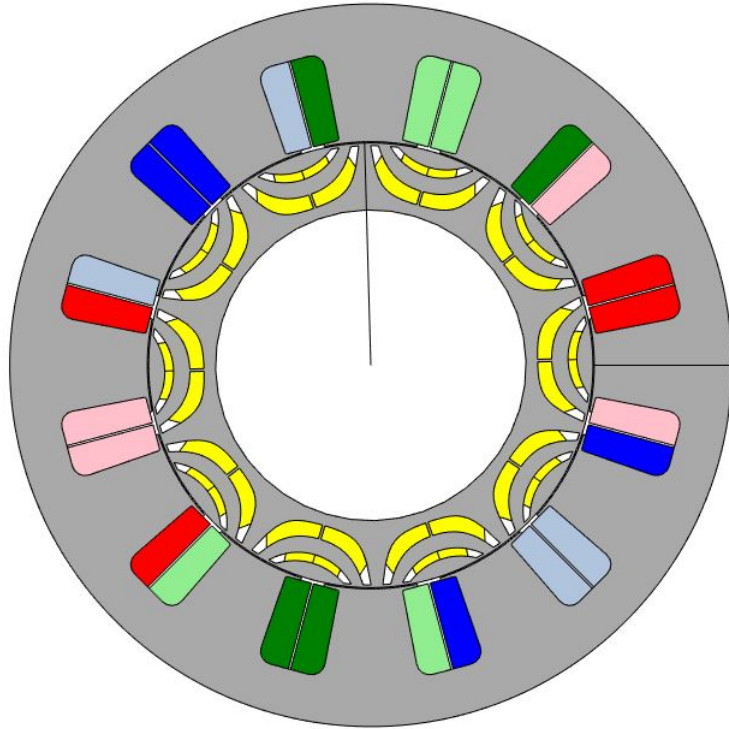


FIGURE 5.4: PMaSynRM 1 motor geometry

The discussion about the air-gap flux density sub-harmonics in SynRM 6 applies also for PMaSynRM. In PMaSynRM, the sub-harmonics are even more lowered. The 1st, 3rd

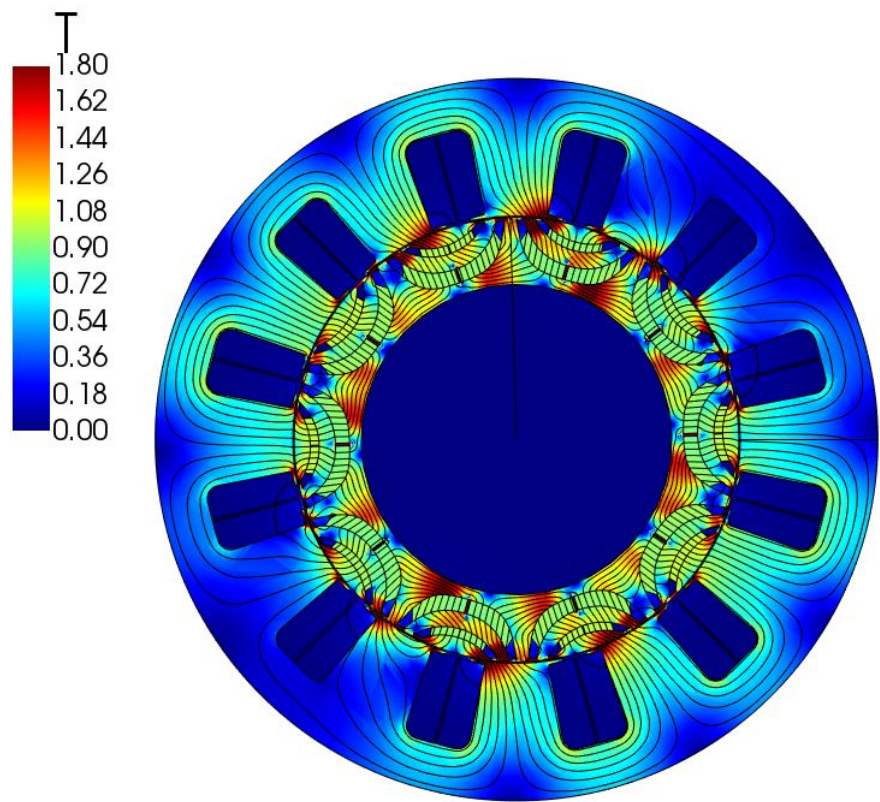


FIGURE 5.5: PMaSynRM 1 flux lines and flux density distribution at nominal load

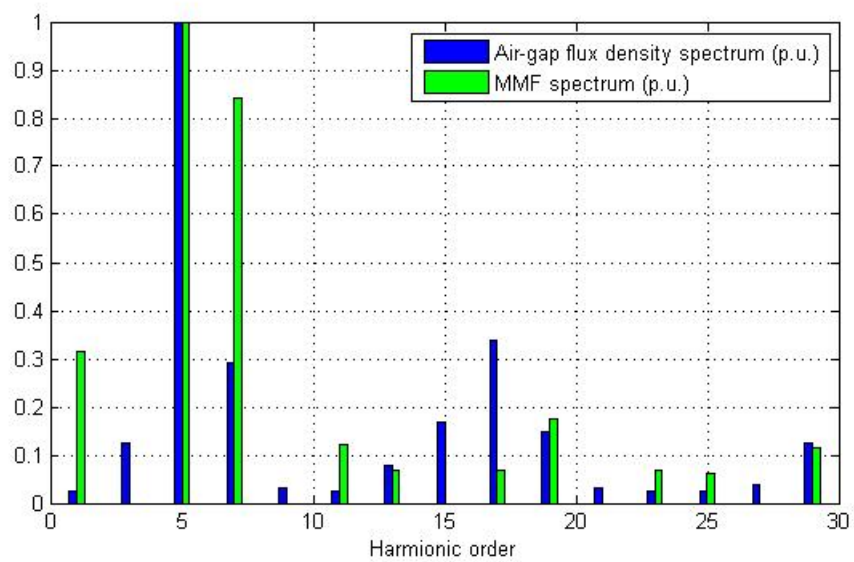


FIGURE 5.6: PMaSynRM 1 Air-gap flux density and MMF spectra in p.u. with reference to the fundamental harmonics

and 7th harmonics are lowered, while the higher order harmonics (from the 15th) are increased.

5.6 Thermal aspects and model refinement

The FEM simulations performed in this work do not take thermal aspects into account. Hence, for an ambient temperature of 25°C, the stator and rotor temperature rises have been set to

- $\Delta T_S = 60K$
- $\Delta T_R = 45K$

The stator and rotor temperature rises represent the maximum temperature difference between the stator and the rotor with respect to the ambient, respectively. This fact introduces an error in the real temperature of the motor parts under operation. This temperature error reflects on the efficiency computation, since the copper resistivity depends on the copper temperature. In order to make the model more precise and trustful, the rotor and stator temperature rises have to be calculated analytically. For this purpose, the following empirical formulas, known as Broströms Formulas [8], have been used

$$\Delta T_{ST} = k_{CS} \sqrt{P_{CU_{ST}} P_{TOT}} \quad (5.26)$$

$$\Delta T_{RO} = k_{CR} \sqrt{P_{CU_{RO}} P_{TOT}} \quad (5.27)$$

where, k_{CS} and k_{RO} are empirical coefficients based on measurements (depending on geometry and cooling capability) and the other elements are self-explanatory. Since the copper losses and the total losses depends on the temperature rise, because of the resistivity variation, it is necessary to solve the equations by iterations. The Broströms Formulas are intended for both synchronous and induction motors, but it can be stated that for synchronous motors only the stator temperature rise appreciably influences the copper losses. Thus, only the stator equation has been employed and the temperature difference between the stator and rotor temperature rises has been assumed to be 15 K.

The values for PMaSynRM 5 of the temperature rise, efficiency and power factor retrieved after the iterative process are

- $\Delta T_{ST} = 19.3K$
- Efficiency = 94.45%

when the ambient temperature is 25 °C. It is possible to conclude that even a 25 K temperature rise variation makes a negligible difference on efficiency. This is due also because of the low load of the motor.

5.7 Motor Dimension Reduction

It can be inferred from the temperature rise, the low current density and the low flux density, that the motor is oversized for the required power and speed. For these reasons, the geometry selected for the PMaSynRM design is now adapted to the following dimensions (taken from two reference 4-pole 15 kW SynRM and IM motors)

- Outer diameter, D = 136 mm
- Active length, L = 190 mm

The slot dimensions, the rotor internal diameter and the stator external diameter have been scaled in order to maintain the same proportion. The retrieved values are shown in Table 5.5.

TABLE 5.5: Dimension reduction

	Re-sized motor	Original motor
Inner rotor diameter [mm]	94.5	117.7
Stator slot height [mm]	23	28
Stator slot width [mm]	18.5	23

The performance parameters are summarized in Table 5.6.

TABLE 5.6: PMaSyRM 2 performance

Stator Current Density [A/mm^2]	4.17
Air-gap flux Density [T]	0.82
Max St. Yoke Flux Density [T]	1.26
Max St. Tooth Flux Density [T]	0.86
Power Factor	0.94
Efficiency [%]	94.65
PM amount [Kg]	2.74

5.8 PMaSynRM with Ferrite

The PMaSynRM geometry has been simulated also with ferrite as permanent magnet material. Even if the ferrite conductivity is much lower, the rotor barriers have not be filled entirely in order to improve the demagnetization resistance of the motor. The employed ferrite corresponds to the code NMF-7F and its BH curve is depicted in Fig.5.7, taken from [31].

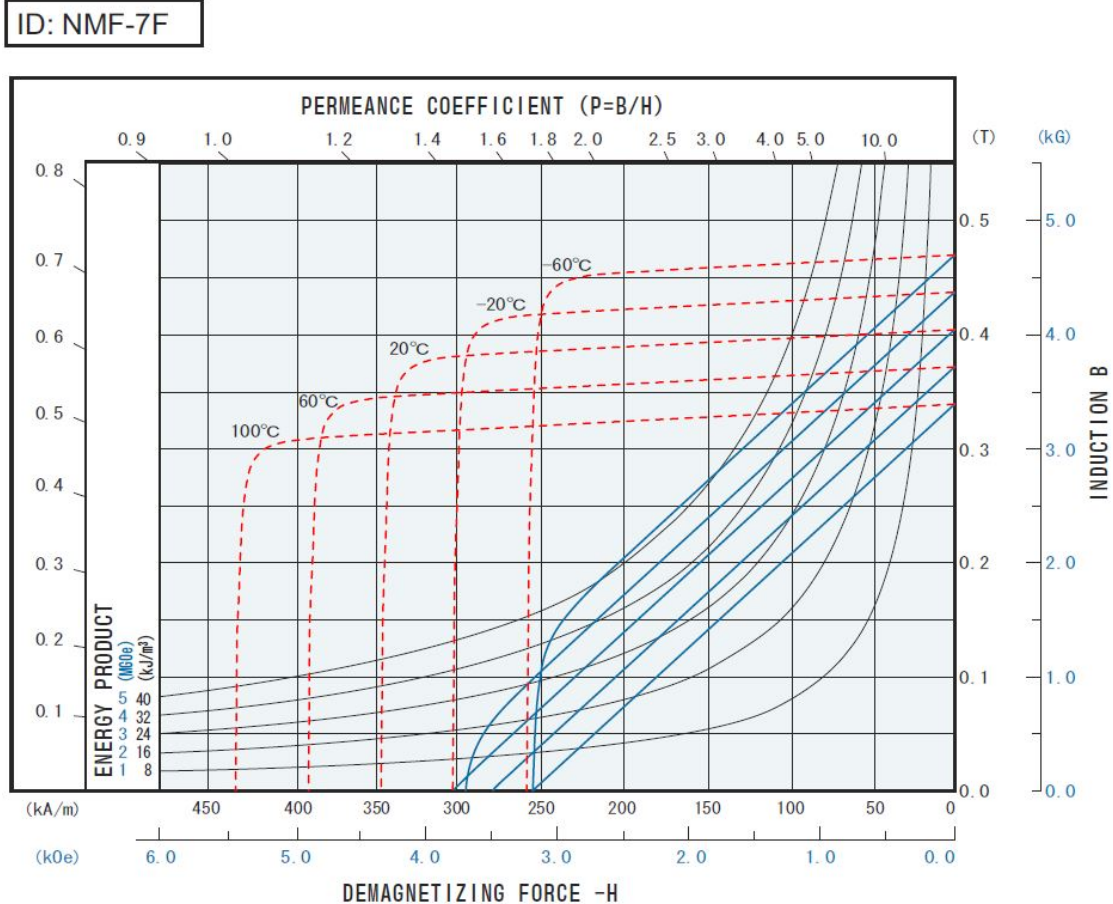


FIGURE 5.7: Employed ferrite magnetization curve [31].

The PMaSynRM ferrite performance are summarized in Table 5.7.

TABLE 5.7: PMaSyRM with ferrite performance

Stator Current Density [A/mm^2]	6.23
Air-gap flux Density [T]	0.665
Max St. Yoke Flux Density [T]	1.64
Max St. Tooth Flux Density [T]	1.70
Power Factor	0.52
Efficiency [%]	91.03
PM amount [Kg]	1.79

The higher electric loading shown in table 5.7, in terms of current density, reflects the weaker PM effect. In order to get the same torque the motor needs an higher current. This result confirms the poor reluctance performance characterizing the 10-pole PMaSynRM motor, regardless of the PM material employed. As long as it has a strong PM torque contribution, its performance is still acceptable but a large amount of rare earth magnet has to be employed. Due to the poor performance, this motor will not be included in the coming comparisons.

5.9 Conclusions

In this part of the thesis the problem of the PMs insertion has been dealt. An analytical PM volume minimization method has been presented and used. The retrieved PMs geometry does not fit into the rotor barriers, hence it was not possible to apply the above mentioned method in this case. An alternative and simpler approach has been proposed.

Mainly due to the large amount of PMs employed, the obtained motor design is considered to be unsatisfactory. In the next chapter, several design alternatives are introduced and compared.

Chapter 6

Alternative Motor Designs

In this chapter, a V-shaped IPM (Interior Permanent Magnets) and a SMPM (Surface Mounted Permanent Magnet) rotor topologies are proposed as alternatives to the 10-pole PMaSynRM designs described in chapters [Chapter 5](#). Moreover, two 8-pole PMaSynRM solutions are also proposed. In order to make a reasonable comparison core length, rotor external diameter and stator external diameter are kept the same as well as the winding type (12 slots, double-layer concentrated) in all the motors.

6.1 V-shaped IPM topology

The proposed V-shaped IPM rotor geometry, flux density and flux lines at rated working point are presented in Fig. [6.1](#). The physical data and performance are shown in Table [6.1](#) and the motor loss distribution at rated working point and 70 °C is given in Fig.[6.2](#).

In this case, the rotor geometry parameters subjected to optimization are the magnet thickness, length and opening angle.

6.2 SMPM topology

The proposed SMPM rotor geometry is shown in Fig.[6.3](#) and its data is summarized in Table [6.2](#). In this case, the rotor geometry parameters subjected to optimization are the magnet thickness, magnet length and span angle. The optimal PM geometry was found with a lower PM volume, with respect to PMaSynRM 5. More precisely, it does not give considerable advantage to increase the magnet thickness and it is counterproductive to increase the magnet width (flux leakage increases and eventually the PM losses).

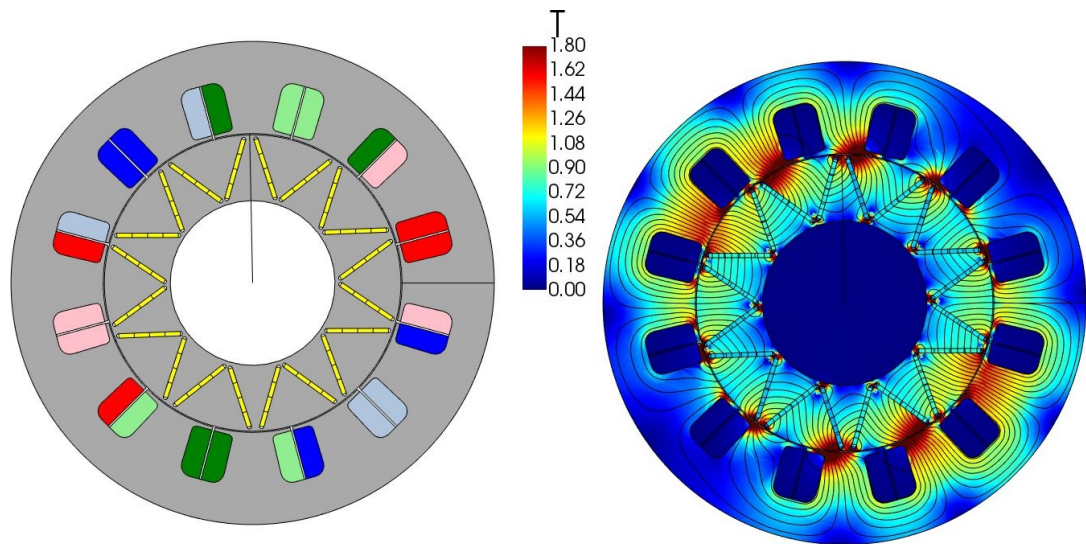


FIGURE 6.1: V-shaped IPM motor geometry, flux density and flux lines at rated working point

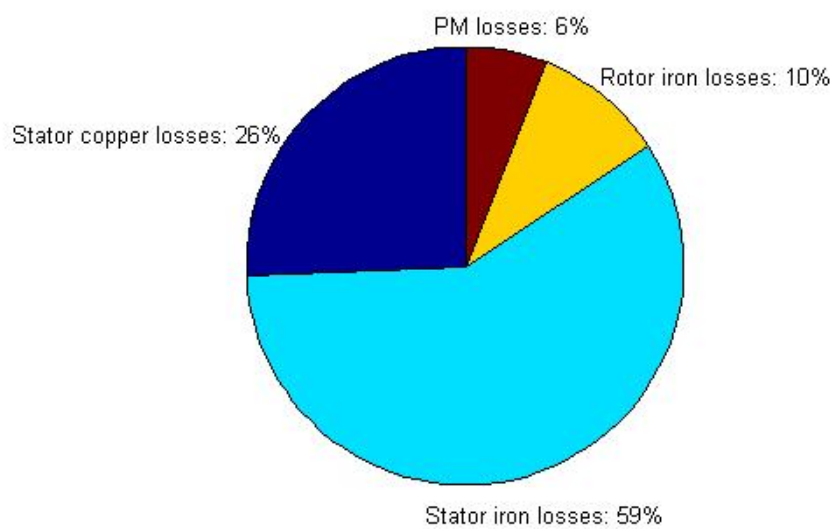


FIGURE 6.2: V-shaped IPM motor loss distribution at rated working point and magnet temperature at 70 °C

TABLE 6.1: V-shaped IPM geometrical and performance data at ambient temperature
 25°C

Magnet thickness [mm]	2
Magnet width [mm]	28
Inner rotor diameter [mm]	75
Outer diameter [mm]	220
Stator slot height [mm]	16
Stator slot width [mm]	19.5
Stator slot opening width [mm]	1
Effective conductors per slot	35
PM amount [kg]	1.6
Rated efficiency %	95.24
Rated power factor	0.99
Peak-to-peak Torque Ripple [%]	14.7
Stator Temp. Rise [K]	23

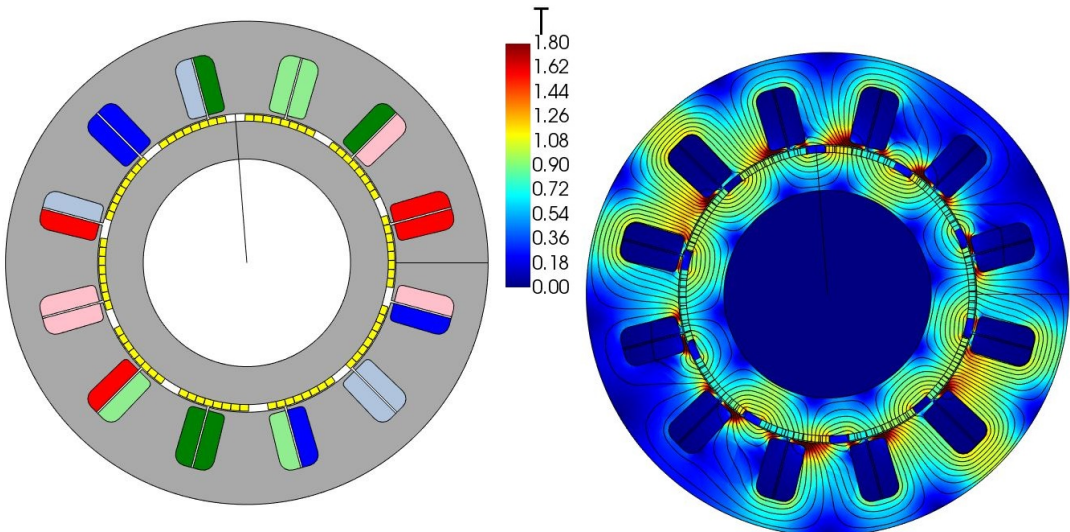


FIGURE 6.3: SMPM motor geometry, flux density and flux lines at rated working point

6.3 8-pole PMaSynRM

As extensively explained in [32], the 10-pole/12 slots combination provides poor reluctance performance. Moreover, it is also shown that this combination is particularly affected by cross-saturation phenomena. In order to get rid of this inconvenience, it is possible to adopt a different winding (distributed or, as suggested in [32], a non-conventional winding with an higher number of stator slots) or change the slot/pole combination. For this reason, the comparison study has been extended to the 8 poles/12 slots combination.

The 8-pole SynRM geometry is shown in Fig.6.5 and its relevant data are summarized in Table 6.3.

TABLE 6.2: SMPM geometrical data and performance data at ambient temperature 25°C

Magnet thickness [mm]	3
Magnet width [mm]	32
Magnet span [%]	75.16
Inner rotor diameter [mm]	94.5
Outer diameter [mm]	220
Stator slot height [mm]	20
Stator slot width [mm]	17.5
Stator slot opening width [mm]	1
Effective conductors per slot	42
PM amount [Kg]	1.37
Rated efficiency [%]	95.7
Rated power factor	0.99
Peak-to-peak Torque Ripple [%]	14.14
Stator Temp. Rise [K]	25

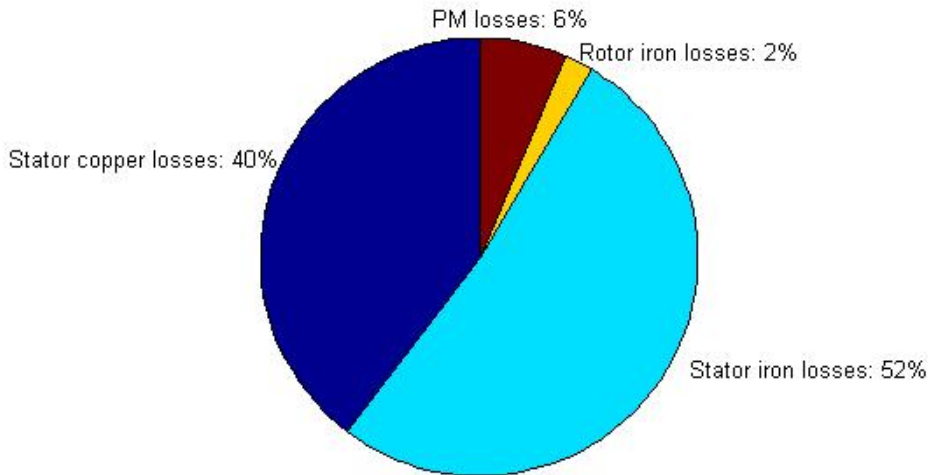


FIGURE 6.4: SMPM motor loss distribution at rated working point and magnet temperature 70°C

The 8-pole SynRM motor efficiency and power factor are very much larger than the 10-pole SynRM motor performance, presented in Table 4.5.

Moreover, because of the relatively good reluctance performance of the 8 poles/12 slots combination, two 8 poles PMaSynRM motors have been designed with two different inserted PM material: NdFeB and ferrite. Information about costs and characteristics of these materials are given in Paragraph 2.2.

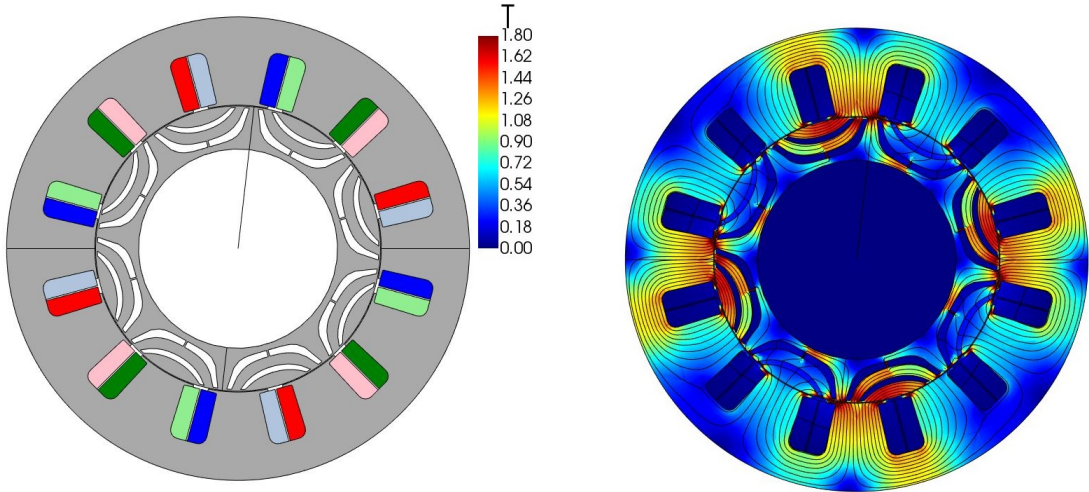


FIGURE 6.5: 8-pole SynRM motor geometry, flux density and flux lines at rated working point

TABLE 6.3: 8-pole SynRM geometrical and performance data at ambient temperature 25 °C

Insulation ratio	0.7
Number of barriers	2
Inner rotor diameter [mm]	117.7
Outer diameter [mm]	273.7
Stator slot height [mm]	31.66
Stator slot width [mm]	21
Stator slot opening width [mm]	9
Rated efficiency [%]	91.11
Rated power factor	0.4774

6.3.1 NdFeB assisted motor

The proposed PMaSynRM rotor geometry, flux density and flux lines at rated working point are shown in Fig.6.6, the relevant geometric dimensions are summarized in Table 6.4 and the loss distribution at rated working point and magnet temperature 70 °C are given in Fig. 6.7.

It is immediately noticeable that the 8-pole motor has better performance in terms of efficiency with a lower amount of PMs used. This is due to the higher reluctance achievable, despite of a lower winding factor.

6.3.2 Ferrite assisted motor

The employed ferrite is the same as presented in the previous chapter for the 10-pole motor. A small region of the rotor barrier, close to the air-gap, was left empty. This

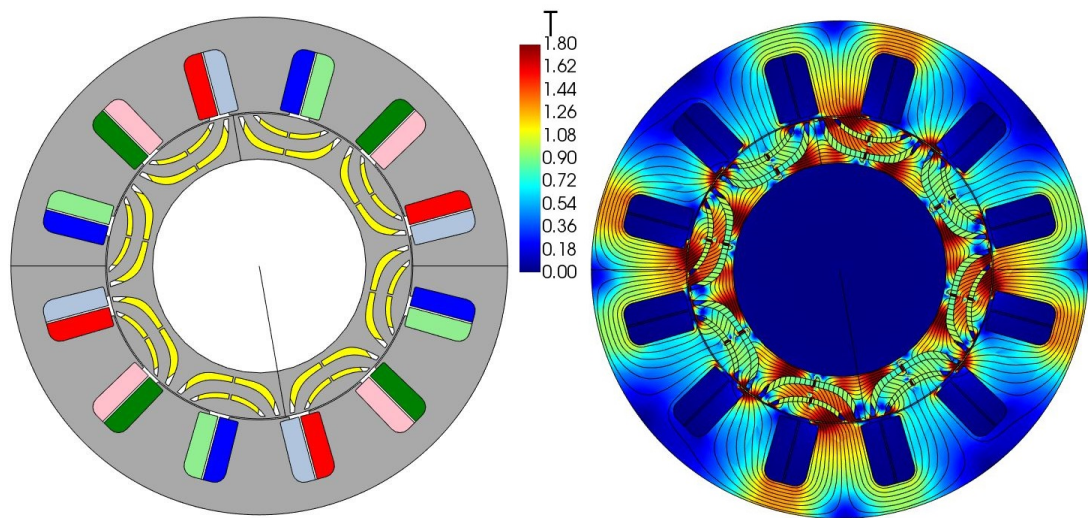


FIGURE 6.6: 8 poles PMaSynRM motor geometry, flux density and flux lines at rated working point

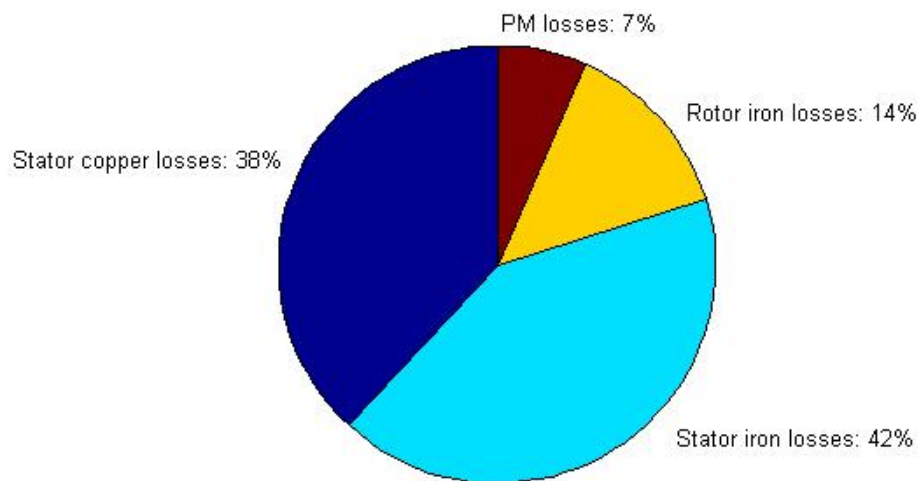


FIGURE 6.7: 8 poles PMaSynRM motor loss distribution at rated working point and magnet temperature 70 °C

TABLE 6.4: 8 poles PMaSynRM geometrical data and performance data at ambient temperature 25 °C

Insulation ratio	0.6
Number of barriers	2
Number of imaginary barriers	2
Inner rotor diameter [mm]	94.5
Outer diameter [mm]	220
Stator slot height [mm]	23
Stator slot width [mm]	18.5
Stator slot opening width [mm]	9
Effective conductors per slot	45
PM amount [Kg]	2.08
Rated efficiency [%]	95.45
Rated power factor	0.98
Peak-to-peak Torque Ripple [%]	26.18
Stator Temp. Rise [K]	26

decision was made to avoid the risk of demagnetization, while induced losses in the ferrite are negligible (low conductivity). The proposed geometry is shown in Fig.6.8 and the relevant geometric dimensions are summarized in Table 6.4.

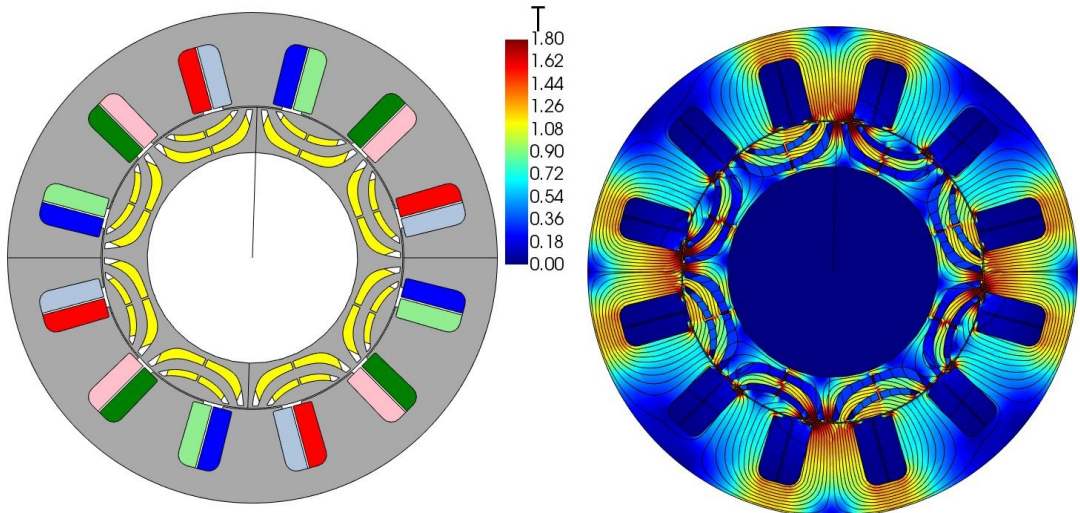


FIGURE 6.8: 8-pole PMaSynRM Ferrite motor geometry, flux density and flux lines at rated working point

6.4 Performance analysis and comparison method

All the presented motor alternatives have been simulated for several working conditions. More precisely, the operating conditions have been classified by ambient temperature (from -20°C to 195°C), load and speed.

TABLE 6.5: 8-pole PMaSynRM Ferrite geometrical and performance data at ambient temperature 25 °C

Insulation ratio	0.8
Number of barriers	2
Number of imaginary barriers	2
Inner rotor diameter [mm]	94.5
Outer diameter [mm]	220
Stator slot height [mm]	23
Stator slot width [mm]	18.5
Stator slot opening width [mm]	9
Effective conductors per slot	42
PM amount [Kg]	1.89
Rated efficiency [%]	92.97
Rated power factor	0.64
Peak-to-peak Torque Ripple [%]	54.45
Stator Temp. Rise [K]	52

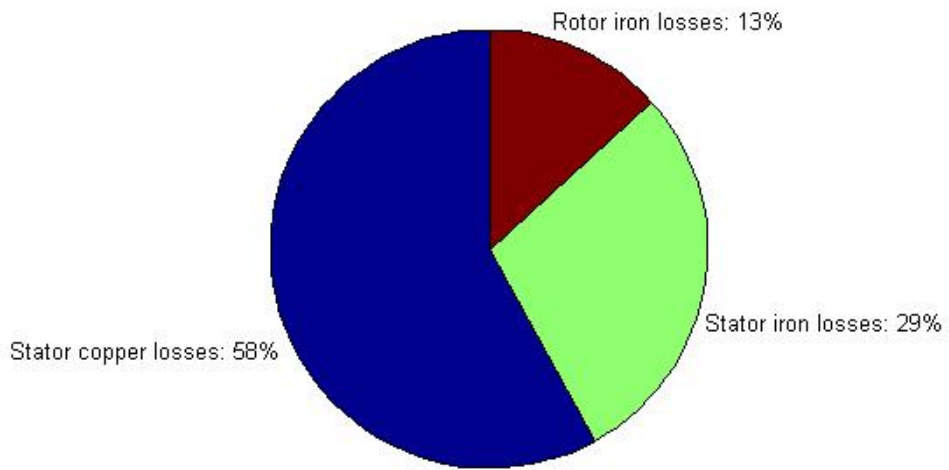


FIGURE 6.9: 8-pole PMaSynRM Ferrite motor loss distribution at rated working point and magnet temperature 70 °C

The simulated load/speed combinations are depicted in Fig.6.10.

In this way, it is not only possible to analyze the motor performance for different operating points other than the rated, but also understand the motor or PMs robustness with respect to the temperature. The demagnetization risk is a primary concern in order to ensure the motor reliability for several working conditions. The minimum permanent magnets flux density dependence with the temperature at different working points are retrieved and compared to the characteristics depicted in Fig.6.11 for the NdFeB and ferrite material employed in this work.

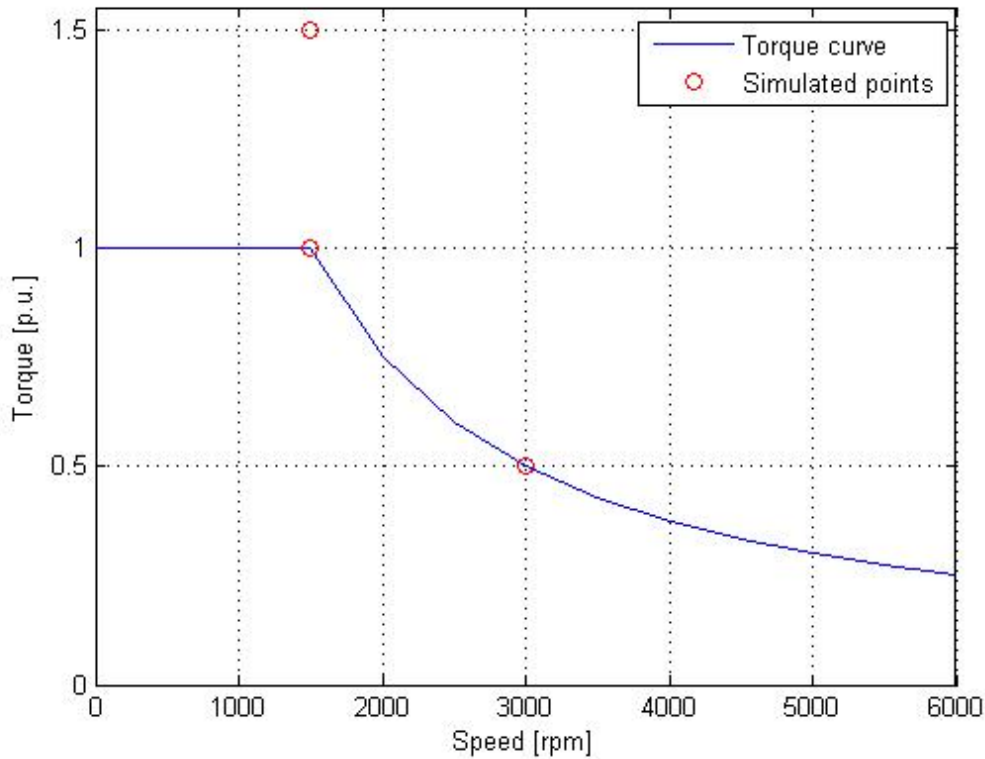


FIGURE 6.10: Simulated load/speed combinations and torque curve

As shown in Fig.6.11, NdFEB and ferrite knee points behave differently with respect to the temperature. This fact reflects the different temperature coefficients relative to the remanence flux density B_r and the coercitive field H_{ci} for the considered materials, as mentioned in Paragraph 2.2 .

The comparison is carried out in three different steps:

- topology-wise comparison
- comparison of different slot/pole combinations
- PM materials comparison i.e., NdFeB and ferrite

It is important to mention that the "nominal point" option, mentioned in section 1.4, in the simulation profile is also applied here. It means that Adept selects different current angles for different temperature levels. As a consequence, the following graphs (with the PM temperature as abscissa) give the best working condition possible for each temperature level, i.e. a qualitative insight on the temperature effects. Depending on the control's sensitivity to the temperature influence, the motor and drive may react differently in reality. The selection of the current angle should then be the object of

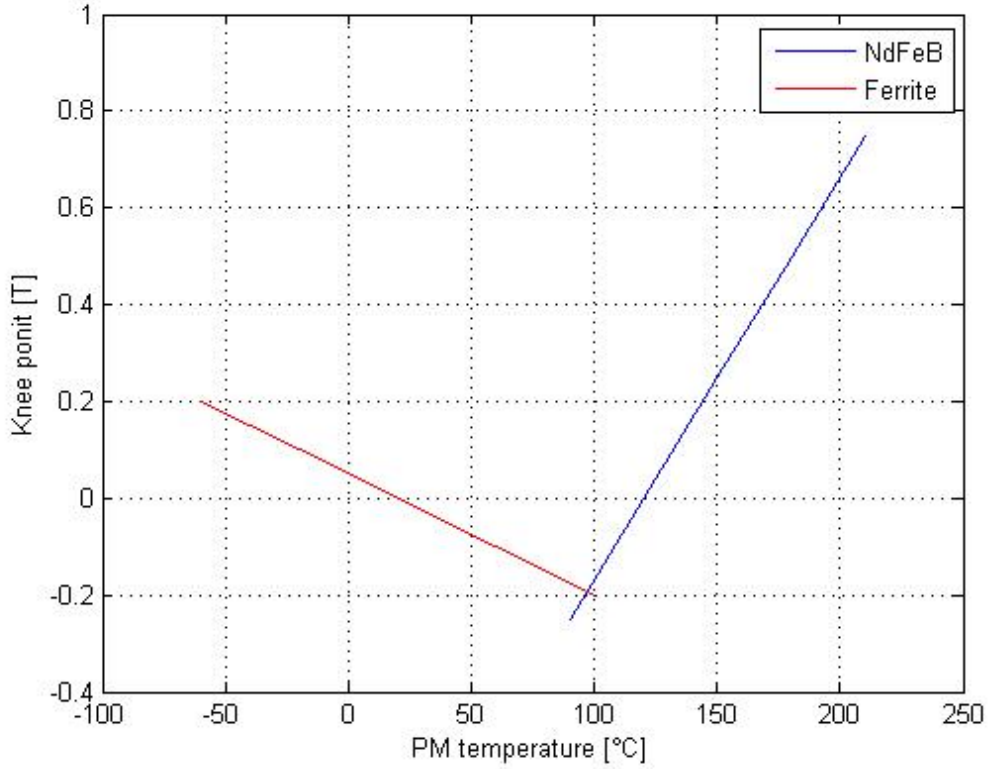


FIGURE 6.11: NdFeB 493a and NMF-7F Ferrite minimum permanent magnets flux density dependence with the temperature

investigation and can be optimized depending on the expected operation temperature range.

A example in which the motor gets demagnetized is given in Fig. 6.12, where PMaSynRM with 10-pole is simulated at rated point and at ambient temperature of 195 °C. The PM temperature results to be 209 °C and the minimum flux density which guarantees the PMs to not be demagnetized is 0.74 T.

6.5 Topology comparison

In this section, the 10-pole PMaSynRM is compared with the two alternative rotor topologies, namely V-shaped IPM and SMPM where, the poles/slots combination and the magnet materials are fixed. In this way, it is possible to give an insight on the performance, advantages, drawbacks and the relation to the temperature for each topology.

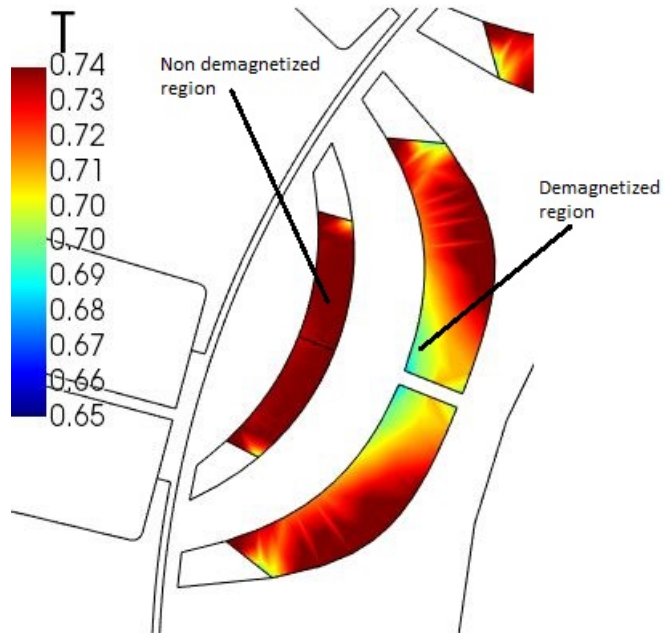


FIGURE 6.12: PMaSynRM 10-pole simulated at rated point and ambient temperature of 195 °C

6.5.1 Rated point

The efficiency, power factor and current dependency with the temperature are shown in Fig. 6.13, 6.14 and 6.15 for the rated point case.

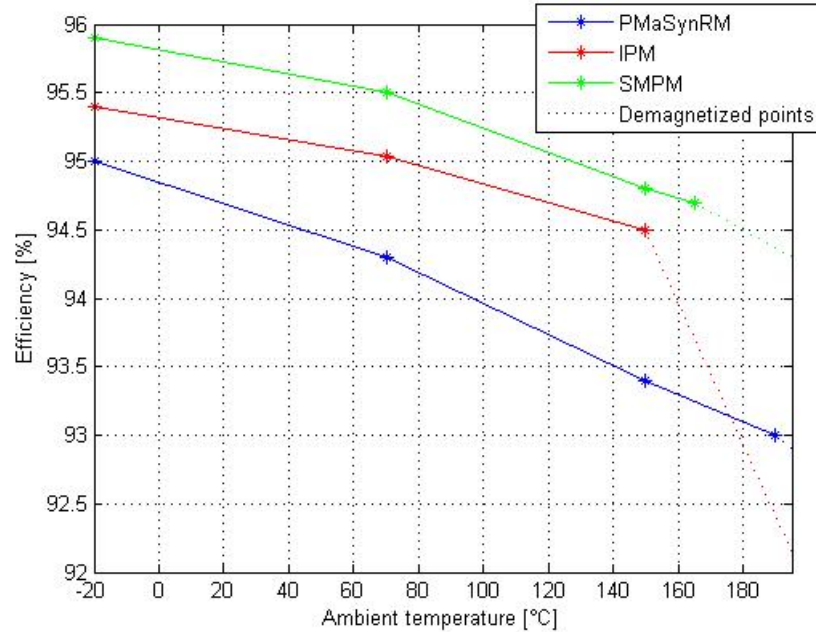


FIGURE 6.13: Efficiency comparison at rated point for different topologies

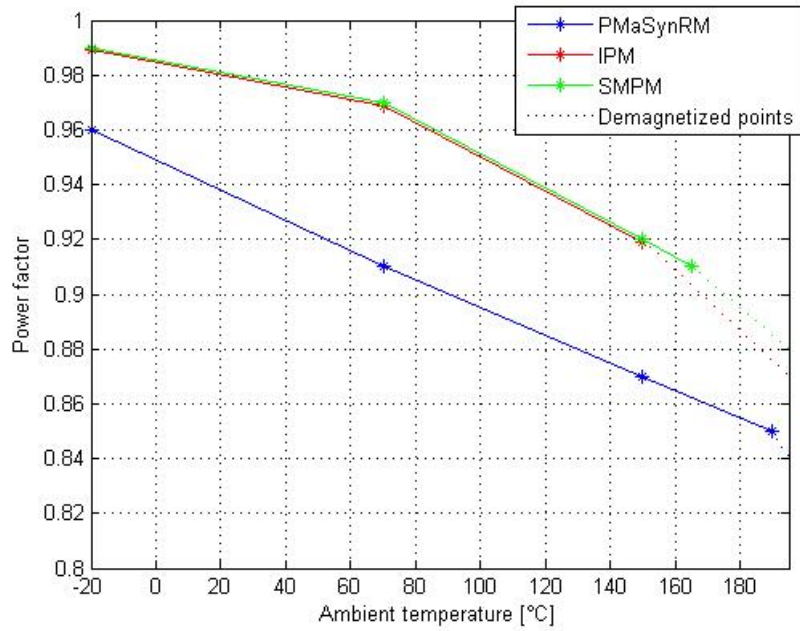


FIGURE 6.14: Power factor comparison at rated point for different topologies

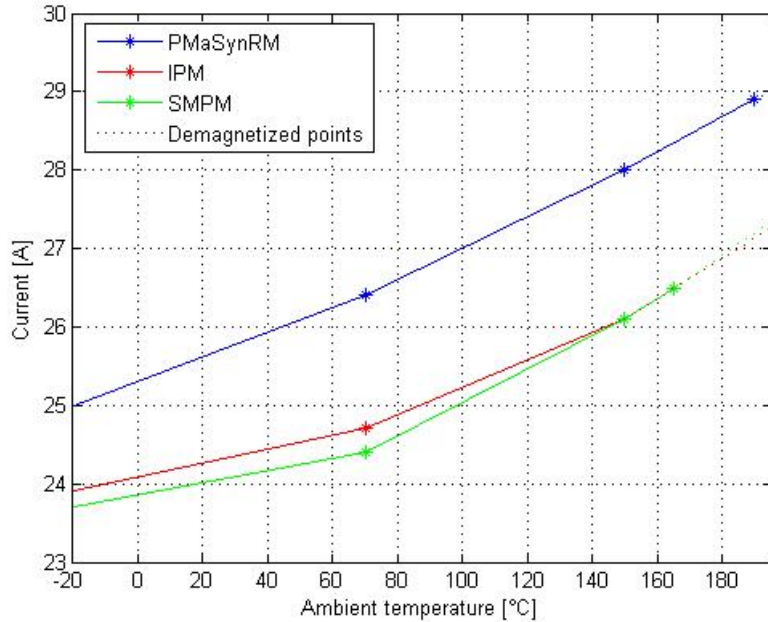


FIGURE 6.15: Current comparison at rated point for different topologies

Both efficiency and power factor decrease when the temperature increases for all the considered motor designs. This is due to the fact that the remanence flux density decreases for higher temperatures (it has a negative temperature coefficient) and hence the flux provided by the magnet is lower. As a consequence, in order to reach the desired torque, a higher current is needed. A higher current also means higher copper losses thus the efficiency is lowered. Concerning the power factor, it is obvious (from the vectorial

graph in Fig.2.14) that the lower the PM flux the lower the power factor. Moreover, the poorer performance of the 10-pole PMaSynRM is clearly seen in the graphs. Even with a higher amount of PM, efficiency and power factor are low for the whole temperature range, compared to IPM and SMPM. On the other hand, the maximum safe ambient temperature is higher for the PMaSynRM topology. It has been found to be 190 °C, while it is 150 °C and 165 °C for IPM and SMPM respectively. Anyhow, the IPM and SMPM maximum safe ambient temperature are still reasonable for most of the applications. The wider safe temperature range reachable by SMPM with respect to IPM, can be justified by the magnet thickness (3 mm vs 2 mm) even if the magnets are placed closer to the air-gap.

6.5.2 Overspeed

The efficiency, power factor and current variation with the temperature are depicted in Fig.6.16, 6.17 and 6.18 for an overspeed working point i.e., 3000 rpm.

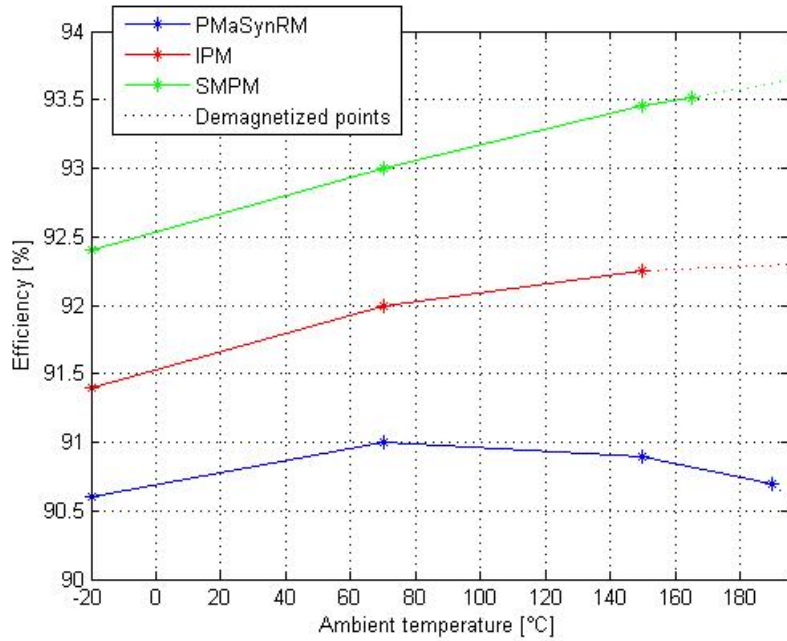


FIGURE 6.16: Efficiency comparison at 3000 rpm for different topologies

In this case, the trend is the opposite with respect to the rated point case. In the selected working point the motor is in flux-weakening operation, hence a demagnetizing current flows in the stator in order to keep the voltage within the maximum value. This demagnetizing current component produces copper losses without contributing to the torque. As a consequence, it lowers the efficiency. Moreover, it only creates a flux component (counteracting the PM flux), thus its presence lowers also the power factor. A higher PM temperature means a lower PM flux and a lower demagnetizing current is

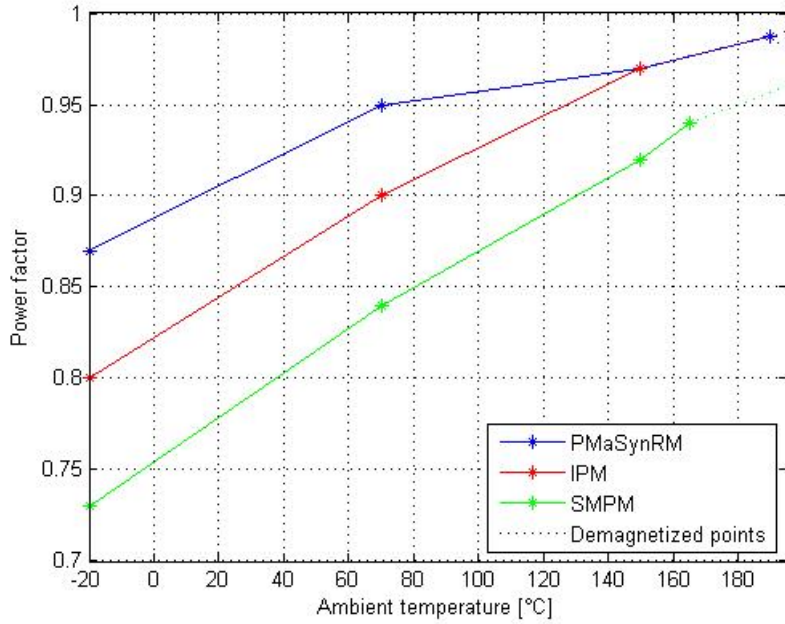


FIGURE 6.17: Power factor comparison at 3000 rpm for different topologies

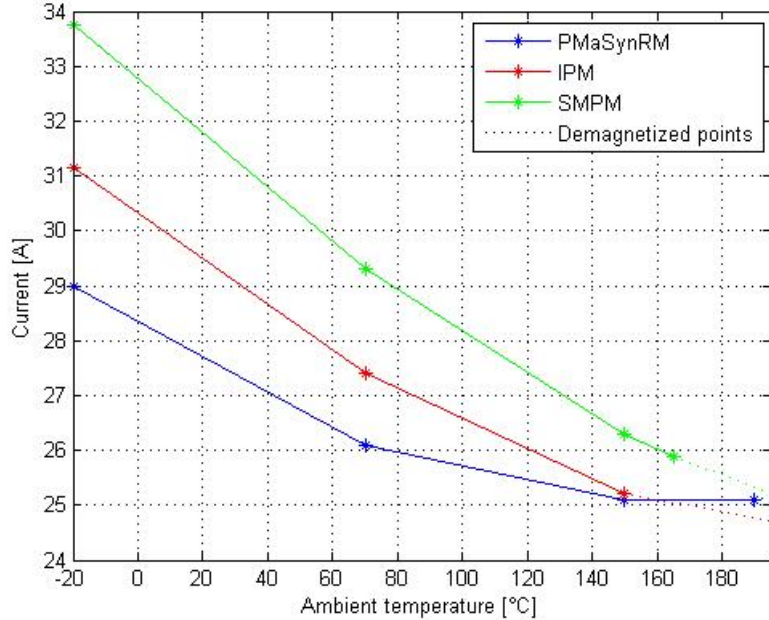


FIGURE 6.18: Current comparison at 3000 rpm for different topologies

needed in flux weakening condition. Thus, the higher the PM temperature the higher the efficiency and power factor, in flux-weakening condition. Fig. 6.16 show that, in this working condition, the PMaSynRM presents again the lower efficiency for all the considered temperatures.

Results show that in this operating condition a higher temperature corresponds to higher

performance, because a lower de-magnetizing current is needed in flux-weakening. This de-magnetizing current only produces copper losses without contributing to the torque production.

6.5.3 Overload

The efficiency, power factor and current variation with the temperature are depicted in Fig. 6.19, 6.20 and 6.21 for an overload working point i.e., 1.5 pu and rated speed.

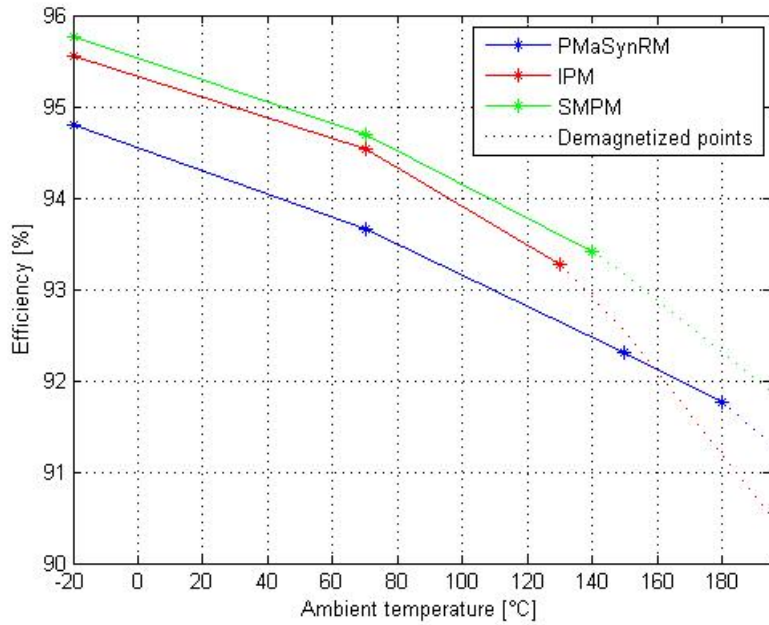


FIGURE 6.19: Efficiency comparison at 1.5 pu load for different topologies

The efficiency and power factor trends are similar to what was found at rated condition and the reasoning provided for that case applies also here. The poor performance obtained by the PMaSynRM motor are underlined also in this case. The safe temperature range is in this case restricted compared to the rated case. This is due to the higher current required and the consequently higher MMF produced by the stator winding.

6.6 Slot/pole combinations comparison

The next comparison step consists on fixing the rotor topology (PMaSynRM) and the magnet material (NdFeB) and compare two different poles/slots combinations i.e., 10 poles/12 slots and 8 poles/12 slots.

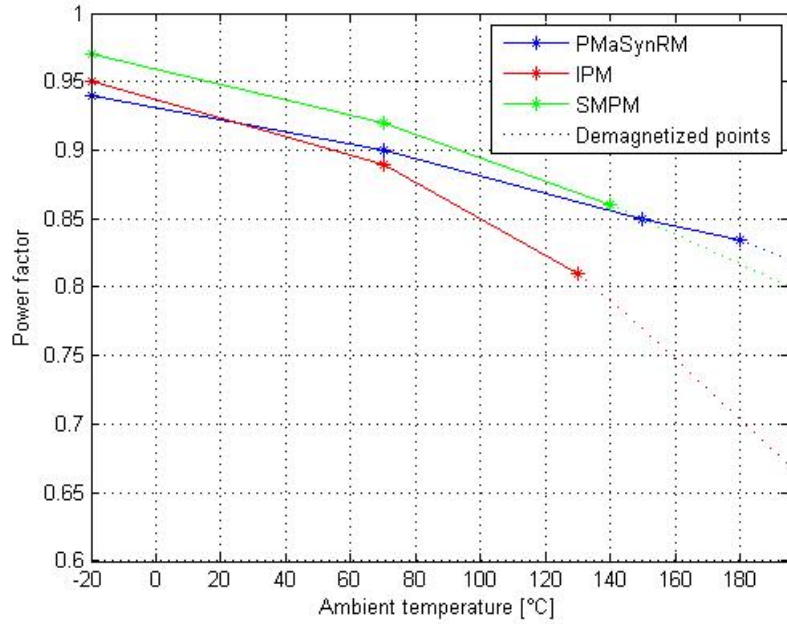


FIGURE 6.20: Power factor comparison at 1.5 pu load for different topologies

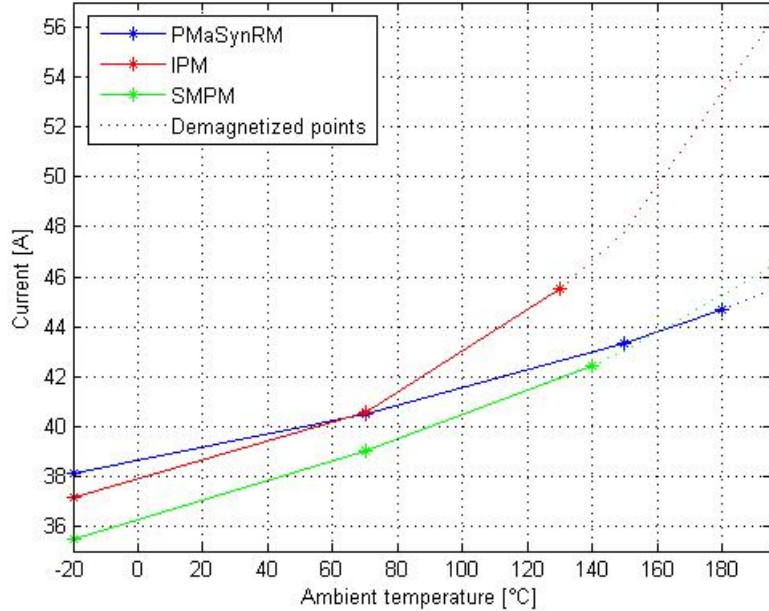


FIGURE 6.21: Current comparison at 1.5 pu load for different topologies

6.6.1 Rated point

The efficiency, power factor and current dependency with the temperature are shown in Fig.6.22, 6.23 and 6.24 for the rated point case.

A clear result from the slot/pole combination comparison at rated point is that the

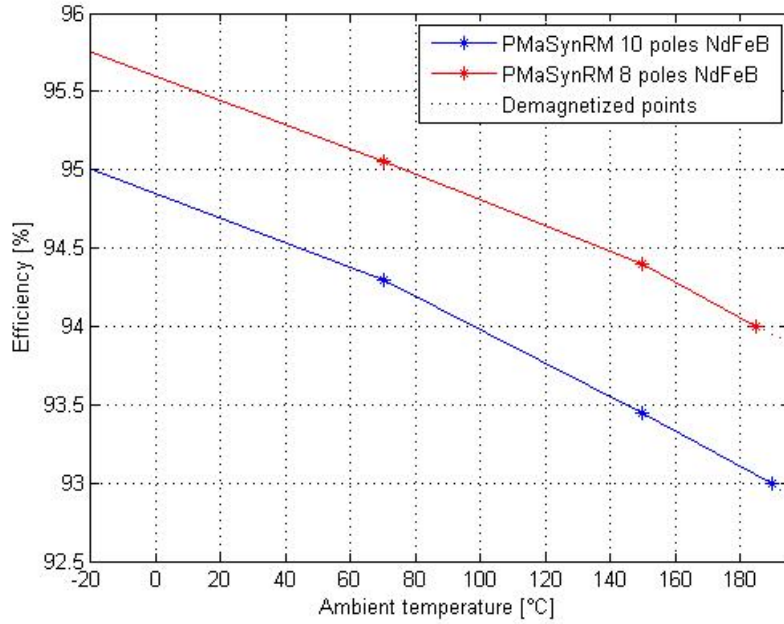


FIGURE 6.22: Efficiency comparison at rated point for different poles/slots combinations

8-pole motor has better performance, in terms of efficiency and power factor, for all the considered temperatures. It is important to notice that the 8-pole PMaSynRM design presents a reduction on PM amount of 24% compared to the 10-pole solution.

6.6.2 Overspeed

The efficiency, power factor and current variation with the temperature are depicted in Fig. 6.25, 6.26 and 6.27 for an overspeed working point i.e., 3000 rpm.

In over-speed condition the efficiency gap between the two designs is even more evident, while the power factor does not show a large difference for all the considered ambient temperatures. The larger efficiency gap can be justified by the PM parasitic losses effect i.e., eddy currents which increase with the frequency. Hence, a larger rare earth PM amount (which presents a relatively high conductivity) represents an important loss source, especially at higher frequencies.

6.6.3 Overload

The efficiency, power factor and current variation with the temperature are depicted in Fig. 6.28, 6.29 and 6.30 for an overload working point i.e., 1.5 pu and rated speed.

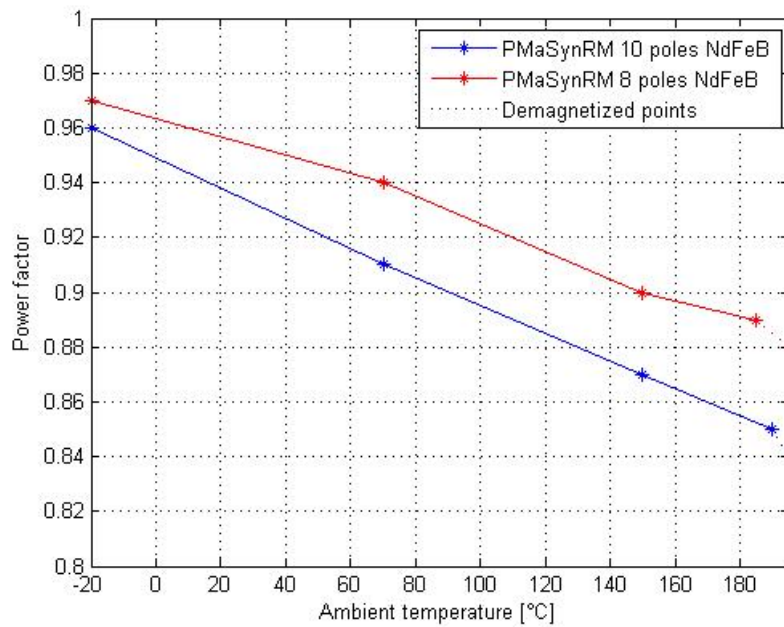


FIGURE 6.23: Power factor comparison at rated point for different poles/slots combinations

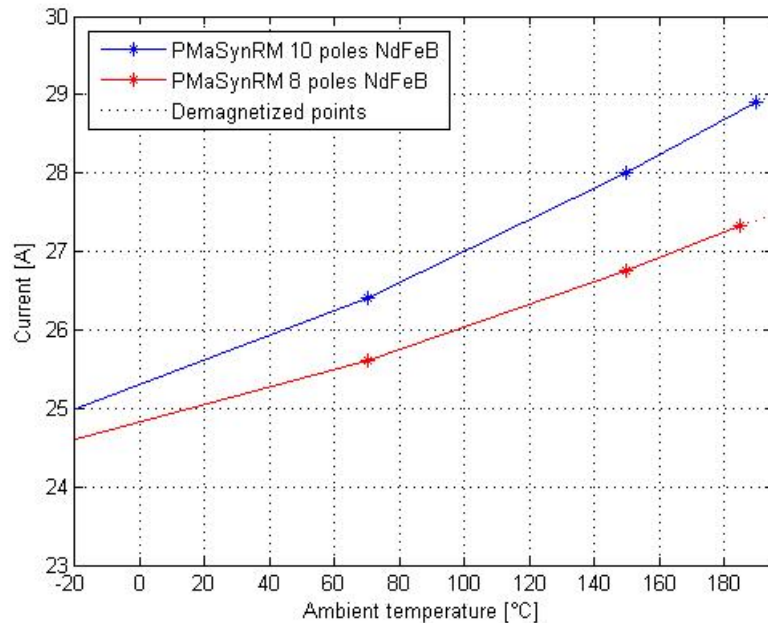


FIGURE 6.24: Current comparison at rated point for different poles/slots combinations

The graphs show a similar temperature dependence with the rated operation point. The 8-pole design is characterized by better performances for all the considered temperatures also in this case.

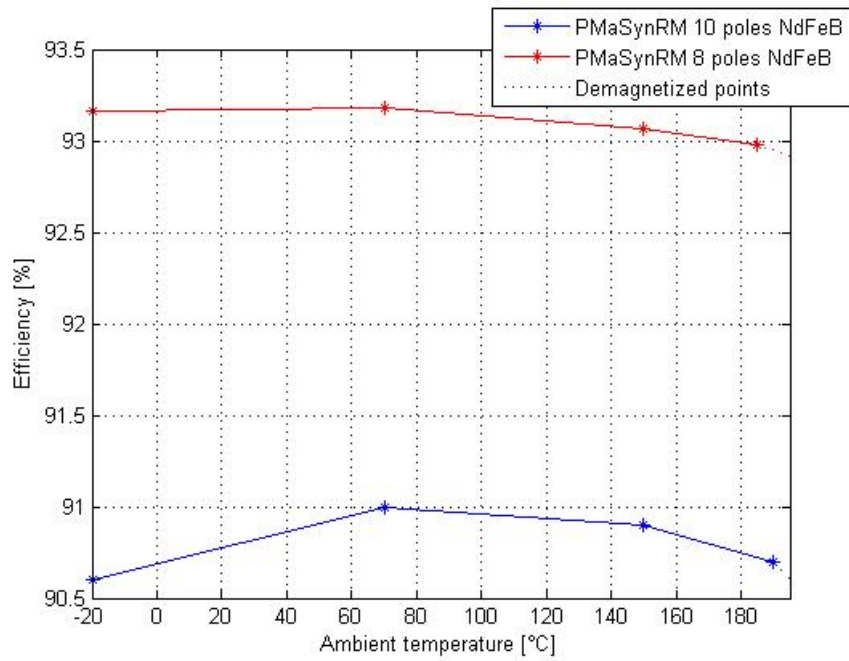


FIGURE 6.25: Efficiency comparison at 3000 rpm for different poles/slots combinations

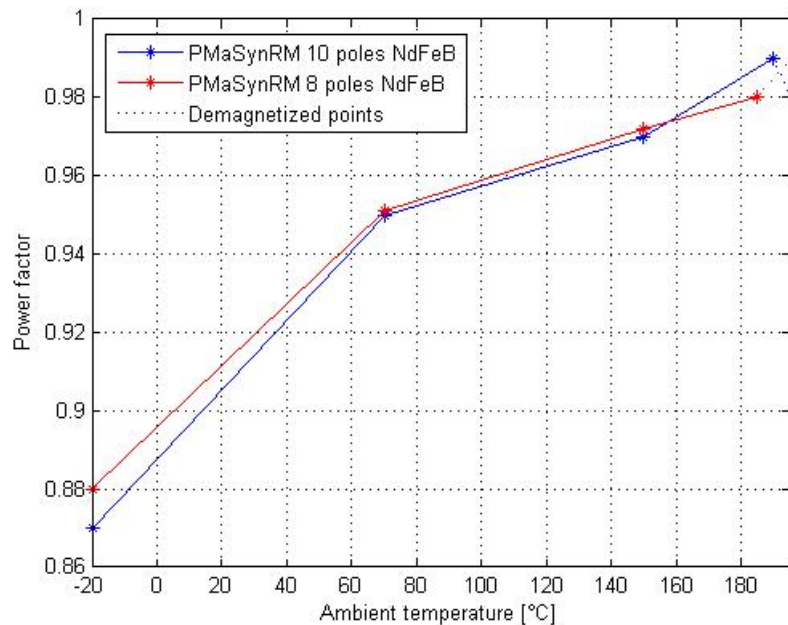


FIGURE 6.26: Power factor comparison at 3000 rpm for different poles/slots combinations

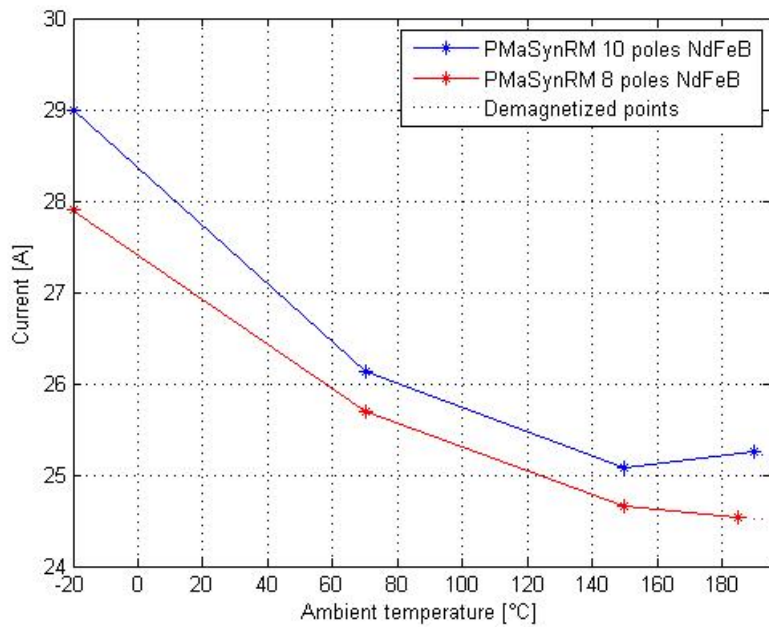


FIGURE 6.27: Current comparison at 3000 rpm for different poles/slots combinations

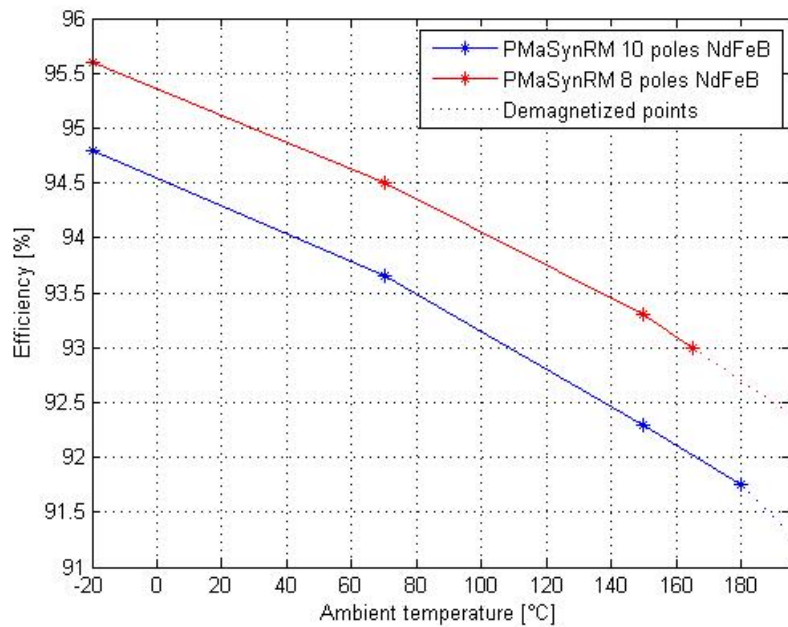


FIGURE 6.28: Efficiency comparison at 1.5 pu load for different poles/slots combinations

6.7 PM materials comparison

The final step of this comparative analysis is meant to underline the different effects the magnet material provide on the motor performance and temperature effects on it.

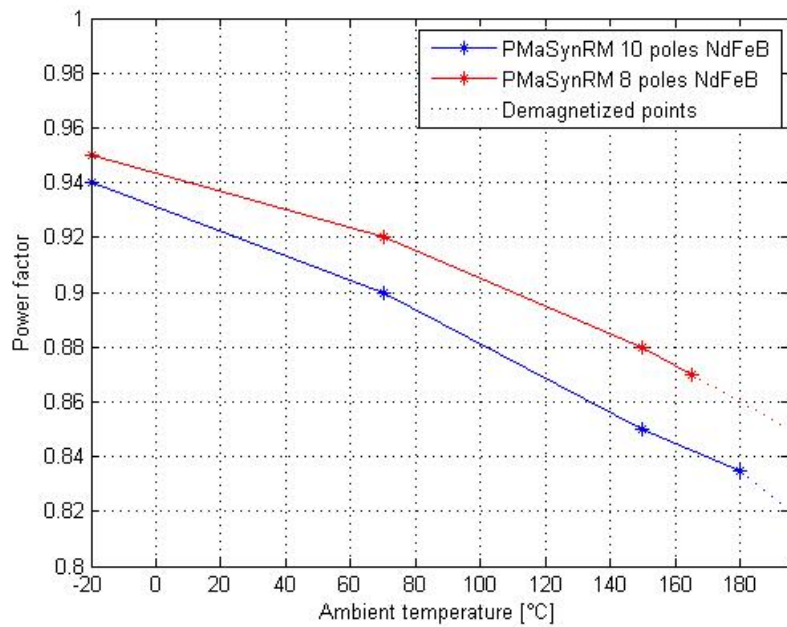


FIGURE 6.29: Power factor comparison at 1.5 pu load for different poles/slots combinations

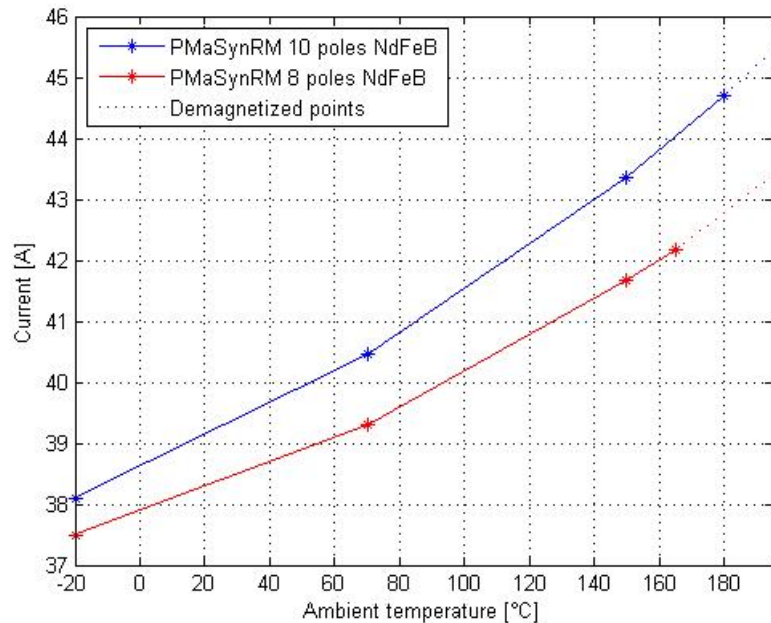


FIGURE 6.30: Current comparison at 1.5 pu load for different poles/slots combinations

For this reason, the rotor topology is fixed (PMaSynRM) as well as the poles/slots combination (8/12), while two PM materials are employed: NeFeB and Ferrite.

6.7.1 Rated point

The efficiency, power factor and current dependency with the temperature are shown in Fig. 6.31, 6.32 and 6.33 for the rated point case.

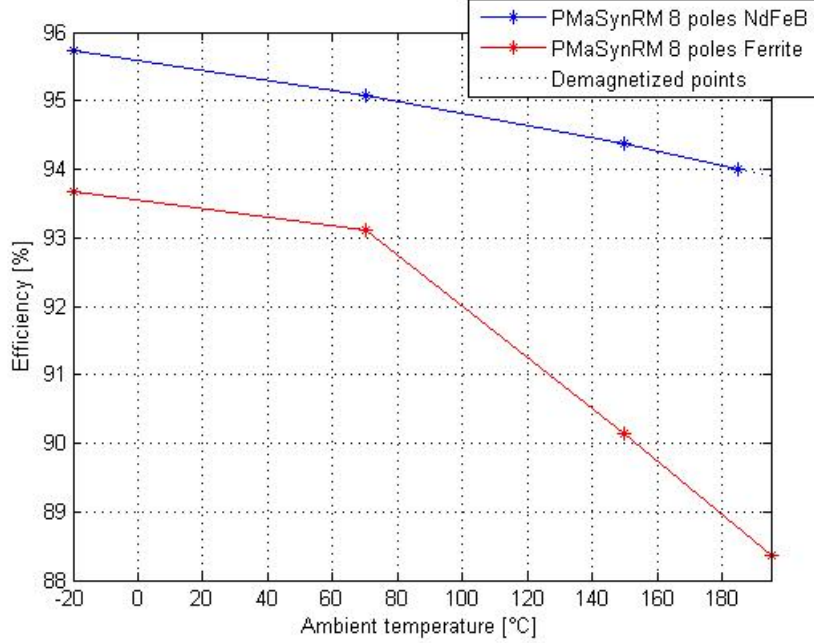


FIGURE 6.31: Efficiency comparison at rated point for different PM materials

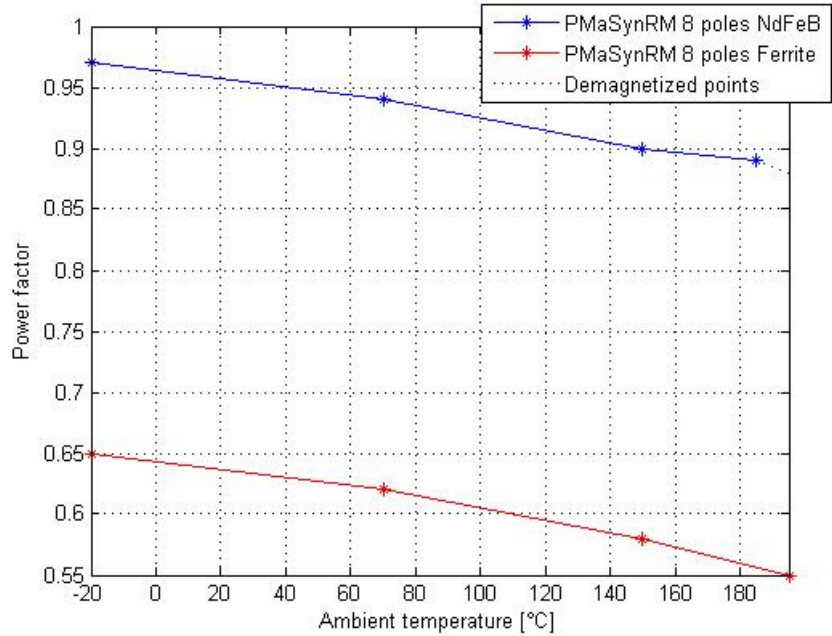


FIGURE 6.32: Power factor comparison at rated point for different PM materials

The two compared motors present a significant difference in terms of efficiency and power factor. This results leads to the conclusion that, even in the 8-pole PMaSynRM

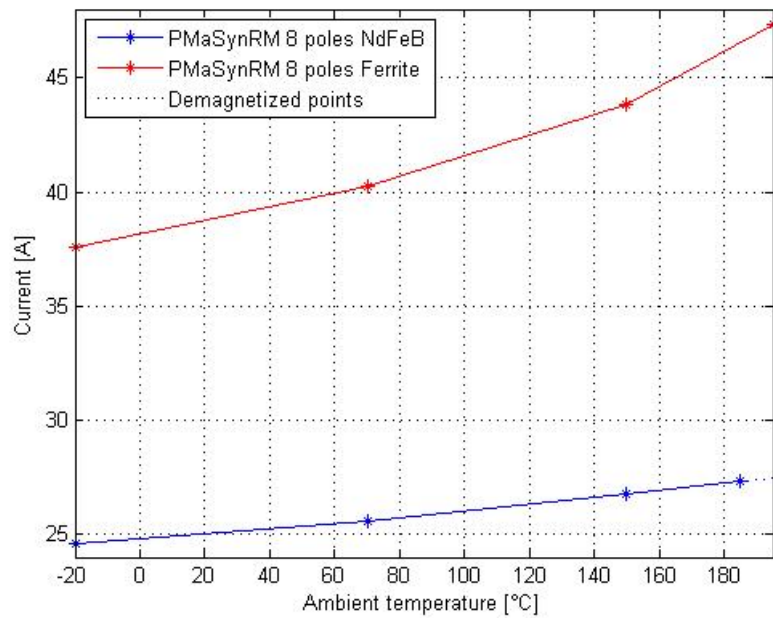


FIGURE 6.33: Current comparison at rated point for PM materials

motor with NdFeB the PM torque contribution is relevant and it is appropriate to overcompensate the motor.

The ferrite assisted motor was not able to reach 3000 rpm by maintaining the rated power of 15 kW and the 50% overload at rated speed.

6.8 Influence of the load angle

The motors with different rotor positions and maintaining the same voltage phase were simulated. The current phase depends on the rotor position (because of the anisotropy). The simulation results show the maximum torque capability for each motor at 1500 rpm and at a ambient temperature of 25 °C as shown in Fig.6.34. The nominal working points at 95.5 Nm (15 kW) are marked with red dots.

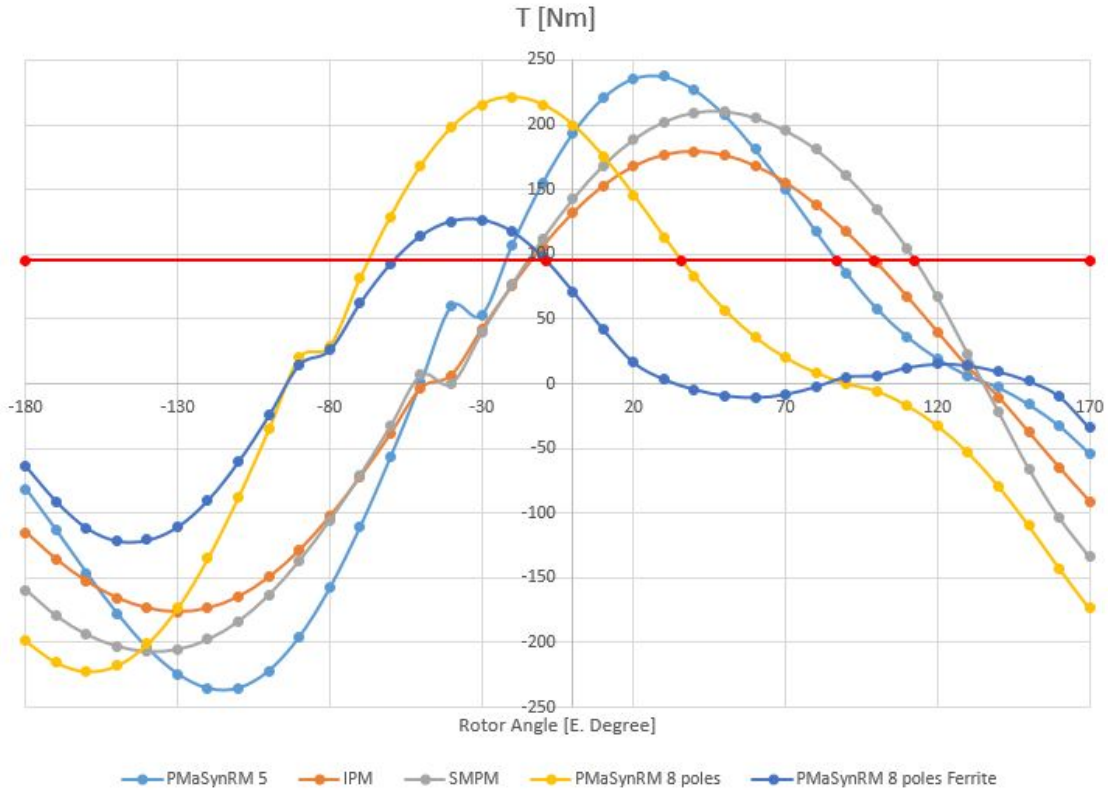


FIGURE 6.34: Overload capability analysis for the studied motor designs at ambient temperature 25 °C

These curves present how the motor would behave if synchronized on a network, as a synchronous motor. The interesting information is the ratio of the maximum value of the torque at given voltage in relation to the nominal torque R_T , summarized in Table 6.6 for all the considered motors. It shows the overload capability of the motor.

The 10-pole and 8-pole PMaSynRM with NdFeB designs present the highest R_T values. The main factor influencing this result is the presence of a large amount of rare-earth PM. The IPM and SMPM designs present relatively high value of R_T , while the 8-pole PMaSynRM with ferrite value is considerably lower.

TABLE 6.6: Torque ratio R_T for the considered motors

	R_T [-]	T_{MAX} [Nm]
IPM 10-pole NdFeB	1.88	179.4
SMPM 10-pole NdFeB	2.2	210.4
PMaSynRM 10-pole NdFeB	2.49	237.4
PMaSynRM 8-pole NdFeB	2.32	221.3
PMaSynRM 8-pole Ferrite	1.32	126.45

6.9 General comparison

A general comparison of the considered motors is given in this section. An overview of all the studied motor designs is shown in Fig.6.35 where the different design choices are presented. Moreover, a performance and cost-wise comparison is given in Table 6.7, where two standard motors (rated 15 kW) are taken as reference: an induction motor and a SynRM. In order to estimate the material cost, the material prices have been chosen as

- Iron: 2.1 [USD/Kg] [33]
- Copper: 7.1 [USD/Kg] [33]
- Aluminium: 2.5 [USD/Kg] [35]
- NdFeB: 83 [USD/Kg] [33]
- Ferrite: 6 [USD/Kg] [34]

It is important to say that rare earth permanent magnet price experiences fluctuations because of the international market situation. Thus, the following considerations could lead to slightly different conclusion if made in a different point of time.

All the designed motors with rare earth magnets present high efficiencies and power factors. The PMaSynRM designs, 10-pole and 8-pole, present an relatively high amount of PM which reflects on higher material cost, in comparison to the IPM and SMPM solution. This suggests that the PMaSynRM topology is not beneficial for this high

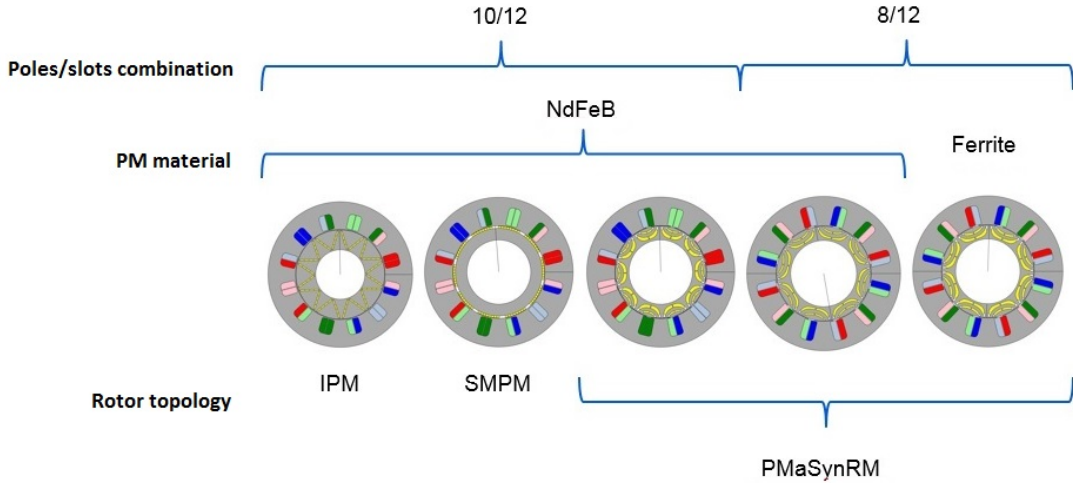


FIGURE 6.35: General overview of all the studied motor designs

TABLE 6.7: General motor designs comparison

	Efficiency [%]	Power factor [-]	T_{MAX} [Nm]	Material Cost [USD]
SynRM DW 4-pole (reference motor)	93.03	0.76	223	125.32
IM 4-pole (reference motor)	91.25	0.83	339.35	165.6
IPM 10-pole NdFeB	95.24	0.99	179.42	250.6
SMPM 10-pole NdFeB	95.7	0.99	210.45	228.1
PMaSynRM 10-pole NdFeB	94.65	0.94	237.41	338.7
PMaSynRM 8-pole NdFeB	95.45	0.98	221.32	289.7
PMaSynRM 8-pole Ferrite	92.97	0.64	126.45	128.7

number of poles and the rated power level. Moreover, the 8-pole PMaSynRM with ferrite presents similar efficiency and material cost as for the 4 poles SynRM, but with a lower power factor. This result gives an insight on the anisotropy deficiency in a 8-pole SynRM structure. The anisotropy increases moving from 10 to 8 poles, as expected. In fact the 8 poles design presents slightly better performance even if the PM quantity employed is lower (2.08 Kg versus 2.74 Kg) as well as the winding factor (0.866 versus 0.933). These results are valid for the concentrated winding design. Indeed, different anisotropy levels can be reached with distributed windings, as investigated in [32].

TABLE 6.8: Permanent magnets effectiveness and resistance to demagnetization at rated point

	PM amount [Kg]	Induced Voltage @1500 rpm [V]	Induced Voltage @1500 rpm per PM amount [V/Kg]	Ambient temp. demagn. limit [°C]
IPM 10-pole NdFeB	1.6	392.4	245.25	< 150
SMPM 10-pole NdFeB	1.37	392.6	286.57	< 165
PMaSynRM 10-pole NdFeB	2.74	312.4	114.01	< 190
PMaSynRM 8-pole NdFeB	2.08	311.1	149.57	< 185
PMaSynRM 8-pole Ferrite	1.89	74.5	39.42	—

It is also interesting to study the magnet effectiveness, in terms of flux production, in the different analysed solutions. The PM and flux barriers shape and position in the rotor structure influence the magnetic circuit reluctance, hence the flux amount does not depend only on the PM amount. If the speed is fixed, it is possible to compare the flux production indirectly by means of the induced voltage in the stator windings. From Table 6.8, it is evident that the PMaSynRM topology has the lowest induced voltage with respect to the PM amount. This is because the iron shape of the rotor is intended to block the q-axis flux, both in positive and negative direction. For this reason, it could be convenient to pursue with an other topology. As extensively explained in chapter 2, the difference between PMaSynRM and IPM motors is not in their working principle, but it is basically in the different design approach. When the PMaSynRM motor is largely overcompensated the main flux of the motor is provided by the PMs as it happens in the IPM motor. The PMs are not used only to compensate the undesired L_q inductance. This fact is evident in Fig. 6.36, where the flux lines are mainly aligned with the q-axis.

It is well known from the basic theory that the inductance could be expressed as

$$L = \frac{N^2}{R} \quad (6.1)$$

where N is the number of turns and R is the reluctance seen by the flux. It is now possible to insert 6.1 in 2.10 and obtain

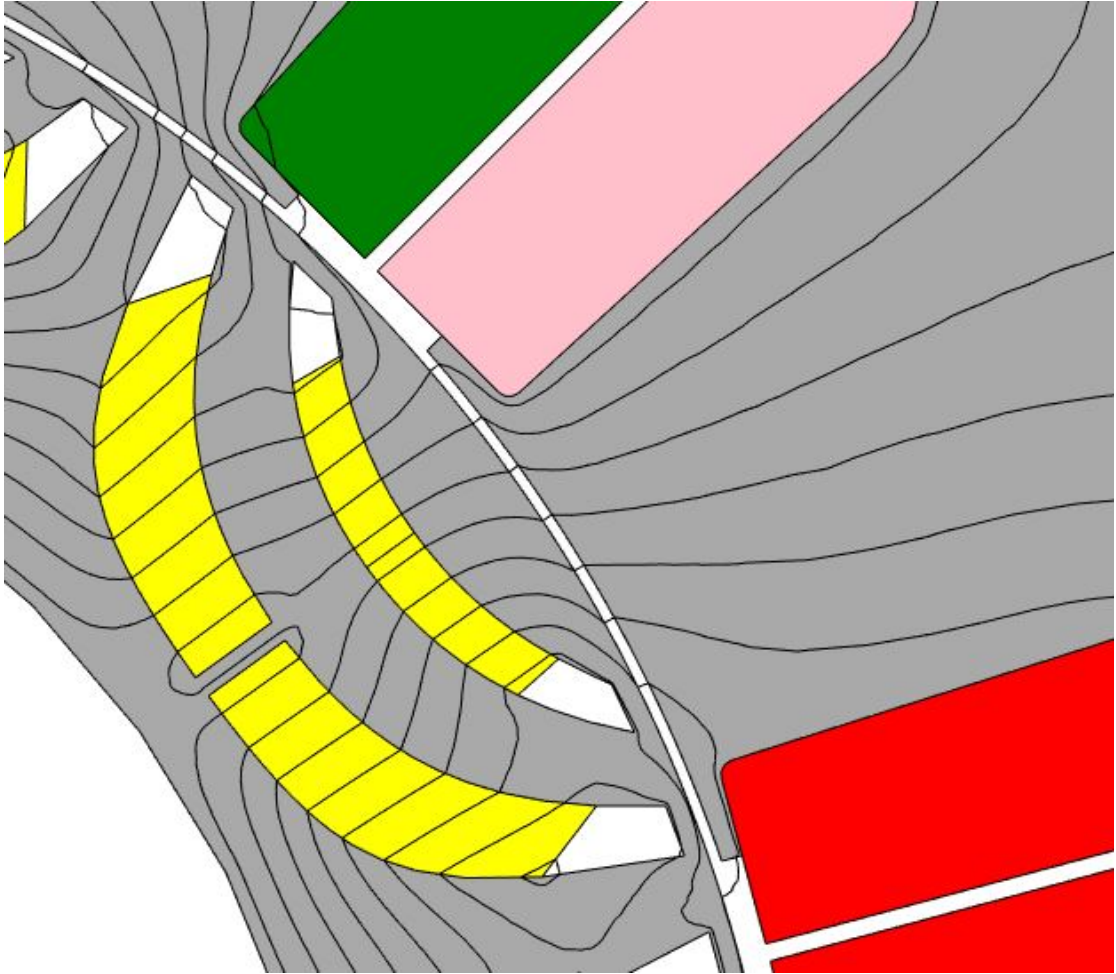


FIGURE 6.36: Main flux orientation in the designed PMaSynRM

$$T = \frac{3}{2}p((L_d - L_q)i_{dm}i_{qm} - \frac{F_{PM}}{N^2}L_qi_{dm}) \quad (6.2)$$

From equation 6.2, it is possible to deduce that for high F_{PM} values, the L_q minimization typical in PMaSynRM motors is not convenient from a material cost point of view (as shown in Table 6.7) as well as for torque production. In other words, it could be more profitable to maximize the permanent magnet torque instead of the reluctance component which typically happens in IPM motors.

The proposed PMaSynRM designs present a higher robustness with respect to the demagnetization, at the expense of a higher PM quantity. However, the temperature range characterizing the IPM and SMPM designs covers almost all the electric drives application requirements.

Chapter 7

Conclusions and Future Work

Finally, the report concludes with a summary of the results obtained in this work and some possible future work is suggested.

7.1 Conclusions

After a literature study, several design steps based on analytical and FEM analysis has been carried on. Moreover, an analytical PMs minimization strategy, based on the motor magnetic model proposed in [28] has been proposed. Lastly, four alternative motors with different topologies, number of poles and PM material have been designed, optimized and analyzed in order to make a wide comparison for the specified target application.

The main conclusion of this work is that the achievable saliency is lowered if the number of poles is increased and the SynRM reluctance structure does not exploit the PMs contribution in a proper way. Therefore, the PMaSynRM topology (with 8 or 10 poles) does not produce both the PM and the reluctance torque in an efficient way. As a consequence, 'low number of poles' motors match well with the PMaSynRM topology while 'high number of poles' motors combine well with IPM and SMPM topologies.

7.2 Future Work

As a possible future work development, it would be interesting to expand the comparison made in this thesis. 4-pole and 6-pole PMaSynRM motor designs could be included in order to better evaluate how the number of poles affects the reluctance. As Carvajal Almendros C. states in [37], it is possible to build 4-pole PMaSynRM motors (both with concentrated and distributed winding) providing good performance, in terms of efficiency

and power factor, without overcompensating the motor (with this configuration it is possible to reach the highest saliency levels). Because of the lower compensation level, it is then possible to either fill the flux barriers with ferrite or place a small amount of NdFeB, obtaining similar efficiency and power factor values. In the first case, the material cost of the motor is very low (even comparable to SynRM and IM) while in the second case it was possible to study the most convenient PM location inside the rotor (it is found that only the torque ripple is appreciably improvable).

In this thesis only motor designs with concentrated windings are treated. It would be interesting to include DW motors in the study in order to see how the results and conclusion would diverge from what is found in this document.

In this report, the possibility to overcompensate the SynRM motor has been taken into consideration. It would be interesting to verify the convenience of this design strategy also for lower number of poles (i.e. 4-pole and 6-pole motors).

In order to have a better understanding on the PMs utilization of the topologies treated, it would be enlightening to formulate and provide a more detailed comparison between IPM and PMaSynRM with lumped magnetic models.

Lastly, in order to validate the accuracy of the simulations, it would be useful to include harmonic losses due to the inverters, make use of 3D FEM analysis in order to test the accuracy of the end-winding effects estimation (taken into account by analytically) and build and test prototypes.

Bibliography

- [1] Florence Meier, *Permanent-Magnet Synchronous Machines with Non-Overlapping Concentrated Windings for Low-Speed Direct-Drive Application*. Doctoral Thesis in Electrical Engineering, KTH Stockholm, 2008.
- [2] Reza - Rajabi Moghaddam, *Synchronous Reluctance Machine (SynRM) in Variable Speed Drives (VSD) Applications*. Doctoral Thesis in Electrical Engineering, KTH Stockholm, 2011.
- [3] Freddy Magnussen, *On Design and Analysis of Synchronous Permanent Magnet Machines for Field-Widening Operation in Hybrid Electric Vehicles*. Doctoral Thesis in Electrical Engineering, KTH Stockholm, 2004.
- [4] N. Bianchi, M.D. Pré, *Use of the Star of Slots in Designing Fractional-slot Single-layer Synchronous Motors*. IEE Proceedings-Electric Power Applications, Volume 153, Issue 3, Pages 459-466, May 2006.
- [5] N. Bianchi, S. Bolognani, E. Fornasiero, *A general approach to determine the rotor losses in three-phase fractional-slot PM machines*. Electric Machines and Drives Conference, 2007. IEMDC '07. IEEE International, Volume 1, May 2007.
- [6] N. Bianchi, S. Bolognani, A. Consoli, T. M. Jahns, R. D. Lorenz, E. C. Lovelace, S. Morimoto, A. Vagati, *Design, Analysis and Control of Interior PM Synchronous Machines*. IEEE Ind. Appl. Society, Annual Meeting, Seattle, USA, October 3rd, 2004.
- [7] T. M. Jahns, V. Caliskan, *Uncontrolled Generator Operation of Interior PM Synchronous Machines Following High-Speed Inverter Shutdown*. IEEE Transactions and Industry Applications, Volume 35, Issue 6, Nov.-Dec. 1999.
- [8] C. Sadarangani, *Electrical Machines: Design and Analysis of induction and permanent magnet motors*. KTH Royal Institute of Technology, 2006.
- [9] Rare-earth Permanent Magnet Vacuumshmelze Brochure,
http://www.vacuumschmelze.com/fileadmin/Medienbibliothek_2010/Downloads/DM/VACODYM-VACOMAX_PD002_2014_en.pdf .

- [10] E. Armando, P. Guglielmi, G. Pellegrino, M. Pastorelli, A. Vagati *Accurate Modelling and Performance Analysis of IPM-PMASR Motors*. IEEE Transactions and Industry Applications, Volume 45, NO.1, January/February 2009.
- [11] A. M. El-Refaie, *Fractional-Slot Concentrated-Windings Synchronous Permanent Magnet Machines: opportunities and Challenges*. Industrial Electronics, IEEE Transactions, Volume 57, Issue 1, January 2010.
- [12] S. Ooi, S. Morimoto, M. Sanada, Y. Inoue, *Performance evaluation of a high-power-density PMaSynRM with ferrite magnets*. Industry Applications, IEEE Transactions, Volume 49, Issue 3, May-June 2013.
- [13] Yung-kang Chin, *A Permanent Magnet Synchronous Motor for an Electric Vehicle - Design Analysis*. Licentiate Thesis, Stockholm, 2004.
- [14] G. Pellegrino, E. Armando, P. Guglielmi, *Direct Flux Field-Oriented Control of IPM Drives With Variable DC Link in the Field-Weakening Region*. Industry Applications, IEEE Transactions, Volume 45, Issue 5, September-October 2009.
- [15] W.L. Soong, T.J.E. Miller, *Field-weakening performance of brushless synchronous AC motor drives*. IEEE Proceeding of Electric Power Application, 141(6), pp. 331-340, 1994.
- [16] G. Bertotti, *General properties of power losses in soft ferromagnetic materials*. IEEE Transactions on Magnetics, Vol.24, pp. 621-630, 1988.
- [17] G. Bertotti, A. Boglietti, M. Chiampi, D. Chiarabaglio, F. Fiorillo, M. Lazzari, *An improved estimation of iron losses in rotation electrical machines*. IEEE Transactions on Magnetics, 27(6), pp. 5007-5009, 1991.
- [18] F. Deng, *An improved iron loss estimation for permanent magnet brushless machines*. IEEE Transactions on Energy Conversion, 14(4), pp. 1391-1395, 1997.
- [19] A. Krings, J. Soulard, *Overview and comparison of iron loss models for electrical machines*. Journal of Electrical Engineering, vol.10, no.3, pp. 162-169, September 2010.
- [20] W. L. Soong, *Sizing of Electrical Machines*. Power Engineering Briefing Note Series, 26 September 2008.
- [21] T. J. E. Miller, *Brushless Permanent-Magnet and Reluctance Motor Drives*. Oxford Science Publications, 1989.
- [22] T. A. Lipo, *Introduction to AC Machines Design*. Wisconsin Power Electronics research Center, University of Wisconsin, 2004.

- [23] Reza - Rajabi Moghaddam, *Synchronous Reluctance Machine (SynRM) Design.* Master Thesis in Electrical Engineering, KTH Stockholm, 2007.
- [24] N. Bianchi, S. Bolognani, D. Bon, M.D. Pré, *Rotor flux-barrier design for torque ripple reduction in synchronous reluctance motors.* Industry Application Conf., 41st IAS Annual Meeting, Conf. Record of the IEEE, Volume 3, 8-12 Oct. 2006 Page(s): 1193-1200.
- [25] A. Vagati, G. Franceschini, I. Marongiu, G.P. Troglia, *Design criteria of high performance synchronous reluctance motors.* Industry Application Society Annual Meeting, Conf. Record of the IEEE, 4-9 Oct. 1992 Page(s): 66-73, vol.1.
- [26] L. Alberti, M. Barcaro, N. Bianchi, *Design of a Low-Torque-Ripple Fractional-Slot Interior Permanent-Magnet Motor.* IEEE Transactions on Industry Application, Volume 50, No. 3, May/June 2014.
- [27] A. Vagati, M. Pastorelli, G. Franceschini, S.C. Petrache, *Design of a low-torque-ripple synchronous reluctance motor.* IEEE Transactions on Industry Application, Volume 34, Issue 4, July/August 1998, pp:758-765.
- [28] P. Guglielmi, B. Boazzo, E. Armando, G. Pellegrino, A. Vagati, *Permanent-Magnet Minimization in PM-Assisted Synchronous Reluctance Motors for Wide Speed Range.* IEEE Transactions on Industry Application, Volume 49, No. 1, January/February 2013.
- [29] G. Dajaku, D. Gerling, *Reduction of Low Space Harmonics for the Fractional Slot Concentrated Windings Using a Novel Stator Design.* IEEE Transactions on Magnetics, Volume 50, No. 5, May 2014.
- [30] Rare-earth Permanent Magnet Neorem Brochure,
<http://www.neorem.fi/permanent-magnets.html> .
- [31] Ferrite Permanent Magnet Hitachi Brochure,
<http://www.hitachimetals.com/product/permanentmagnets/ferrite> .
- [32] M. Gamba, G. Pellegrino, A. Vagati, *A new PM-Assisted Synchronous Reluctance Machine with a Nonconventional Fractional Slot per Pole Combination.* 2014 International Conference on Optimization of Electrical and Electronic Equipment, pp.268-275, May 2014
- [33] C. Du-Bar, *Design of a fault-tolerant fractional slot PMSM for a vehicle application.* Licentiate Thesis in Electrical Engineering, Chalmers University of Technology, 2014.

- [34] A. Isfanuti, M. Baba, L. Tutelea, A. Moldovan, I. Boldea, *Surface NdFeB versus Ferrite IPM motor drive for low power (100 W to 2000 W) applications: FEM embedded optimal design with full step torque response validation in sensorless vector control*. Industrial Electronics Society, IECON 2013 - 39th Annual Conference of the IEEE, November 2013.
- [35] ABB LV Motors Västerås (SE) expertise, oral communication with Dan Fors, December 2014.
- [36] J. Soulard, F. Meier, *dq Theory Applied to a Permanent Magnet Synchronous Machine with Concentrated Windings*. 4th IET International Conference on Power Electronics, Machines and Drives (PEMD 2008), pp.194-198, 2008.
- [37] C. Carvajal Almendros, *Design and Analysis of a Fractional Slot Concentrated Winding PM assisted Synchronous Reluctance Machine (FSCW-PMaSynRM)*. Master Thesis in Electrical Engineering, KTH Stockholm, 2015.

TRITA XR-EE-E2C 2015:003